

# The IRX- $\beta$ relation of high-redshift galaxies

Lichen Liang<sup>1\*</sup>, Robert Feldmann<sup>1</sup>, Christopher C. Hayward<sup>2</sup>, Desika Narayanan<sup>3,4,5</sup>,  
Onur Çatmabacak<sup>1</sup>, Dušan Kereš<sup>6</sup>, Claude-André Faucher-Giguère<sup>7</sup>, Philip F. Hopkins<sup>8</sup>

<sup>1</sup>*Institute for Computational Science, University of Zurich, Winterthurerstrasse 190, Zurich CH-8057, Switzerland*

<sup>2</sup>*Center for Computational Astrophysics, Flatiron Institute, 162 Fifth Avenue, New York, NY 10010, USA*

<sup>3</sup>*Department of Astronomy, University of Florida, 211 Bryant Space Sciences Center, Gainesville, FL 32611 USA*

<sup>4</sup>*University of Florida Informatics Institute, 432 Newell Drive, CISE Bldg E251, Gainesville, FL 32611*

<sup>5</sup>*Cosmic Dawn Center at the Niels Bohr Institute, University of Copenhagen and DTU-Space, Technical University of Denmark*

<sup>6</sup>*Department of Physics, Center for Astrophysics and Space Sciences, University of California at San Diego, La Jolla, CA 92093, USA*

<sup>7</sup>*Department of Physics and Astronomy and CIERA, Northwestern University, Evanston, IL 60208, USA*

<sup>8</sup>*TAPIR, Mailcode 350-17, California Institute of Technology, Pasadena, CA 91125, USA*

Accepted 2020. Received 2020; in original form 2020

## ABSTRACT

The relation between infrared excess (IRX) and UV spectral slope ( $\beta_{UV}$ ) is an empirical probe of dust properties of galaxies. The shape, scatter, and redshift evolution of this relation are not well understood, however, leading to uncertainties in estimating the dust content and star formation rates (SFRs) of galaxies at high redshift. In this study, we explore the nature and properties of the IRX- $\beta_{UV}$  relation with a sample of  $z = 2 - 6$  galaxies ( $M_* \approx 10^9 - 10^{12} M_\odot$ ) extracted from high-resolution cosmological simulations (MassiveFIRE) of the Feedback in Realistic Environments (FIRE) project. The galaxies in our sample show an IRX- $\beta_{UV}$  relation that is in good agreement with the observed relation in nearby galaxies. IRX is tightly coupled to the UV optical depth, and is mainly determined by the dust-to-star geometry instead of total dust mass, while  $\beta_{UV}$  is set both by stellar properties, UV optical depth, and the dust extinction law. Overall, much of the scatter in the IRX- $\beta_{UV}$  relation of our sample is found to be driven by variations of the intrinsic UV spectral slope. We further assess how the IRX- $\beta_{UV}$  relation depends on viewing direction, dust-to-metal ratio, birth-cloud structures, and the dust extinction law and we present a simple model that encapsulates most of the found dependencies. Consequently, we argue that the reported ‘deficit’ of the infrared/sub-millimetre bright objects at  $z \gtrsim 5$  does not necessarily imply a non-standard dust extinction law at those epochs.

**Key words:** dust: extinction — galaxies: evolution — galaxies: high-redshift — galaxies: ISM — infrared: galaxies

## 1 INTRODUCTION

Reliable estimates of the SFR of galaxies at low and high- $z$  is crucial for constraining the various physical processes associated with galaxy evolution at different epochs (e.g. Madau & Dickinson 2014). The rest-frame UV luminosities of galaxy ( $L_{UV}$ ), which are dominated by the light of the young, massive stars, are commonly used as diagnostics of the current SFR of galaxy (e.g. Kennicutt 1998; Kennicutt & Evans 2012; Conroy 2013; Flores Velázquez et al. 2020). However, the accuracy of this method can be hampered by the effect of dust attenuation (e.g. Salim & Narayanan 2020). It is known that a large fraction of stellar radiation in the Universe is absorbed by interstellar dust and becomes re-emitted at infrared (IR) and millimetre (mm) wavelengths in the form of thermal radiation (e.g. Calzetti et al. 2000; Magnelli et al. 2009; Reddy et al.

2010; Burgarella et al. 2013; Gruppioni et al. 2013; Whitaker et al. 2017). Therefore, it is critical to account for both the dust thermal emission as well as the UV light of stars to accurately measure the SFR of galaxies.

However, estimating the dust luminosity of distant galaxies can be very challenging. While the UV photometry of many high- $z$  galaxies can be extracted from the deep broadband imaging surveys (e.g., Bouwens et al. 2009; Ellis et al. 2013; McLure et al. 2013; Bouwens et al. 2014; McLeod et al. 2015; Oesch et al. 2015; Laporte et al. 2016; Oesch et al. 2018), reliable measurement of their dust continuum is often not possible. Many single-dish IR telescopes, such as *Herschel* and SCUBA, have high confusion noise due to their poor spatial resolution (e.g. Dole et al. 2004; Nguyen et al. 2010; Berta et al. 2011; Lutz 2014), and therefore source detection is limited to the most IR-luminous objects at high redshifts (e.g., Casey et al. 2014a). Interferometric telescopes (e.g. ALMA) have significantly improved the detection limit with higher resolu-

\* Email: lliang@physik.uzh.ch

tion and sensitivity, but these can only probe relatively small volumes. Therefore, on many occasions, one needs to infer the bolometric IR luminosity (and the obscured SFR) of high- $z$  galaxies through alternative, indirect methods.

One common alternative strategy is by using the empirical relationship between the UV spectral slope ( $\beta_{UV}$ ), defined as the index in the power-law relationship  $f_\lambda \propto \lambda^{\beta_{UV}}$  over the wavelength range  $1200 < \lambda < 3200 \text{ \AA}$ <sup>1</sup> (e.g., Calzetti et al. 1994; Leitherer & Heckman 1995; Calzetti 1997), and their infrared excess ( $IRX \equiv L_{IR}/L_{UV}$ ) of galaxies. While  $\beta_{UV}$  is a measure of the reddening of UV colour (assuming that the variation in the intrinsic UV spectral slope is negligible), IRX is a proxy for dust attenuation. A higher dust attenuation should increase both IRX and the amount of reddening, and  $\beta_{UV}$  and IRX may be correlated. Observationally, it was at first revealed by the seminal work of Meurer et al. (1995, 1999, hereafter M99) that their selected nearby starburst sample (originally compiled by Calzetti et al. 1994) exhibited a fairly tight sequence in the IRX- $\beta_{UV}$  plane. Their result suggested that  $L_{IR}$  could potentially be reliably constrained when only UV measurements ( $L_{UV}$  and  $\beta_{UV}$ ) were available.

From then on, efforts have been made to extend the study of this empirical relationship using a wider range of diverse galaxy populations. Despite the promising nature of this technique, growing observational evidence has shown that galaxies of a broad range of types can exhibit a non-trivial degree of variations in the IRX- $\beta_{UV}$  relation and show much larger scatter than the original result of M99. For instance, some studies have discovered that the local ultra-luminous infrared galaxies (ULIRGs) tend to have bluer  $\beta_{UV}$  in comparison to the canonical M99 relation at their IRX (e.g., Goldader et al. 2002; Buat et al. 2005; Howell et al. 2010; Casey et al. 2014b). On the other hand, observations of nearby normal star-forming and quiescent galaxies have shown that these galaxies appear to be systematically ‘redder’ than the M99 relation and occupy a fairly wide range of positions on the diagram (e.g. Bell 2002; Buat et al. 2002; Kong et al. 2004; Buat et al. 2005; Boquien et al. 2012; Grasha et al. 2013). These findings from the local observations suggest that the general galaxy populations may not follow a tight, universal IRX- $\beta_{UV}$  relation.

In recent years, a growing number of studies have focused on the IRX- $\beta_{UV}$  relation at higher- $z$  in order to probe the evolution of the dust attenuation properties of galaxies (e.g., Reddy et al. 2010; Heinis et al. 2013; Bouwens et al. 2016; Álvarez-Márquez et al. 2016; Reddy et al. 2018; Koprowski et al. 2018). Many of these studies are based on large samples of UV/optical-selected Lyman-break galaxies (LBGs) due to the efficiency of the source selection techniques (Steidel et al. 1996). The IR dust emission of individual high- $z$  LBGs, however, is often undetected (e.g., Adelberger & Steidel 2000; Reddy et al. 2006), and their IRXs are derived instead with a stacking method. Here, galaxies are binned by their measured  $\beta_{UV}$  and for each bin, IRX is derived from the stacked UV and IR photometry of the binned galaxies.

The results reported by these studies are not entirely conclusive. While some found results to be in good agreement with the original M99 relation derived using local starbursts (e.g., Heinis et al. 2013; Bourne et al. 2017; Fudamoto et al. 2017; McLure et al. 2018; Koprowski et al. 2018; Álvarez-Márquez et al. 2019; Fudamoto et al. 2020), others reported a redder and much shallower relation (e.g., Álvarez-Márquez et al. 2016; Bouwens et al. 2016; Reddy et al. 2018). As a consequence, different conclusions have

been reached regarding the evolution of dust attenuation properties with redshift.

What is missing from the analysis of the stacked high- $z$  LBGs, however, is that the results do not truly reflect the level of scatter among the individual systems, but instead, represents only the luminosity-averaged properties of the galaxies at a given  $\beta_{UV}$  and can be easily dominated by several high-luminosity outliers. Probing this scatter observationally is challenging, as typically only a small subset of the sample are detected in the dust continuum, even with the unprecedented sensitivity of ALMA (e.g. Bouwens et al. 2016; Dunlop et al. 2017; Fudamoto et al. 2020). For the rest of the samples, only upper limits on their IRX are known. The few observations able to study the scatter in individual objects suggest that it is significant ( $\sigma_{IRX} \gtrsim 0.3$  dex; Oteo et al. 2013; Fudamoto et al. 2020). However, our knowledge of this scatter in the general galaxy population at high- $z$  is still fairly limited.

Apart from the approach of using UV-selected LBGs, a few recent studies have analysed samples of high- $z$  dusty star-forming galaxies (DSFGs), which are generally the galaxy population selected at IR/submm bands (e.g., Penner et al. 2012; Casey et al. 2014b). IR-selected samples typically have complete UV detections, enabling a measurement of the IRX- $\beta_{UV}$  relation of individual galaxies. These studies showed that DSFGs have systematically bluer  $\beta_{UV}$  compared to the local M99 relation as well as the LBG samples at their given IRX (Penner et al. 2012; Casey et al. 2014a,b; Safarzadeh et al. 2017b). Furthermore, deviation of the DSFGs from the M99 relation appears to show a clear correlation with  $L_{IR}$  (Casey et al. 2014a,b; Narayanan et al. 2018a). These findings suggest that the derived IRX- $\beta_{UV}$  relation of high- $z$  samples may be susceptible to selection effects.

The high sensitivity and resolution of ALMA has allowed the detection of dust emission of very early galaxies (i.e.,  $z \gtrsim 5$ ) which was previously not possible with single-dish telescopes (e.g., Capak et al. 2015; Watson et al. 2015; Walter et al. 2016; Bouwens et al. 2016; Laporte et al. 2017; Venemans et al. 2017; Carniani et al. 2018a; Jin et al. 2019; Novak et al. 2019; Matthee et al. 2019; Bañados et al. 2019; Neeleman et al. 2020; Bakx et al. 2020; Faisst et al. 2020; Bouwens et al. 2020, and Novak et al. submitted). To date, there have been a handful of objects at this epoch that have reported observational constraints on their IRX- $\beta_{UV}$  relation but with large scatter. One major challenge is that the galaxies at such high redshifts are often observed at fewer photometric bands (both UV and IR) compared to those at low- or intermediate redshifts (Casey 2012; Casey et al. 2018b; Popping et al. 2017; Reddy et al. 2018; Liang et al. 2019), and therefore observational constraints on  $\beta_{UV}$  and  $L_{IR}$  of these galaxies have much larger uncertainties. For example,  $L_{IR}$  extrapolated from a single-band ALMA flux density depends strongly on the adopted ‘dust temperature’<sup>2</sup> associated with the assumed functional form of the SED (Capak et al. 2015; Bouwens et al. 2016; Faisst et al. 2017; Casey et al. 2018b; Liang et al. 2019). Using 45 K instead of 35 K with a standard modified blackbody (MBB) function (Hildebrand 1983) will lead to a factor of  $\sim 3$  increase in the derived IRX. It is therefore of paramount importance to constrain the uncertainties in the measurements of

<sup>1</sup> Throughout this paper, ‘ $\lambda$ ’ stands for rest-frame wavelength.

<sup>2</sup> The ‘dust temperature’ here does not mean a physical temperature. Observations and simulations have shown that ISM dust has a wide distribution of (physical) temperature (e.g. Harvey et al. 2013; Lombardi et al. 2014; Behrens et al. 2018; Liang et al. 2019). Observationally, often a simplified SED function is adopted for extrapolating  $L_{IR}$  from single-band submm flux density, and the ‘ $T$ ’ parameter in the function is referred to as the ‘dust temperature’ of galaxy in the literature (Casey 2012; Casey et al. 2014a).

$\beta_{UV}$  and  $L_{IR}$  and to compare them to the intrinsic scatter of the IRX- $\beta_{UV}$  relation at high redshift.

Over the years, there have been a range of theoretical works that explore the physical nature of the IRX- $\beta_{UV}$  relation and the scatter in this relation, including those that adopt analytic and semi-analytic approaches (e.g., Granato et al. 2000; Noll et al. 2009; Ferrara et al. 2017; Faisst et al. 2017; Popping et al. 2017; Reddy et al. 2018; Qiu et al. 2019; Salim & Boquien 2019) as well as the ones utilising idealised/cosmological hydrodynamic galaxy formation simulations (e.g., Jonsson et al. 2006; Safarzadeh et al. 2017b; Narayanan et al. 2018a; Behrens et al. 2018; Ma et al. 2019; Schulz et al. 2020; Shen et al. 2020). With different modelling methodologies, these attempts have been successful in accounting for the general power-law trend in the IRX- $\beta_{UV}$  relation as well as reproducing the observed ‘secondary dependence’ of this relation on other variables (e.g.  $L_{IR}$  and sSFR).

The current general consensus amongst the different studies is that while dust optical depth is the key for driving a galaxy’s location along the IRX- $\beta_{UV}$  relation, the displacement off the relation arises from variations in the intrinsic UV spectral slope and the shape of the dust attenuation curve (see e.g. Salim & Narayanan 2020, and the references therein). Several mechanisms have been suggested that influence the shape of the attenuation curve of galaxies, including changes of the intrinsic dust properties (e.g. dust composition and dust grain sizes; Pei 1992; Fitzpatrick 1999; Weingartner & Draine 2001; Gordon et al. 2003; Safarzadeh et al. 2017b; Narayanan et al. 2018a), the spatial configuration of the dust and UV-emitting stars (e.g. Natta & Panagia 1984; Calzetti et al. 1994; Witt & Gordon 1996; Gordon et al. 1997; Charlot & Fall 2000; Witt & Gordon 2000; Narayanan et al. 2018b; Trayford et al. 2019), and the level of ISM turbulence (Fischera et al. 2003; Seon & Draine 2016; Popping et al. 2017). However, the importance of these mechanisms has not been conclusively determined, leaving open the significance of such variations in comparison with those resulting from changes of the intrinsic UV spectral slope.

High resolution cosmological ‘zoom-in’ galaxy formation simulations are ideal tools to quantify the relative importance of the various sources to the scatter in the IRX- $\beta_{UV}$  relation and to understand how they are related to the observed ‘secondary dependence’ of the relation. These simulations can model the various physical processes, including cosmic gas accretion, gas cooling, metal/dust production, and feedback processes, that are essential for reproducing the realistic star formation histories of galaxies as well as the complex geometry of dust distribution within galaxies (Somerville & Davé 2015; Vogelsberger et al. 2020). Synthetic spectral energy distribution (SED) and multi-frequency imaging of the simulated sample can be produced through dust radiative transfer (RT) modelling (e.g. Hayward & Smith 2015; Snyder et al. 2015; Torrey et al. 2015; Camps et al. 2018; Narayanan et al. 2020). Subsequently, various observational properties of galaxies can be derived and a direct comparison to observations becomes possible.

In this work, we study the IRX- $\beta_{UV}$  relation using a galaxy sample at  $z = 2 - 6$  that is extracted from the MASSIVEFIRE simulation suite (Feldmann et al. 2016, 2017). We focus on exploring the origin of the relation, and quantify the relative importance of the several main contributors to the intrinsic scatter. We also analyse how they contribute to the observed ‘secondary dependence’ of the relation on other galaxy properties and how the relation depends on the evolutionary stage of a galaxy. Moreover, we also compare the level of the intrinsic scatter driven by the different mechanisms with the observational uncertainties of  $\beta_{UV}$  and  $L_{IR}$  measurements of high- $z$  galaxies.

This paper is structured as follows. In Section 2, we summarise the simulation methodology and details of the radiative transfer analysis of our sample. In Section 3, we compare the predicted IRX- $\beta_{UV}$  relation of our sample with recent observational data at similar redshifts. In Section 4, we explore in detail the nature of the IRX- $\beta_{UV}$  relation and investigate the various contribution to the *intrinsic* scatter of this relation. In Section 5, we compare this intrinsic scatter with the uncertainties of  $\beta_{UV}$  and  $L_{IR}$  measurements of high- $z$  galaxies. We summarise the findings of this paper and conclude in Section 6. Throughout this paper, we adopt cosmological parameters in agreement with the nine-year data from the Wilkinson Microwave Anisotropy Probe (Hinshaw et al. 2013), specifically  $\Omega_m = 0.2821$ ,  $\Omega_\Lambda = 0.7179$ , and  $H_0 = 69.7 \text{ km s}^{-1} \text{ Mpc}^{-1}$ .

## 2 SIMULATION METHODOLOGY

In this section, we introduce the simulation methodology. In Section 2.1, we briefly introduce the simulation suites from which our galaxy sample is extracted. And in Section 2.2, we summarise the methodology of the dust RT analysis on our galaxy sample.

### 2.1 Simulation setup and galaxy catalogue

We adopt the galaxy sample ( $M_* \approx 10^9 - 10^{12} M_\odot$ ) extracted from the MASSIVEFIRE cosmological ‘zoom-in’ suite (Feldmann et al. 2016, 2017), which is part of the Feedback in Realistic Environments (FIRE) project<sup>3</sup> (Hopkins et al. 2014). The simulation methodology of MASSIVEFIRE has been described in the above papers, and we refer the interested readers to them for more details. We summarise only the salient points here.

The MASSIVEFIRE simulations are run with the gravity-hydrodynamics code GIZMO<sup>4</sup> (FIRE-1 version) in the Pressure-energy Smoothed Particle Hydrodynamics (“P-SPH”) mode (Hopkins 2013; Hopkins 2015). The initial conditions of the simulations are generated using the MUSIC (Multi-Scale Initial Conditions) code (Hahn & Abel 2011) within the periodic simulation boxes of the low-resolution (LR) dark matter (DM)-only runs with the WMAP cosmology (Hinshaw et al. 2013). From the outputs of the LR runs, we select a number of model halos to resimulate at much higher resolution and with baryons included. The selected halos have a variety of masses, accretion history, and environmental overdensities.

The catalogue used for this paper includes 18 massive halos selected from a  $(100 \text{ Mpc h}^{-1})^3$  comoving simulation box at  $z_{\text{final}} = 2$  (from Series A, B, and C in Feldmann et al. 2017) and 11 additional massive halos selected from two larger boxes ( $400$  and  $762 \text{ Mpc h}^{-1}$  on a side) at  $z_{\text{final}} = 6$  (Liang et al. 2019). Initial conditions for the ‘zoom-in’ runs are set up with a convex hull surrounding all particles within  $3R_{\text{vir}}$  at  $z_{\text{final}}$  of the chosen halo defining the Lagrangian high-resolution (HR) region following the method introduced by Hahn & Abel (2011). The mass resolution of the HR runs for dark matter and gas particles are  $m_{\text{DM}} = 1.7 \times 10^5 M_\odot$  and  $m_{\text{gas}} = 3.3 \times 10^4 M_\odot$ , respectively. The most massive progenitors (MMPs) of the galaxies are identified using the AMIGA Halo Finder (Gill et al. 2004; Knollmann & Knebe 2009).

<sup>3</sup> [fire.northwestern.edu](http://fire.northwestern.edu)

<sup>4</sup> A public version of GIZMO is available at <http://www.tapir.caltech.edu/phopkins/Site/GIZMO.html>

The simulations incorporate various gas cooling processes (free-free, photoionization/recombination, Compton, photoelectric, metal-line, molecular and fine-structure processes) and a uniform UV background using the FG09 model (Faucher-Giguère et al. 2009), and self-consistently account for 11 separately tracked metal species. Star formation occurs in self-gravitating, dense and self-shielding molecular gas based on a sink-particle prescription. Specifically, gas that is locally self-gravitating and has density exceeding  $n_{\text{crit}} = 5 \text{ cm}^{-3}$  is assigned an SFR  $\dot{\rho}_* = f_{\text{mol}} \rho_{\text{gas}} / t_{\text{ff}}$ , where  $t_{\text{ff}}$  is the local free-fall time of gas and  $f_{\text{mol}}$  is the self-shielding molecular mass fraction calculated following Krumholz & Gnedin (2011). Due to the self-gravity criterion, the mean gas density at which star formation occurs is actually significantly higher ( $\sim 100 \text{ cm}^{-3}$  for the resolution of the simulations) than  $n_{\text{crit}}$ .

The initial mass of a star particle is set to be equal to the mass of the parent gas particle from which it is spawned. Once the star particle is formed, it acts as a single stellar population (SSP) with given metallicity and age. The simulations explicitly incorporate several different stellar feedback channels including (1) local and long-range momentum flux from radiative pressure, (2) energy, momentum, mass, and metal injection from supernovae (Types Ia and II), (3) and stellar mass-loss (both OB and AGB stars), and (4) photoionization and photoelectric heating processes. The relevant stellar feedback quantities are tabulated in the simulations based on the stellar population model STARBURST99 (hereafter SB99) with a Kroupa initial mass function (IMF) (Leitherer et al. 1999), without subsequent adjustment or fine-tuning. We refer the readers to Hopkins et al. (2014) for details of the feedback prescriptions.

FIRE simulations have successfully reproduced a variety of observed galaxy properties relevant for this work, including the stellar-to-halo-mass relation (Hopkins et al. 2014; Feldmann et al. 2017), the sSFRs of galaxies at the cosmic noon ( $z \sim 2$ ) (Hopkins et al. 2014; Feldmann et al. 2016), the gas-phase and stellar mass-metallicity relation (Ma et al. 2016a), the submm flux densities at  $850 \mu\text{m}$  (Liang et al. 2018), the observational effective dust temperatures at  $z \sim 2$  (Liang et al. 2019) as well as the UV luminosity functions and cosmic star formation rate density at  $z > 5$  (Ma et al. 2019).

## 2.2 Predicting dust SED with SKIRT

We generate the UV-to-mm continuum SEDs for the galaxy catalogue using SKIRT<sup>5</sup>, an open-source<sup>6</sup> 3D Monte Carlo dust RT code (Baes et al. 2011; Baes & Camps 2015; Camps & Baes 2015). SKIRT provides full treatment of absorption and multiple anisotropic scattering by dust, and self-consistently computes the dust thermal re-emission and the dust temperature distribution for various astrophysical systems. To prepare our galaxy snapshots as RT input models, we follow the prescription of Camps et al. (2016) (see also Trayford et al. 2017; Camps et al. 2018). Here we only summarise the main points of the prescription and refer the readers to the above-mentioned papers for the details.

For the radiative transfer (RT) analysis, each star particle is treated as a SSP, and a spectrum is assigned to each star particle according to the age, initial metallicity, and initial mass of the particle. The RT calculations are performed based on an equally spaced logarithmic wavelength grid ranging from  $\lambda = 0.05 - 1000 \mu\text{m}$ . We launch  $10^6$  photon packages for each point in the wavelength

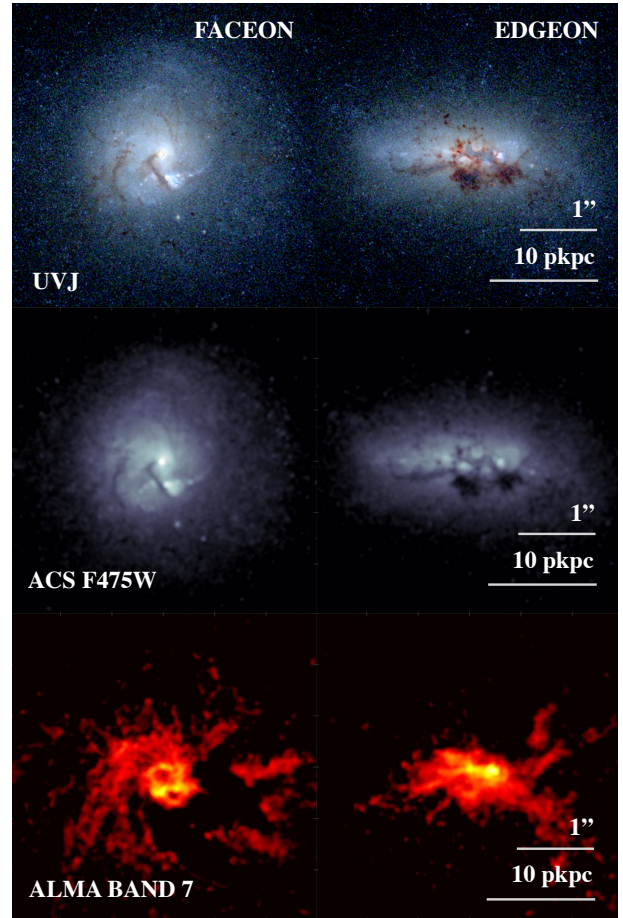


**Figure 1.** Synthetic images of a disc-like MASSIVEFIRE galaxy at  $z = 2$  for face-on (left panels) and edge-on (right panels) viewing directions. The top, middle and bottom panels show the composite UVJ, the *HST* ACS F475W-band, and the ALMA band 7 images, respectively.

grid and for each of the stellar emission and following dust emission phases. To produce the mock images and SEDs of galaxies, we place mock detectors at an arbitrary “local” distance of 10 Mpc from galaxy along different viewing angles to accumulate both spatially resolved as well as integrated fluxes at each wavelength grid point.

Dust mass is assumed to trace metal mass in the ISM. We discretise the spatial domain using an octree grid and keep subdividing grid cells until the cell contains less than  $f = 3 \times 10^{-6}$  of the total dust mass and the *V*-band ( $0.55 \mu\text{m}$ ) optical depth in each cell is less than unity. The highest grid level corresponds to a cell width of  $\sim 20 \text{ pc}$ , *i.e.* about twice the minimal SPH smoothing length. Gas hotter than  $10^6 \text{ K}$  is assumed to be dust-free because of sputtering (Hirashita et al. 2015). We self-consistently calculate the self-absorption of dust emission and include the transient heating function to calculate non-local thermal equilibrium (NLTE) dust emission by transiently heated small grains and PAH molecules (Baes et al. 2011; Camps et al. 2015). To account for the heating of dust by the cosmic microwave background (CMB), we adopt a correction to the dust temperature following Eq. 12 of da Cunha et al. (2013).

To understand how several uncertainties in the stellar population and dust properties of high- $z$  galaxies can influence the IRX- $\beta_{\text{UV}}$  relation of galaxies, we run several series of RT simulations with different parametrisation of inputs for each galaxy in

<sup>5</sup> SKIRT home page: <http://www.skirt.ugent.be>.

<sup>6</sup> SKIRT code repository: <https://github.com/skirt>

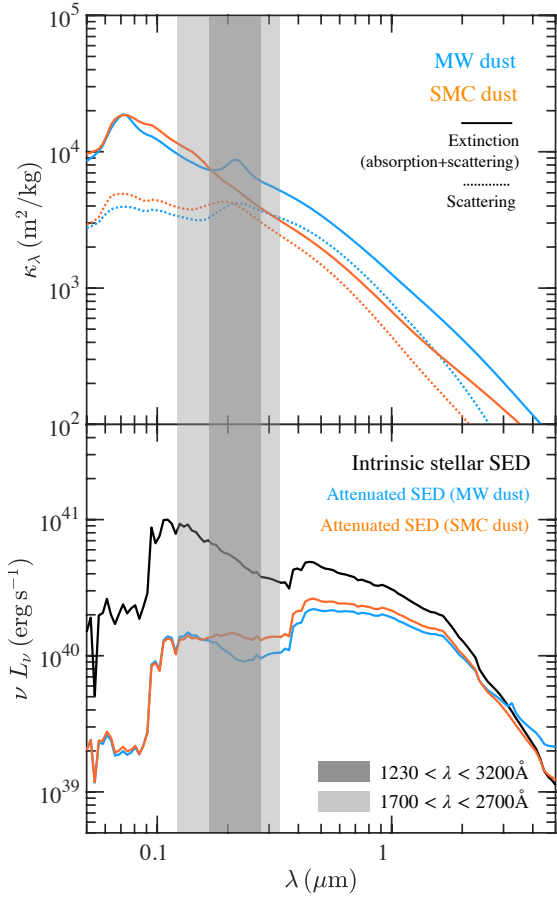


**Figure 2.** *Upper panel:* Dust extinction (absorption+scattering, solid lines) and dust scattering curves (dotted lines) of the Weingartner & Draine (2001) dust models. The blue and orange lines correspond to the Milky Way (MW) and SMC dust models, respectively. *Lower panel:* The SEDs of a selected  $z = 2$  MASSIVEFIRE galaxy. The black line indicates the intrinsic stellar SED of this galaxy. The blue and orange lines show the dust-attenuated SEDs for a selected viewing angle that are computed with SKIRT using the MW and SMC dust models, respectively. The light grey area in both panels show the wavelength range  $1230 < \lambda < 3200 \text{ \AA}$ , within which the measured photometry are used for estimating  $\beta_{\text{UV}}$  by the different studies. The dark grey area marks the regime of the ‘bump’ feature in the MW extinction curve. The derived  $\beta_{\text{UV}}$  can differ significantly depending on whether the photometry within this regime is included or not if a ‘bump’ feature exists.

our sample. This includes a change in 1) dust extinction law (due to different grain composition and grain size distribution, see Section 4.5.1), 2) the dust-to-metal mass ratio ( $\delta_{\text{dzt}}$ , see Section 4.5.3) and 3) the stellar population model (single vs. binary stellar evolution, see Section 4.5.4). In the *default* RT model, we adopt the SB99 SED libraries, the Milky Way (MW) dust model of Weingartner & Draine (2001, hereafter WD01) (for the case of  $R_V = 3.1$ , see Fig 2 for the shape of the extinction curve of this model), and assume a constant  $\delta_{\text{dzt}} = 0.4$  (Dwek 1998; Draine et al. 2007; Li et al. 2019). In addition to these runs, we also perform three additional RT calculations for each galaxy, with alternative choice for the stellar population model (BPASS, Eldridge & Stanway 2012; Eldridge et al. 2017), dust model (SMC dust of WD01, see Fig. 2), and  $\delta_{\text{dzt}}$  (0.2 and 0.8), with the other input parameters fixed. We compare the difference in the IRX- $\beta_{\text{UV}}$  relation caused by each of the three changes in the RT model in Section 4.5. Unless stated otherwise, we refer to the results of the default model throughout the paper.

Finally, we note that while our simulations have better resolu-

tion than many previous simulations modelling dust extinction and emission (e.g., Jonsson et al. 2006; Narayanan et al. 2010; Hayward et al. 2011; De Looze et al. 2014; Camps et al. 2016) and can directly incorporate various important stellar feedback processes, they might still be unable to resolve the emission from H II and photodissociation regions (PDR) from some of the more compact birth-clouds surrounding star-forming cores. The time-average spatial scale of these H II+PDR regions typically varies from  $\sim 5$  to  $\sim 800$  pc depending on the local physical conditions (Jonsson et al. 2010). Therefore, we also perform additional RT calculations, where star particles are split into two sets according to their age. Star particles that formed less than 10 Myrs ago are identified as ‘young star-forming’ particles, while older star particles are treated as in the default model. To account for the pre-processing of radiation by birth-clouds, we follow Camps et al. (2016) in assigning a source SED from the MAPPINGSIII (Groves et al. 2008) family to young star-forming particles. Dust associated with the birth-clouds is removed from the neighbouring gas particles to avoid double-counting (see Camps et al. 2016). We will discuss the effect of the variations in the conditions of the birth-clouds on the IRX- $\beta_{\text{UV}}$  relation in Section 4.5.5.

We show in Fig. 1 the synthetic images produced by SKIRT on one of our MASSIVEFIRE galaxies (galaxy ID: MF A2:0, Feldmann et al. 2016, 2017) at  $z = 2$  for both face-on (left panels) and edge-on viewing directions (right panels). In particular, we show composite U, V, J false-colour images (top panels), images of the flux densities at *Hubble Space Telescope* (HST) ACS-F475W band (middle panels) and ALMA band 7 (bottom panels). The broadband flux densities are calculated by convolving the simulated SED output from SKIRT with the transmission function of each band filter. The HST ACS-F475W band corresponds to rest-frame  $\lambda \approx 1600 \text{ \AA}$  at  $z = 2$ , i.e. in the far-ultraviolet (FUV) regime. The regions of higher dust extinction in the UV/optical corresponds to the most luminous regions at submm wavelength due to dust thermal emission.

We compute  $L_{\text{IR}}$  of the MASSIVEFIRE galaxies by integrating the simulated SEDs over the wavelength range  $\lambda = 8 - 1000 \mu\text{m}$ . Without explicit notification,  $\beta_{\text{UV}}$  is calculated using the flux densities measured at rest-frame  $\lambda = 1230$  and  $3200 \text{ \AA}$  to avoid the contamination by the  $2175 \text{ \AA}$  ‘bump’ feature (indicated by dark grey area in Fig. 2, see also Behrens et al. 2018) in the MW extinction curve, i.e.

$$\beta_{\text{UV}} = \frac{\log(f_{\lambda, 0.12}) - \log(f_{\lambda, 0.32})}{\log(\lambda_{0.12}) - \log(\lambda_{0.32})} \quad (1)$$

where  $f_{\lambda, 0.12}$  and  $f_{\lambda, 0.32}$  are the specific flux (in units of  $\text{erg s}^{-1} \text{ m}^{-3}$ ) at  $\lambda = 1230$  and  $3200 \text{ \AA}$ , respectively. Throughout the paper, we adopt the MW and SMC dust models of WD01; However, we note that the dust properties (i.e. composition and grain size distribution) and the resulting shape of the dust extinction curve of high- $z$  galaxies are uncertain (Stratta et al. 2007; Zafar et al. 2011; Salim & Narayanan 2020), in particular the strength of the ‘bump’ feature at around  $\lambda = 2175 \text{ \AA}$  (Kriek & Conroy 2013; Ma et al. 2015, 2017; Narayanan et al. 2018b).

### 3 COMPARING SIMULATIONS WITH OBSERVATIONS

In this section, we compare the predicted IRX vs.  $\beta_{\text{UV}}$  relation of the MASSIVEFIRE sample with recent observational data. We first introduce the ‘canonical’ relations derived using local starburst galaxies in Section 3.1. In Section 3.2, we compare the simulation

data with the stacked data derived using the high- $z$  Lyman-break galaxy (LBG) samples. And in Section 3.3, we compare it with the data of IR-selected samples. We also discuss secondary dependences of the IRX vs.  $\beta_{UV}$  relation and the impact of selection effect in observation of galaxies in Section 3.3.

### 3.1 The canonical relation of local starbursts

The relation between IRX and  $\beta_{UV}$  of galaxies was first derived based on a sample of  $\sim 60$  nearby compact starbursts (M99). In this work,  $\beta_{UV}$  was measured using the *International Ultraviolet Explorer* (*IUE*) satellite (Kinney et al. 1993), while far-IR luminosity (over  $40 \leq \lambda \leq 120 \mu\text{m}$ ) were extrapolated from the two-band (60 and  $100 \mu\text{m}$ ) photometry measured by the *Infrared Astronomical Satellite* (*IRAS*). Since then, IRX is defined more often using the bolometric IR luminosity in the literature, which includes emission over a larger wavelength range of  $8 \leq \lambda \leq 1000 \mu\text{m}$ . The revision of the definition of IRX results in an increase of IRX by 0.15 dex with respect to the original equation (e.g. Calzetti et al. 2000), Eq. 10 of M99. With the new definition, the equation is revised to be

$$\log \text{IRX} = \log(10^{0.4(4.43+1.99\beta_{UV})} - 1) + 0.076. \quad (2)$$

Hereafter, we refer to this relation as the ‘M99 relation’ in this paper. Given that this result has widely been adopted for correcting dust-attenuated SFRs of galaxies over a range of redshifts by many different studies, we also refer to it as the ‘canonical relation’, as in many other previous works.

One major problem with the M99 relation is that the UV fluxes measured with the *IUE* satellite were incomplete due to its limited aperture size ( $10'' \times 20''$ ), which is typically much smaller than the full spatial extent of a local galaxy ( $\sim$ arcmins). Hence,  $L_{UV}$  were underestimated and because *IUE* had focused only on the galaxies’ core regions, a colour bias of  $\beta_{UV}$  was introduced because of the colour gradient. The same sample was later remeasured using the *Galaxy Evolution Explorer* (*GALEX*; Morrissey et al. 2007) by other groups (Overzier et al. 2011; Takeuchi et al. 2012; Casey et al. 2014b), which has a much larger aperture size. These studies find lower IRX and redder  $\beta_{UV}$  of the exact same galaxies generally. We quote here the relation derived by Overzier et al. (2011)

$$\log \text{IRX} = \log(10^{0.4(4.54+2.07\beta_{UV})} - 1) + 0.225. \quad (3)$$

Hereafter, we will refer to Eq. 3 as the ‘M99<sub>corr</sub> relation’ in the paper, which stands for ‘aperture-corrected M99 relation’, to distinguish it from the original result derived by M99 (Eq. 2).

### 3.2 The high- $z$ IRX- $\beta$ relation

#### 3.2.1 The results derived by UV-selected galaxies

The majority of the current observational constraints on the IRX- $\beta_{UV}$  relation at high- $z$  are derived using LBG samples due to the efficiency of the selection methods (Steidel et al. 1996). Most studies have reported stacked results due to the difficulty in getting reliable detection of the dust continuum of many individual sources.

In the *left* panel of Fig. 3, we show the stacked results of the LBG samples at  $1.5 \lesssim z \lesssim 4$  obtained by Heinis et al. (2013) (yellow-edged triangles), Bouwens et al. (2016) (orange-edged hexagram), Álvarez-Márquez et al. (2016) (red-edged asterisks), Reddy et al. (2018) (blue-edged diamonds), McLure et al. (2018) (pink-edged circles) and Fudamoto et al. (2020) (cyan-edged squares). In these

studies, galaxies are binned by their measured  $\beta_{UV}$ , which are determined by fitting the power-law,  $f_{\lambda} \propto \lambda^{\beta_{UV}}$ , to the available UV photometry over different wavelength ranges between rest-frame 1200 Å and 3200 Å. For each bin, an IRX is extrapolated using the stacked UV and IR photometry of the objects in that bin. Specifically,  $L_{UV}$  ( $\equiv \lambda_{0.16} L_{\lambda, 0.16}$ ) is extrapolated from the best-fit power-law function at  $\lambda = 1600 \text{ Å}$ , while  $L_{IR}$  is derived by fitting the assumed dust SED templates (e.g. Dale & Helou 2002) or MBB functions (see e.g. Casey 2012; Casey et al. 2014a) to the available stacked *Herschel* or ALMA broadband fluxes. We summarise the detailed methodology for deriving  $\beta_{UV}$ ,  $L_{UV}$  and  $L_{IR}$  used by each study in Table 1.

Looking at the *left* panel, we can see that these studies have reported fairly diverse results of IRX- $\beta_{UV}$  relation. Specifically, McLure et al. (2018) and Fudamoto et al. (2020) show fairly blue  $\beta_{UV}$  and the derived relations agree with the canonical M99 relation (dotted black line). The relations by Heinis et al. (2013), Bouwens et al. (2016) and Reddy et al. (2018), however, are more compatible with the corrected M99 relation (solid black line). And yet the relation by Álvarez-Márquez et al. (2016) appears to be significantly ‘redder’ than the other observations and shows shallower slope compared to the M99 or M99<sub>corr</sub> relations. The shape of this curve resembles the expected relation of a SMC-type dust extinction curve (see Section 4.1).

The evolution of the IRX- $\beta_{UV}$  relation can be interpreted as a sign of change in stellar population age or the shape of attenuation curve (e.g. Salim & Narayanan 2020, and see references therein), and the difference in the derived relation can obviously lead to different estimate of such changes. However, it should also be noted that the uncertainties in the measurements of both  $\beta_{UV}$  and IRX can be non-trivial, which makes the interpretation of the observed evolution of the IRX- $\beta_{UV}$  relation challenging. Specifically, it can be seen from Table 1 that different studies have adopted different photometry spanning over different wavelength range for estimating  $\beta_{UV}$  and  $L_{UV}$  of their sample. Álvarez-Márquez et al. (2016), for example, have only adopted the photometry blueward to  $\lambda = 2000 \text{ Å}$ , which is significantly shorter compared to the upper limit of the other studies. This can lead to non-negligible difference in the estimated  $\beta_{UV}$ , because the true SED shape can deviate from a simple power-law (i.e.,  $f_{\lambda} \propto \lambda^{\beta_{UV}}$ , and see the *lower* panel of Fig. 2 for an example of the SEDs produced by using the dust extinction curves of the WD01 model), which most studies have assumed. We will explore this issue in more details in Section 5.1.

Apart from that, we note that different studies have adopted different *Herschel*/ALMA photometry as well as different fitting techniques for extrapolating  $L_{IR}$ , as summarised in Table 1. While some studies have fit different dust SED templates to the stacked fluxes at multiple IR-to-mm bands (e.g., Heinis et al. 2013; Álvarez-Márquez et al. 2016; Reddy et al. 2018), others also have derived  $L_{IR}$  by fitting single-band stacked flux densities with an assumed template SED (e.g., Fudamoto et al. 2020) or MBB function with an assumed ‘dust temperature’ (e.g., Bouwens et al. 2016; McLure et al. 2018). For those depending on single-band flux densities, the derived IRX therefore strongly depends on the assumed template or ‘dust temperature’. We therefore point out the implicit uncertainties in the results from the different studies due to the inconsistencies in the methodology for deriving  $L_{IR}$  and the limited constraint on the dust SED shape at high- $z$ .

One important issue about the stacked data is that they do not reflect the dispersion of individual sources, but instead, only represents the *luminosity-weighted* results. In the *right* panel of Fig. 3, we explicitly show the result of the individual source in

**Table 1.** The selection criteria and the methods for deriving  $L_{\text{IR}}$ ,  $L_{\text{UV}}$  and  $\beta_{\text{UV}}$  adopted by each observation that is referenced in Fig. 3 (Section 3.2).

Paper	Selection criteria of the sample	Methods for deriving $L_{\text{IR}}$ , $\beta_{\text{UV}}$ and $L_{\text{UV}}$
Heinis et al. (2013)	The sample contains 42,184 galaxies selected from the optical imaging of the COSMOS field (Capak et al. 2007) in the $u^*$ band ( $1.2 < z_{\text{phot}} < 1.7$ and $u^* < 26$ mag at $5\sigma$ ). The mean redshift of the sample is $\langle z_{\text{phot}} \rangle = 1.43$ .	$L_{\text{IR}}$ is derived from fitting the Dale & Helou (2002) SED templates to the stacked fluxes at 250, 350 and 500 $\mu\text{m}$ extracted from <i>Herschel</i> Space Observatory Spectral and Photometric Imaging Receiver (SPIRE, Griffin et al. 2010; Swinyard et al. 2010) imaging of the COSMOS field. $\beta_{\text{UV}}$ is computed by fitting the photometry to a single power-law SED, $f_{\lambda} \propto \lambda^{\beta_{\text{UV}}}$ . The rest-UV photometry is obtained from the Subaru $u^*$ and $V$ broad-band, 12 intermediate- and 2 narrow-band filters that cover the wavelength range $1200 < \lambda < 3000\text{\AA}$ . $L_{\text{UV}}$ is calculated at rest-frame 1600 $\text{\AA}$ using the best-fit SEDs.
Álvarez-Márquez et al. (2016)	The sample contains $\sim 22,000$ LBGs at $2.5 < z_{\text{phot}} < 3.5$ that are selected within the COSMOS field using broad-band filters $u^*$ , $V_j$ , and $i^+$ ( $V_j < 26.5$ and $i^+ < 26.1$ mag at $5\sigma$ ) and are included in the Ilbert et al. (2009, version 2.0) photometric redshift catalogue. The mean redshift of the sample is $\langle z_{\text{phot}} \rangle = 3.02$ .	$L_{\text{IR}}$ is estimated by fitting the Dale et al. (2014) SED templates to the stacked fluxes at <i>Herschel</i> Photodetector Array Camera and Spectrometer (PACS, Poglitsch et al. 2010) (100 and 160 $\mu\text{m}$ ) and SPIRE (250, 350 and 500 $\mu\text{m}$ ), and AzTEC (1.1 mm) bands. $\beta_{\text{UV}}$ is computed by fitting the power-law SED to the rest-UV photometry within the wavelength range $1250 < \lambda < 2000\text{\AA}$ from the Capak et al. (2007) catalogue. The photometry is obtained using the Subaru $B_j$ , $V_j$ , $g^+$ , $r^+$ , $i^+$ , $z^+$ broad-band, 12 intermediate- and 2 narrow-band filters. $L_{\text{UV}}$ is calculated at rest-frame 1600 $\text{\AA}$ from the best-fit SEDs.
Bouwens et al. (2016)	The sample includes 330 LBGs spanning the redshift range $2 < z_{\text{phot}} < 10$ selected from the <i>Hubble Ultra-Deep Field</i> (HUDF) via dropout technique.	$L_{\text{IR}}$ is inferred from converting the stacked ALMA 1.2 mm fluxes by a standard modified blackbody function with a dust temperature of 35 K and a power-law spectral index for dust emissivity of $\beta_{\text{IR}} = 1.6$ . $\beta_{\text{UV}}$ of the galaxies is estimated by fitting the <i>HST</i> photometry in various bands (from ACS-F606W to WFC3-F160W) to the power-law SEDs. $L_{\text{UV}}$ is calculated from the best-fit SEDs at 1600 $\text{\AA}$ .
McLure et al. (2018)	The sample consists of the star-forming galaxies at $2 < z_{\text{phot}} < 3$ within the deep 1.2-mm ALMA mosaic ( $35 \mu\text{Jy beam}^{-1}$ at $1\sigma$ ) of the HUDF presented by Dunlop et al. (2017). The UV-to-MIR photometry were assembled from the Great Observatories Origins Deep Survey-South (GOODS-S) (Guo et al. 2013) and the Ultra-Deep Survey (UDS) (Galametz et al. 2013) catalogues provided by the Cosmic Assembly Near-infrared Deep Extragalactic Legacy Survey (CANDELS) team, incorporated with the catalogue for the Unlra-Visible and Infrared Survey Telescope for Astronomy (UVISTA) survey Data Release 3 (DR3) (Mortlock et al. 2017).	$L_{\text{IR}}$ is estimated from converting the 1.2-mm flux, assuming an optically thin modified blackbody spectrum with a dust temperature of 35 K and a dust emissivity index of $\beta_{\text{IR}} = 1.6$ . $\beta_{\text{UV}}$ is determined by fitting the photometry from the GOOD-S, UDS and UVISTA catalogues that cover the wavelength range $1268 < \lambda < 2580\text{\AA}$ with the power-law SED. $L_{\text{UV}}$ is calculated from the best-fit SEDs at 1600 $\text{\AA}$ .
Reddy et al. (2018)	The sample contains $\sim 3,500$ galaxies at $1.5 \leq z_{\text{phot}} \leq 2.5$ extracted from the ground- and space-based photometry compiled by the 3D- <i>HST</i> survey (Skelton et al. 2014) with newly obtained imaging from the HDUV Legacy Survey (Oesch et al. 2018) in the GOODS-N and GOODS-S fields. The UV and optical depth of the sample are $H \approx 27$ and $m_{\text{UV}} \approx 27$ , respectively. Objects identified as X-ray active galactic nucleus (AGN) (Shao et al. 2010; Xue et al. 2011) or classified as quiescent galaxies by the UVJ method (Williams et al. 2009) are excluded.	$L_{\text{IR}}$ is derived by fitting the Elbaz et al. (2011) main-sequence dust SED template to the stacked fluxes at 100 and 160 $\mu\text{m}$ obtained from the <i>Herschel</i> /PACS imaging. $\beta_{\text{UV}}$ is computed by fitting the power-law function to the broadband photometry covering the wavelength range of $1268 < \lambda < 2580\text{\AA}$ . $L_{\text{UV}}$ is calculated from the best-fit SEDs at 1600 $\text{\AA}$ .
Fudamoto et al. (2020)	The sample includes 1,512 galaxies at $2.5 < z_{\text{phot}} < 4$ selected from the COSMOS2015 catalogue (Laigle et al. 2016) that are part of the ALMA archival band 6 and 7 observations that were publicly available as of January 2018. The COSMOS2015 catalogue are extracted from a combined near-IR image from the UltraVISTA survey ( $J$ , $H$ , $K$ bands, McCracken et al. 2012) and the $z^+$ image from the Subaru telescope.	$L_{\text{IR}}$ is estimated by scaling a dust SED template, which is previously derived for $z \sim 3$ galaxies by Álvarez-Márquez et al. (2016), to the stacked fluxes in ALMA band 6 or 7 of the sample. $\beta_{\text{UV}}$ is estimated by employing SED fitting to photometric data over the wavelength range of $1500 < \lambda < 2500\text{\AA}$ . $L_{\text{UV}}$ is calculated from the best fit SEDs at 1600 $\text{\AA}$ .

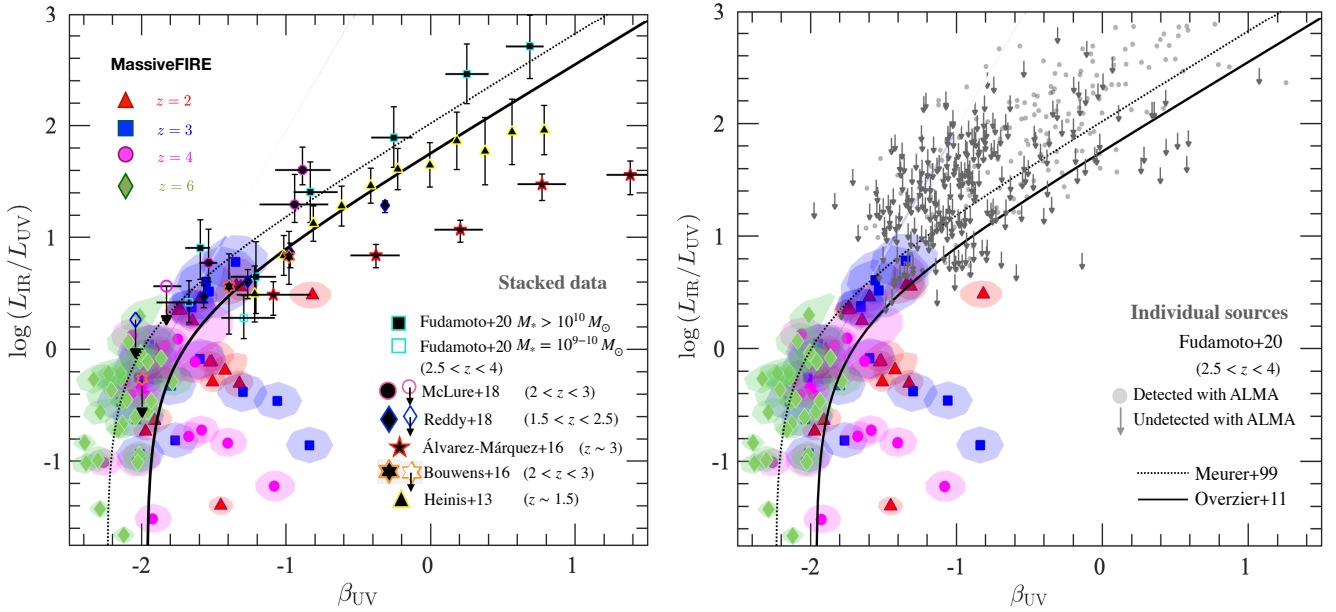


**Figure 3.** Comparison between the IRX- $\beta_{UV}$  relation of the MASSIVEFIRE galaxies with the recent observational data derived using UV-selected samples. In both panels, red triangles, blue squares, magenta circles and green diamonds correspond to the MASSIVEFIRE sample at  $z = 2$ ,  $z = 3$ ,  $z = 4$  and  $z = 6$ , respectively. The contour around each data point indicates the  $3\sigma$  (*i.e.* 99.8% confidence level) distribution of the result of 24 randomly selected viewing directions. In the *left* panel, the observational data are stacked results, including Heinis et al. (2013) (yellow-edged triangles), Álvarez-Márquez et al. (2016) (red-edged stars), Bouwens et al. (2016) (orange hexagram), McLure et al. (2018) (magenta-edged circles), Reddy et al. (2018) (blue-edged diamonds) and Fudamoto et al. (2020) (cyan-edged squares). The results of the individual sources in the Fudamoto et al. (2020) sample are explicitly shown in the *right* panel. The ALMA-detected objects are indicated by grey dots whereas the  $3\sigma$  upper confidence limit of the non-detected objects in the sample are marked with grey downward arrows. In both panels, the dotted and solid black lines indicate the original and the aperture-corrected M99 relations derived using the local starburst samples, respectively (Section 3.1). While the majority of MASSIVEFIRE galaxies are in broad agreement with the local M99 relation, a number of them appear to be noticeably below (or rightwards) due to the recent quenching of star formation in those galaxies (Section 4.4). The stacked results derived from the various LBG samples exhibit non-trivial discrepancies among different studies. The majority ( $\sim 90\%$ ) of the LBGs in these samples are not individually resolved by ALMA.

the Fudamoto et al. (2020) sample as an example. The sample of Fudamoto et al. (2020) contains 1512 galaxies selected from the COSMOS2015 catalogue (Laigle et al. 2016) that are part of the ALMA archival band 6 and 7 observations. 172 out of 1512 galaxies (11.4%) are detected with more than  $3\sigma$  with ALMA. In the figure, the data of the detected sources and the  $3\sigma$  (*i.e.* 99.8%) upper limits of the undetected objects are marked with grey filled circles and grey downward arrows, respectively.

The scatter among individual sources is non-trivial. The IRX of the ALMA-detected objects has a dispersion as large as  $\sim 0.3$  dex at given  $\beta_{UV}$ . Since the IRX and  $\beta_{UV}$  of all the objects in the same sample are measured using the same methodology, the scatter present in the figure is largely intrinsic. We also emphasise that the exact location of the undetected sources on the diagram is unknown and can in principle be offset from the  $M99_{\text{corr}}$  relation. Given their large population, the dispersion of the complete LBG sample of Fudamoto et al. (2020) is in fact uncertain. The stacked data, which is biased by the IR-luminous objects, appears to well agree with the canonical M99 relation (*left* panel), while the individual objects may deviate from it. This again highlights the issue that stacked results of the high- $z$  LBG samples may not reflect the distribution of the location of the individual sources in the IRX- $\beta_{UV}$  plane.

### 3.2.2 Comparing the simulation results with the observations

We now compare the prediction of MASSIVEFIRE with the observational data. In Fig. 3, we show the IRX- $\beta_{UV}$  relation of our MAS-

SIVEFIRE sample at  $z = 2 - 6$ . The coloured symbols represent the data that are averaged over 24 random viewing angles of each galaxy, and the semi-transparent coloured contours around those filled symbols indicate the  $3\sigma$  (*i.e.* 99.8% confidence level) probability distribution of the results of the different viewing angles. The redshifts of the galaxies are indicated by the colour and shape of the symbols as labeled. We show in this figure only the results of our fiducial RT model (SB99 stellar evolution model,  $\delta_{\text{dzt}} = 0.4$ , and the MW dust model of WD01, see Section 2.2).

From the figure, we can see that the simulated data exhibit fairly large scatter on the diagram. While a large fraction of the galaxies are in broad agreement with the canonical M99 relation, there are also a number of galaxies that appear to have significantly redder  $\beta_{UV}$  for their IRX (or significantly lower IRX at their  $\beta_{UV}$ ). To better quantify the location of galaxies on the diagram, we define the variable,  $\delta\beta_{UV}$ , as the horizontal offset of the galaxy’s UV spectral slope from the  $M99^7$  relation on the diagram, *i.e.*

$$\delta\beta_{UV} \equiv \beta_{UV} - \beta_{M99}(\text{IRX}), \quad (4)$$

where  $\beta_{M99}(\text{IRX})$  is the inverse function of Eq. 2.

<sup>7</sup> Although the original M99 relation has the problem of missing UV fluxes and colour bias in  $\beta_{UV}$  (see Section 3.1) and has been corrected by several subsequent works, we still use the uncorrected relation as the benchmark because it has been very widely adopted for correcting dust-obscured SFRs by many studies in the past.



We find that 54 out of 83 galaxies (66%, *i.e.*  $1\sigma$ ) in our sample at  $z = 2 - 6$  lie within  $\delta\beta_{UV} = \pm 0.2$ , while 21 (8) galaxies lie redwards (bluewards) to that region. The standard deviation of  $\delta\beta_{UV}$  of the entire sample is 0.32. We notice a mild redshift evolution of  $\delta\beta_{UV}$ , from a median value of  $-0.08$  at  $z = 6$  (green diamonds) to  $0.14$  at  $z = 2$  (red triangles). This is mainly driven by the increase of the intrinsic UV spectral slope ( $\beta_{UV,0}$ ) on average with decreasing redshift (see discussion in Section 4.4, and also *e.g.* Reddy et al. 2018). Note that this evolution from  $z = 6$  and  $z = 2$  (by 0.22) does not appear to be significant compared to the dispersion of the entire sample ( $1\sigma$  is 0.32) or that of any subsample of a given redshift. This is because  $\delta\beta_{UV}$  is strongly correlated to the very recent star formation history of galaxy on the timescale of  $\lesssim 100$  Myrs and galaxies at a given snapshot have large variations in the star formation history in the past on this timescale (see Section 4.4 for a more detailed discussion, and also Faucher-Giguère 2017; Feldmann et al. 2017; Sparre et al. 2017; Flores Velázquez et al. 2020).

The objects that are in broad agreement with the canonical M99 relation in our sample are therefore also in good agreement with the observational data at high- $z$  in the overlapping parameter space (*i.e.*,  $1 \lesssim \text{IRX} \lesssim 10$  and  $-2 \lesssim \beta_{UV} \lesssim -1$ , see the left panel of Fig. 3). On the other hand, a subset of our simulated galaxies lies well below the canonical M99 relation. They are quiescent galaxies with relatively low recent SFR as well as low dust optical depth (see Section 4). These objects are very faint at the ALMA bands and may constitute a considerable fraction of the submm undetected galaxies in the observations (see the right panel of Fig. 3) and may not be selected as LBGs.

We also note that variations due to different viewing angles do not appear to be as significant as galaxy-to-galaxy variations. The mean  $3\sigma$  dispersion of  $\beta_{UV}$  due to viewing angle variations in the MASSIVEFIRE sample is only 0.10, which is much smaller than the galaxy-to-galaxy dispersion. The viewing direction is thus not a major source of scatter in the observed IRX- $\beta_{UV}$  relation. In Section 4, we will assess the relative contribution of the different sources of the scatter in more detail, including stellar population age, viewing direction, as well as other parameter changes of the fiducial RT model.

Finally, we note that our sample does not completely cover the parameter space occupied by the observational data, specifically, at high IRX (*i.e.*,  $\text{IRX} \gtrsim 10$ ) and  $\beta_{UV}$  (*i.e.*,  $\beta_{UV} \gtrsim -1$ ). This arises because observational samples contain larger number of galaxies (typically, hundreds to thousands of sources, see Table 1) spanning a much wider dynamic range of properties. In particular, they include galaxies with higher dust optical depth, which explains the galaxies in the upper right corner of the diagram (see next section). It is noteworthy that, in practice, this is also the regime where IRX- $\beta_{UV}$  relation becomes useful for estimating dust-obscured SFR with UV data alone, because a small error in  $\beta_{UV}$  does not lead to a significant difference in the derived IRX (and hence  $L_{IR}$ ) for a given IRX- $\beta_{UV}$  relation.

### 3.3 The dependence of IRX- $\beta$ relation on $L_{IR}$

Several works in the recent years have studied the IRX- $\beta_{UV}$  relation at high- $z$  using galaxy samples selected at IR or submm bands. In contrast to the UV/optical-selected samples, which often do not have reliable detections of the IR emission from most of the sources, IR/submm-selected samples have nearly complete detections at rest-UV bands so that constraints on individual sources are possible. The general finding from these studies is that IR-

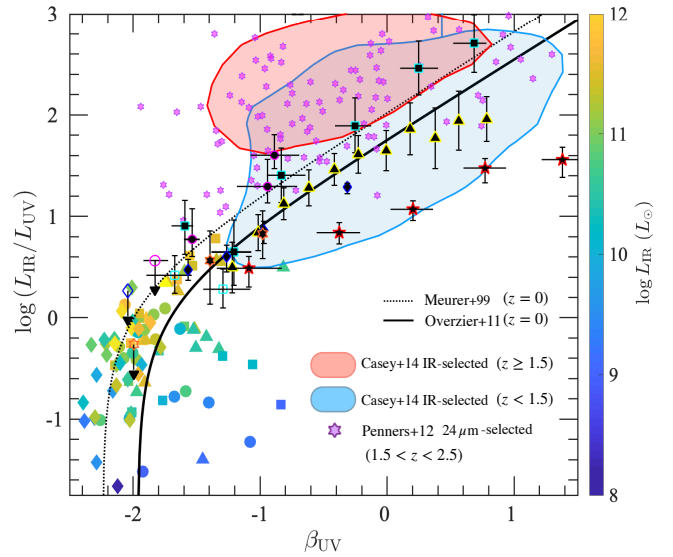


**Figure 4.** The ‘secondary dependence’ of the IRX- $\beta_{UV}$  relation on  $L_{IR}$ . The simulation data are angle-averaged results, and are colour-coded by  $L_{IR}$  of the galaxy. The redshifts of the galaxies (over the range of  $z = 2 - 6$ ) are indicated by the shape of the symbols as in Fig. 3. The magenta hexagrams represent the data derived by Penner et al. (2012) using a  $24 \mu\text{m}$ -selected galaxy sample at  $1.5 < z < 2.5$ , which spans  $10^{12} \lesssim L_{IR} \lesssim 10^{13} L_{\odot}$ . The red and blue shaded areas represent the  $1\sigma$  distribution of the *Herschel*-selected galaxies in the Casey et al. (2014b) sample within the redshift range  $1.5 \leq z < 3.5$  ( $\langle L_{IR} \rangle = 10^{12.5} L_{\odot}$ ) and  $0 < z < 1.5$  ( $\langle L_{IR} \rangle = 10^{11.5} L_{\odot}$ ), respectively. The local M99 and M99<sub>corr</sub> relations, as well as the stacked data of the UV-selected samples are the same as shown in the left panel of Fig. 3. The IR-selected samples at high- $z$  show bluer  $\beta_{UV}$  at given IRX compared to the UV-selected samples.

detected samples, on average, show bluer  $\beta_{UV}$  at given IRX than UV-selected samples.

Specifically, we show in Fig. 4 the data from two studies, Penner et al. (2012, hereafter P12) and Casey et al. (2014b, hereafter C14). P12 have adopted a sample of  $\sim 60$  galaxies at  $1.5 < z < 2.5$  selected at the *Spitzer*/*MIPS* band at  $24 \mu\text{m}$ , whereas C14 have used a much larger sample that contains  $> 4000$  *Herschel*-selected objects that span over a larger redshift range of  $0 < z < 3.5$  (see Table 2 for the details). We show the data of the individual sources of P12 by magenta asterisks in the figure. For the C14 sample, we separately show the result of the galaxies within two redshift ranges,  $0 < z < 1.5$  and  $1.5 \leq z < 3.5$ . Because of the large sample size of C14, we only show the  $1\sigma$  probability contours of the two redshift categories. The lower- (blue semi-transparent area) and higher- $z$  (red semi-transparent area) categories contain 3246 and 919 galaxies, respectively.

The IR-selected samples show a fairly large scatter in the relation similar to the UV-selected samples (right panel of Fig. 3). Comparing the data of the P12 sample and the high- $z$  data of C14 with the stacked results of the various UV-selected samples at similar redshifts, however, we see that the IR-selected samples have on average bluer  $\beta_{UV}$  at a given IRX (or high IRX at a given  $\beta_{UV}$ ). This discrepancy follows from the ‘secondary dependence’ of the IRX- $\beta_{UV}$  relation on  $L_{IR}$  — the horizontal deviation of a galaxy’s location from the canonical relation anti-correlates to  $L_{IR}$  (Casey et al. 2014b) — combined with the higher IR luminosities in the IR-selected sample. This ‘secondary dependence’ is reproduced by our simulations, as is shown in Fig. 4.

The trend that the high- $z$  population of C14 (red semi-

**Table 2.** The selection criteria and the methods for deriving  $L_{\text{IR}}$ ,  $L_{\text{UV}}$  and  $\beta_{\text{UV}}$  used by the two studies that are referenced in Fig. 4 (see also Section 3.3). Both studies analysed IR-selected samples.

Paper	Selection criteria of the sample	Methods for deriving $L_{\text{IR}}$ , $\beta_{\text{UV}}$ and $L_{\text{UV}}$
Penner et al. (2012)	The sample contains $\sim 60$ dust-obscured galaxies (DOGs, Dey et al. 2008) at $1.5 < z_{\text{phot}} < 2.5$ that are selected from a catalogue of $24 \mu\text{m}$ sources produced for the <i>Spitzer</i> /MIPS survey of the GOODS-N region (M. Dickinson: PI; Magnelli et al. 2011).	$L_{\text{IR}}$ is estimated by integrating the redshifted SED template from the Chary & Elbaz (2001) SED libraries that most closely matches the observed $100 \mu\text{m}$ flux density (measured by <i>Herschel</i> /PACS) over the wavelength range $\lambda = 8 - 1000 \mu\text{m}$ . $\beta_{\text{UV}}$ of the galaxies is derived by fitting the single power-law SED, $f_{\lambda} \propto \lambda^{\beta_{\text{UV}}}$ , to the $> 3\sigma$ flux densities measured in the $B$ , $V$ , $R$ , $I$ , and $z$ bands that are extracted from Subaru images (Capak et al. 2004). $L_{\text{UV}}$ is computed using the best-fit SED at $1600 \text{ \AA}$ .
Casey et al. (2014b)	The sample includes $> 4000$ <i>Herschel</i> -selected dusty star-forming galaxies (DSFGs) at $0 < z_{\text{phot}} < 3.5$ in the COSMOS field that have $> 3\sigma$ detection at two or more of the five PACS+SPIRE bands.	For each galaxy, a best-fit SED of the Casey (2012) functional form is found by fitting all the available IR-to-mm data at $\lambda = 8 - 2000 \mu\text{m}$ , and $L_{\text{IR}}$ is derived from integrating the best-fit SED over the range $\lambda = 8 - 1000 \mu\text{m}$ . $\beta_{\text{UV}}$ is calculated by fitting the power-law SED to the multiple photometric measurements available in the COSMOS that are in the $1230 - 3200 \text{ \AA}$ range. $L_{\text{UV}}$ is calculated at $1600 \text{ \AA}$ as in the other works.

transparent area) appears to be systematically above the low- $z$  population (blue semi-transparent area) is now easy to understand. Galaxies selected at higher redshifts are biased to higher  $L_{\text{IR}}$  (Casey et al. 2014a), and hence they appear to be offset from the low- $z$  counterparts in the upper left direction.

Finally, we note that our simulations do not reproduce some of the objects with extremely high IRX in the observational samples (P12 and C14), as can be seen from Fig. 4. Despite the uncertainties in the measurements of  $\beta_{\text{UV}}$  and  $L_{\text{IR}}$ , which we will discuss in Section 5 in detail, a straightforward interpretation is that our simulations do not produce as IR-luminous systems as the ones included in the observational samples. The galaxies in the P12 and C14 samples with  $\text{IRX} \gtrsim 2$  have on average  $L_{\text{IR}} \approx 10^{13} L_{\odot}$ , which exceeds the most luminous object in our sample by an order of magnitude. It should thus be emphasised that the apparent  $\text{IRX}-\beta_{\text{UV}}$  relation depends on the selection of the galaxy population.

#### 4 DISSECTING THE $\text{IRX}-\beta$ RELATION

In the last section, we have shown that both the simulation and observational data exhibit non-trivial scatter in the  $\text{IRX}-\beta_{\text{UV}}$  relation of high- $z$  galaxies. Therefore, in this section, we focus on examining the physical origins of the intrinsic scatter in this relation.

We start by analysing a simple dust slab model in Section 4.1, which provides useful insights into the nature of the  $\text{IRX}-\beta_{\text{UV}}$  relation. In Section 4.2, we reveal the role of the dust optical depth in driving this relation and show the tight correlation between dust optical depth and IRX of galaxies. In Section 4.3, we investigate the physical mechanisms that determine both properties. In Section 4.4, we analyse the evolutionary trajectories of galaxies in the  $\text{IRX}-\beta_{\text{UV}}$  plane. Finally, we discuss uncertainties in the stellar population and dust models and estimate their impact on the resulting  $\text{IRX}-\beta_{\text{UV}}$  relation in Section 4.5.

##### 4.1 Physical insights from the dust slab model

A simple toy model can often offer important physical insights into more complex physics problems. To understand the nature of the  $\text{IRX}-\beta_{\text{UV}}$  relation of high- $z$  galaxies, we at first derive this relation for a simplified model of a homogeneous dust slab intervening between a fixed stellar population and the observer (see Fig. 5 for a schematic plot of the model). The toy model does not capture two

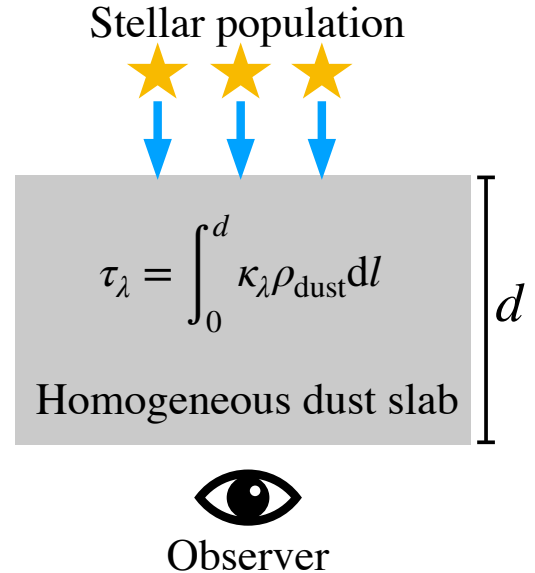


**Figure 5.** Schematic plot of the toy model of a homogeneous dust slab intervening between a fixed stellar population and the observer. For this toy model, the attenuation curve,  $\tau_{\lambda}$ , is simply a function of dust mass column density along the sightline.

major complexities in real galaxies — 1) stellar population and thus the intrinsic stellar SEDs evolve with time, and 2) the dust column density for each star particle in a galaxy is not a constant. This toy model, however, is sufficient to show the role that the optical depth plays in shaping the  $\text{IRX}-\beta_{\text{UV}}$  relation (e.g. Calzetti et al. 2000; Popping et al. 2017; Imara et al. 2018).

Energy balance implies that the  $L_{\text{IR}}$  emitted by dust equals to the amount of energy of the stellar light that is absorbed by dust per unit time. Therefore,  $\text{IRX} (\equiv L_{\text{IR}}/L_{\text{UV}})$  is equivalent to the ratio of the absorbed to the unabsorbed stellar radiation. For the dust slab model,  $L_{\text{IR}}$  can be expressed as

$$L_{\text{IR}} = L_{\text{abs}} = \int_0^{\lambda_{\text{max}}} (1 - e^{-\tau_{\lambda}}) L_{\lambda}^* d\lambda, \quad (5)$$

where  $L_{\text{abs}}$  is the stellar luminosity absorbed by the dust slab (in

units of  $\text{erg s}^{-1}$ ),  $\tau_\lambda$  is the dust optical depth at  $\lambda$ ,  $L_\lambda^*$  is the specific intrinsic luminosity of the fixed stellar population in the background (in units of  $\text{erg s}^{-1} \text{m}^{-1}$ ), and  $\lambda_{\text{max}}$  is the wavelength beyond which direct light from stars constitutes to the total emission at a negligible level ( $\approx 1 \mu\text{m}$ ). IRX can subsequently be expressed as

$$\text{IRX} = \frac{L_{\text{IR}}}{L_{\text{UV}}} = \frac{L_{\text{abs}}}{\lambda_{0.16} L_{\lambda, 0.16}} = \frac{\int_0^{\lambda_{\text{max}}} (1 - e^{-\tau_\lambda}) L_\lambda^* d\lambda}{\lambda_{0.16} (e^{-\tau_{0.16}} L_{\lambda, 0.16}^*)}, \quad (6)$$

where  $\tau_{0.16}$  represents the dust optical depth at  $\lambda_{0.16} = 1600 \text{ \AA}$ , and  $L_{\lambda, 0.16} (= e^{-\tau_{0.16}} L_{\lambda, 0.16}^*)$  and  $L_{\lambda, 0.16}^*$  correspond to the attenuated and unattenuated (intrinsic) specific luminosity of the stellar population at  $\lambda_{0.16} = 1600 \text{ \AA}$ , respectively.

By re-arrangement, Eq. 6 can be written as

$$\text{IRX} = \left( \frac{1 - e^{-\tau_{0.16}}}{e^{-\tau_{0.16}}} \right) \frac{\int_0^{\lambda_{\text{max}}} (1 - e^{-\tau_\lambda}) / (1 - e^{-\tau_{0.16}}) L_\lambda^* d\lambda}{L_{\lambda, 0.16}^* \lambda_{0.16}} = (e^{\tau_{0.16}} - 1) \mathcal{Y}, \quad (7)$$

where we define a new dimensionless parameter, *i.e.*

$$\mathcal{Y} \equiv \frac{\int_0^{\lambda_{\text{max}}} (1 - e^{-\tau_\lambda}) / (1 - e^{-\tau_{0.16}}) L_\lambda^* d\lambda}{L_{\lambda, 0.16}^* \lambda_{0.16}}. \quad (8)$$

It can immediately be seen from the above equation that  $\mathcal{Y}$  is dependent on both intrinsic stellar SED ( $L_\lambda^*$ ) as well as dust attenuation law ( $\tau_\lambda$ ). For a homogeneous dust slab,  $\tau_\lambda$  can be expressed as<sup>8</sup>

$$\tau_\lambda = \int_0^d \kappa_\lambda \rho_{\text{dust}} dl = \kappa_\lambda \rho_{\text{dust}} d = \kappa_\lambda N_{\text{dust}}. \quad (9)$$

$\tau_\lambda$  is simply a function of dust column mass density (*i.e.*,  $N_{\text{dust}} = \rho_{\text{dust}} d$ ), assuming the dust extinction curve<sup>9</sup>,  $\kappa_\lambda$ , is consistent everywhere in the slab.

Eq. 7 implies that if  $\mathcal{Y}$  shows a relatively small variation with different dust and stellar properties (*e.g.*  $\tau_\lambda$  and  $L_{*, \lambda}$ ), then IRX and  $\tau_{0.16}$  simply follow an exponential relation. Let us now consider two extreme conditions. First of all, when the dust optical depth is sufficiently small (*i.e.*  $\tau_\lambda \ll 1$ ), Eq. 8 can simplify to

$$\mathcal{Y} \approx \frac{\int_0^{\lambda_{\text{max}}} (\tau_\lambda / \tau_{0.16}) L_\lambda^* d\lambda}{L_{\lambda, 0.16}^* \lambda_{0.16}} = \frac{\int_0^{\lambda_{\text{max}}} \hat{\tau}_\lambda L_\lambda^* d\lambda}{L_{\lambda, 0.16}^* \lambda_{0.16}}. \quad (10)$$

It can be seen that  $\mathcal{Y}$  depends on both  $L_{*, \lambda}$  and the *normalised* attenuation curve, *i.e.*  $\hat{\tau}_\lambda = \tau_\lambda / \tau_{0.16}$ , but is independent of  $\tau_{0.16}$ .

<sup>8</sup> We neglect the light scattered back into the sightline from dust.

<sup>9</sup> In this paper, we use the term ‘dust extinction law (curve)’ to refer to the dust opacity function,  $\kappa_\lambda$ , which is in unit of  $\text{m}^2 \text{kg}^{-1}$ . We also frequently use the term ‘dust attenuation law (curve)’ to refer to the optical depth function,  $\tau_\lambda$ , which is dimensionless. For the dust slab model,  $\tau_\lambda$  is proportional to  $\kappa_\lambda$  and thus they have the same functional shape (Eq. 9).  $\tau_\lambda$  of a galaxy, however, does not necessarily have the same functional shape as  $\kappa_\lambda$ , depending on the spatial configuration of dust and star distribution (see *e.g.*, Salim & Narayanan 2020, and references therein). The terminology ‘law’ and ‘curve’ are interchangeably utilised in this paper.

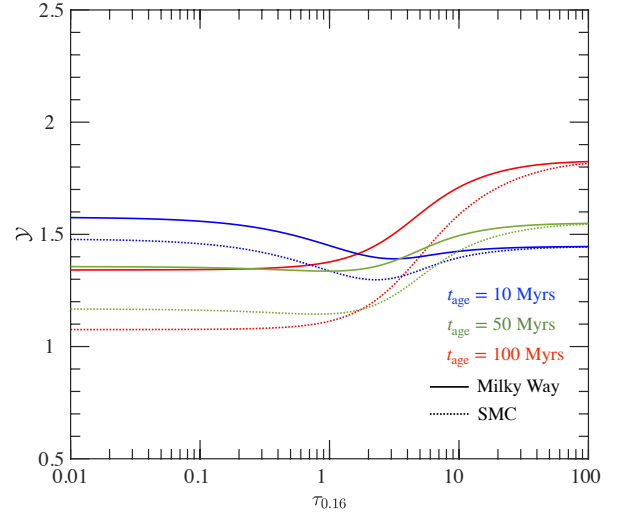


**Figure 6.**  $\mathcal{Y}$  parameter as a function of  $\tau_{0.16}$  (see Eq. 7 for the definition of  $\mathcal{Y}$ ) for various stellar population ages and dust extinction curves. The blue, green and red lines correspond to the cases of  $t_{\text{age}} = 10, 50$ , and  $100$  Myrs, respectively, with stellar metallicities  $Z_* = 0.1 Z_\odot$ . The stellar SEDs are extracted from the STARBURST99 template libraries based on  $t_{\text{age}}$  and  $Z_*$ . The results of the MW and SMC dust models of WD01 are shown by solid and dotted lines, respectively.  $\mathcal{Y}$  is a weak function of  $\tau_{0.16}$ .

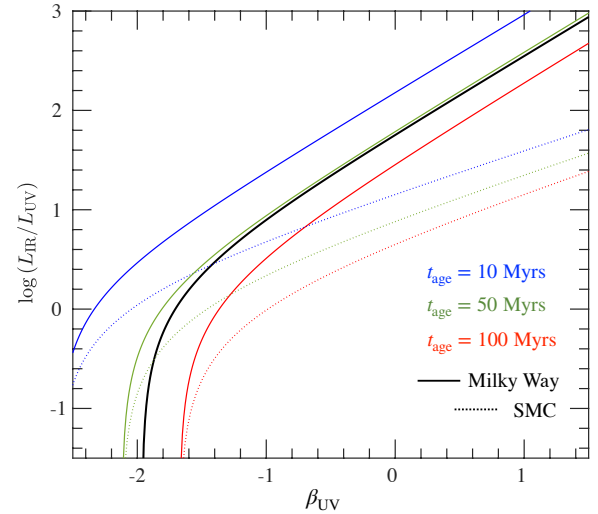


**Figure 7.** The analytic solution of IRX- $\beta_{\text{UV}}$  relation for the dust slab model (by using Eq. 17). The coloured lines correspond to the same models as in Fig. 6. The solid black line indicates the local M99<sub>corr</sub> relation.

On the other hand, when the dust slab is very optically thick (*i.e.*  $\tau_\lambda \gg 1$ ), Eq. 8 approximates to

$$\mathcal{Y} \approx \frac{\int_0^{\lambda_{\text{max}}} L_\lambda^* d\lambda}{L_{\lambda, 0.16}^* \lambda_{0.16}}. \quad (11)$$

In this case,  $\mathcal{Y}$  becomes the ratio of the total intrinsic stellar luminosity to  $L_{\lambda, 0.16}^* \lambda_{0.16}$ , the proxy for stellar UV luminosity. It is interesting to note that  $\mathcal{Y}$  is independent of the dust-related properties (neither  $\hat{\tau}_\lambda$  or  $\tau_{0.16}$  enters the equation).

Overall,  $\mathcal{Y}$  is a weak function of  $\tau_{0.16}$ . To illustrate this, we show the  $\mathcal{Y}$  vs.  $\tau_{0.16}$  relation for a number of different stellar SEDs ( $t_{\text{age}} = 10, 50$  and  $100$  Myrs with  $Z_* = 0.1 Z_\odot$ , extracted from the

SB99 libraries) and dust attenuation curves (yielded from the MW and SMC dust models of WD01) in Fig. 6. It is clear that for all the cases,  $\mathcal{Y}$  does not vary by more than a factor of 2 over four orders of magnitude in  $\tau_{0.16}$ . Therefore, for a dust slab model, IRX and  $\tau_{0.16}$  roughly follow the relation (*c.f.* Meurer et al. 1999; Calzetti et al. 2000; Safarzadeh et al. 2017b; Narayanan et al. 2018a)

$$\text{IRX} \propto e^{\tau_{0.16}} - 1. \quad (12)$$

The relation ensures that when  $\tau_{0.16} \rightarrow 0$ ,  $\text{IRX} \rightarrow 0$ , meaning that no light is reemitted by dust when the optical depth approaches zero.

Now we examine how  $\beta_{\text{UV}}$  relates to  $\tau_{0.16}$ . By definition,  $\beta_{\text{UV}}$  is set by the slope between FUV and NUV luminosity, both of which scale exponentially with optical depth as

$$L_{\lambda, \text{FUV}|\text{NUV}} = e^{-\tau_{\text{FUV}|\text{NUV}}} L_{\lambda, \text{FUV}|\text{NUV}}^*, \quad (13)$$

where  $L_{\lambda, \text{FUV}}$  ( $L_{\lambda, \text{NUV}}$ ) and  $L_{\lambda, \text{FUV}}^*$  ( $L_{\lambda, \text{NUV}}^*$ ) represent the attenuated and intrinsic specific stellar luminosity at a given FUV (NUV) band, respectively.  $\beta_{\text{UV}}$  can therefore be expressed as

$$\begin{aligned} \beta_{\text{UV}} &= \frac{\log(e^{-\tau_{\text{FUV}}} L_{\lambda, \text{FUV}}^*) - \log(e^{-\tau_{\text{NUV}}} L_{\lambda, \text{NUV}}^*)}{\log \lambda_{\text{FUV}} - \log \lambda_{\text{NUV}}} \\ &= \frac{\log[e^{-\tau_{0.16} \hat{\tau}_{\text{FUV}}} L_{\lambda, \text{FUV}}^*] - \log[e^{-\tau_{0.16} \hat{\tau}_{\text{NUV}}} L_{\lambda, \text{NUV}}^*]}{\log \lambda_{\text{FUV}} - \log \lambda_{\text{NUV}}} \end{aligned} \quad (14)$$

where we have expressed  $\tau_{\lambda}$  in terms of  $\tau_{0.16}$ , *i.e.*  $\tau_{\lambda} = \hat{\tau}_{\lambda} \times \tau_{0.16}$ , for both FUV and NUV bands. By re-arrangement of this equation, we get

$$\begin{aligned} \beta_{\text{UV}} &= \frac{\log(L_{\lambda, \text{FUV}}^*/L_{\lambda, \text{NUV}}^*) + [\hat{\tau}_{\text{NUV}} - \hat{\tau}_{\text{FUV}}]\tau_{0.16}}{\log(\lambda_{\text{FUV}}/\lambda_{\text{NUV}})} \\ &= \beta_{\text{UV},0} + \mathcal{Z} \tau_{0.16}, \end{aligned} \quad (15)$$

where

$$\beta_{\text{UV},0} = \frac{\log(L_{\lambda, \text{FUV}}^*/L_{\lambda, \text{NUV}}^*)}{\log(\lambda_{\text{FUV}}/\lambda_{\text{NUV}})} \quad \text{and} \quad \mathcal{Z} = \frac{\hat{\tau}_{\text{NUV}} - \hat{\tau}_{\text{FUV}}}{\log(\lambda_{\text{FUV}}/\lambda_{\text{NUV}})} \quad (16)$$

are pure functions of stellar SED and dust attenuation law, respectively.  $\beta_{\text{UV},0}$  is in fact the UV spectra slope of the unattenuated stellar SED. Eq. 15 and Eq. 16 imply that for the dust slab model, the increment (reddening) of the UV spectral slope due to the dust extinction scales *linearly* with  $\tau_{0.16}$  (see *e.g.* Calzetti et al. 2000, for the empirical relation derived using the local starburst sample from Kinney et al. 1993). The slope of the inclination,  $\mathcal{Z}$ , depends on the steepness of the dust attenuation curve in the FUV-to-NUV wavelength range.

By combining Eq. 7 and 15, we can relate IRX and  $\beta_{\text{UV}}$  by a simple formula (*c.f.* Meurer et al. 1999; Hao et al. 2011),

$$\text{IRX} = [e^{(\beta_{\text{UV}} - \beta_{\text{UV},0})/\mathcal{Z}} - 1]\mathcal{Y}, \quad (17)$$

where the three parameters,  $\beta_{\text{UV},0}$ ,  $\mathcal{Z}$ , and  $\mathcal{Y}$ , are functions of  $L_{\lambda}^*$  and  $\tau_{\lambda}$ . For the dust slab model, the IRX- $\beta_{\text{UV}}$  relation therefore has this well-defined analytic solution.

We show in Fig. 7 the analytic solution given by Eq. 17 for

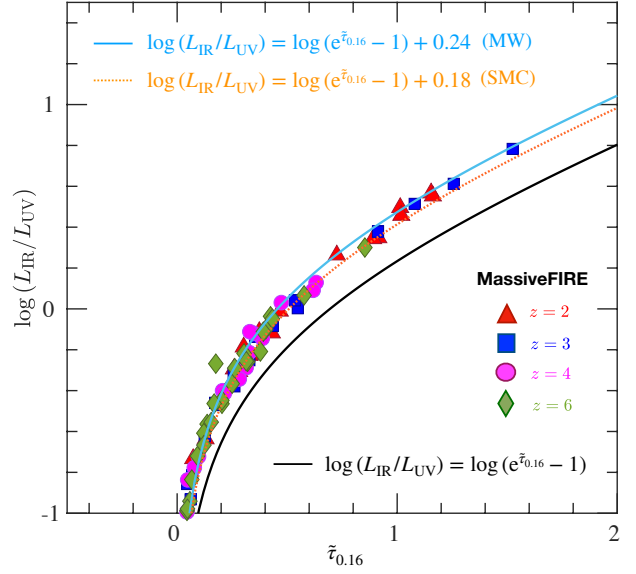


**Figure 8.** Relation between *angle-averaged*  $\tau_{0.16}$  and IRX of the MASSIVEFIRE galaxies. The redshifts of the galaxies are marked with the shape of the symbols as labelled. The data shown are obtained from the fiducial RT model with MW dust. The solid cyan line shows the best-fit exponential-law relation to the data of the fiducial model, while the dotted orange line represents the best-fit relation to the data yielded by using an alternative model where SMC dust is implemented. The solid black line represents the benchmark relation of Eq. 7 with  $\mathcal{Y} = 1$ . The angle-averaged IRX and  $\tau_{0.16}$  of the MASSIVEFIRE galaxies can be well fit by an exponential curve (*i.e.* Eq. 7), with  $\mathcal{Y} = 1.73$  (1.51) for the MW (SMC) dust model. The discrepancy between the best-fit relations (blue and orange lines) and the benchmark relation (black line) is mainly due to the bolometric correction of the UV-to-NIR stellar light relative to the UV emission at 1600 Å (see Eq. 11, *c.f.* Meurer et al. 1999; Calzetti et al. 2000; Hao et al. 2011).

several different stellar SEDs and dust models as in Fig. 6. We can see that by increasing  $t_{\text{age}}$ , the predicted IRX- $\beta_{\text{UV}}$  relation shifts horizontally to higher  $\beta_{\text{UV}}$  without having its shape much affected. In this case,  $\beta_{\text{UV},0}$  in Eq. 17 noticeably increases with  $t_{\text{age}}$ .  $\mathcal{Z}$  is unaffected since it is independent of stellar properties (Eq. 16). In contrast, when the MW dust is replaced with the SMC dust, the expected IRX- $\beta_{\text{UV}}$  relation becomes much shallower in addition to having a horizontal shift to higher  $\beta_{\text{UV}}$ . In this case,  $\mathcal{Z}$  significantly increases (from 0.57 of the MW dust model to 1.01 of the SMC model, calculated using  $\lambda_{\text{FUV}} = 1230 \text{ \AA}$  and  $\lambda_{\text{NUV}} = 3200 \text{ \AA}$  in Eq. 16) whereas  $\beta_{\text{UV},0}$  is unchanged. For both cases,  $\mathcal{Y}$  only mildly changes (with either  $t_{\text{age}}$  or dust model) and thus has only a minor effect on the location and shape of the IRX- $\beta_{\text{UV}}$  relation.

## 4.2 UV Optical depth as driver of the IRX- $\beta$ relation

We have shown that for the dust slab model, the IRX- $\beta_{\text{UV}}$  relation has the simple analytic form of Eq. 17. For a given dust extinction law,  $\tau_{0.16}$  can be viewed as the underlying driver of this relation (see also Popping et al. 2017; Narayanan et al. 2018a). While IRX and  $\tau_{0.16}$  follow an exponential-law relation (Eq. 7),  $\beta_{\text{UV}}$  and  $\tau_{0.16}$  are simply linearly correlated to each other (Eq. 15). Both IRX and  $\beta_{\text{UV}}$  increase with  $\tau_{0.16}$  monotonically.

It is not obvious that these results also apply in real galaxies. As we noted at the beginning of Section 4.1, one key aspect of galaxy that is not captured by the dust slab model is that the dust column density differs for different star-forming regions of a

galaxy. Therefore,  $\tau_\lambda$  should more generally represent the *effective* amount of light lost in aggregate for a number of sightlines between each star and the observer, with a compensation of light scattered back into the sightlines<sup>10</sup>, which can be defined as

$$\tilde{\tau}_\lambda \equiv -\ln\left(\frac{L_\lambda}{L_\lambda^*}\right) = -\ln\left(\frac{\sum_{i=0}^{N_{\text{star}}} L_{i,\lambda} e^{-\tau_{i,\lambda}} + L_{\text{scattered},\lambda}}{\sum_{i=0}^{N_{\text{star}}} L_{i,\lambda}^*}\right), \quad (18)$$

where  $L_\lambda$  and  $L_\lambda^*$  correspond to the attenuated and intrinsic specific luminosity of the galaxy at  $\lambda$ .  $L_{i,\lambda}^*$  and  $\tau_{i,\lambda}$  in the above equation represent the intrinsic specific luminosity and the optical depth of each individual star or star-forming region.  $\tau_{i,\lambda}$  is simply the product of  $\kappa_\lambda$  and the dust column mass density along the sightline, which has the same form as the dust slab model (Eq. 9). Finally,  $L_{\text{scattered},\lambda}$  represents the specific luminosity of light scattered back into the sightlines from dust. Hereafter we use the notation ‘ $\tilde{\tau}_\lambda$ ’ to refer to the *effective* dust optical depth of galaxy, and to distinguish it from the definition using Eq. 9.

We now examine whether  $\tilde{\tau}_{0.16}$ , using the more generalised definition (Eq. 18), follows the same relation with IRX and  $\beta_{\text{UV}}$  of galaxy as those expected from the simple dust slab model (*i.e.* Eq. 7 and Eq. 15).

In Fig. 8, we at first show the relation between  $\tilde{\tau}_{0.16}$  and IRX of the MASSIVEFIRE galaxies at different redshifts ( $z = 2 - 6$ ). The coloured symbols represent the result of our fiducial RT model, where we adopt MW dust and average over 24 random viewing angles. It is clear from the figure that the angle-averaged IRX and  $\tilde{\tau}_{0.16}$  are well correlated, and their relation can be well fit by an exponential curve in the form of Eq. 7, with  $\mathcal{Y}$  being a free parameter. Using least- $\chi^2$  method, we obtain the best-fit relation

$$\log \text{IRX} = \log(e^{\tilde{\tau}_{0.16}} - 1) + (0.24 \pm 0.04). \quad (\text{MW}) \quad (19)$$

We show this relation with solid cyan line in Fig. 8. The relation indicates  $\mathcal{Y} = 1.73 \pm 0.15$ .

The  $\tilde{\tau}_{0.16}$  vs. IRX relation depends (weakly) on the dust attenuation law, as indicated by Eq. 8 and Eq. 10. In Fig. 8, we also show the best-fit exponential-law curve (dotted orange line) to the data yielded by an alternative RT model where we adopt SMC dust instead of MW dust as adopted in our fiducial RT model. We find that the best-fit relation of SMC dust is 0.06 dex below that of MW dust, indicating that a slightly higher  $\tilde{\tau}_{0.16}$  is needed for the same IRX with SMC dust. This is consistent with what is indicated by the analytic solutions for the dust slab model shown in Fig. 6. SMC dust always yields a lower  $\mathcal{Y}$  value than MW dust for the different stellar SEDs. We also note that for clarity of presentation, we do not explicitly show the individual data of SMC dust in Fig. 8, for they overlap much with the data of MW dust.

Let us now examine the  $\tilde{\tau}_{0.16}$  vs.  $\beta_{\text{UV}}$  relation. We show the result of the MASSIVEFIRE galaxies at  $z = 2 - 6$  for MW dust in the *top* panel of Fig. 9. We can see from the *top* panel that  $\tilde{\tau}_{0.16}$  and  $\beta_{\text{UV}}$  are poorly correlated, among either the entire sample or each individual redshift (see also *e.g.* Boquien et al. 2012; Narayanan et al. 2018a). This is in stark contrast with the simple linear correlation expected from Eq. 15. However, the equation includes the term  $\beta_{\text{UV},0}$ . The intrinsic  $\beta_{\text{UV},0}$  may vary between galaxies, due to different star formation histories and hence different age distributions of their stars.

<sup>10</sup> We find that on average  $\sim 7\%$  of  $L_{\text{UV}}$  of the MASSIVEFIRE galaxies is from the light scattered into the camera from dust from our RT calculations.

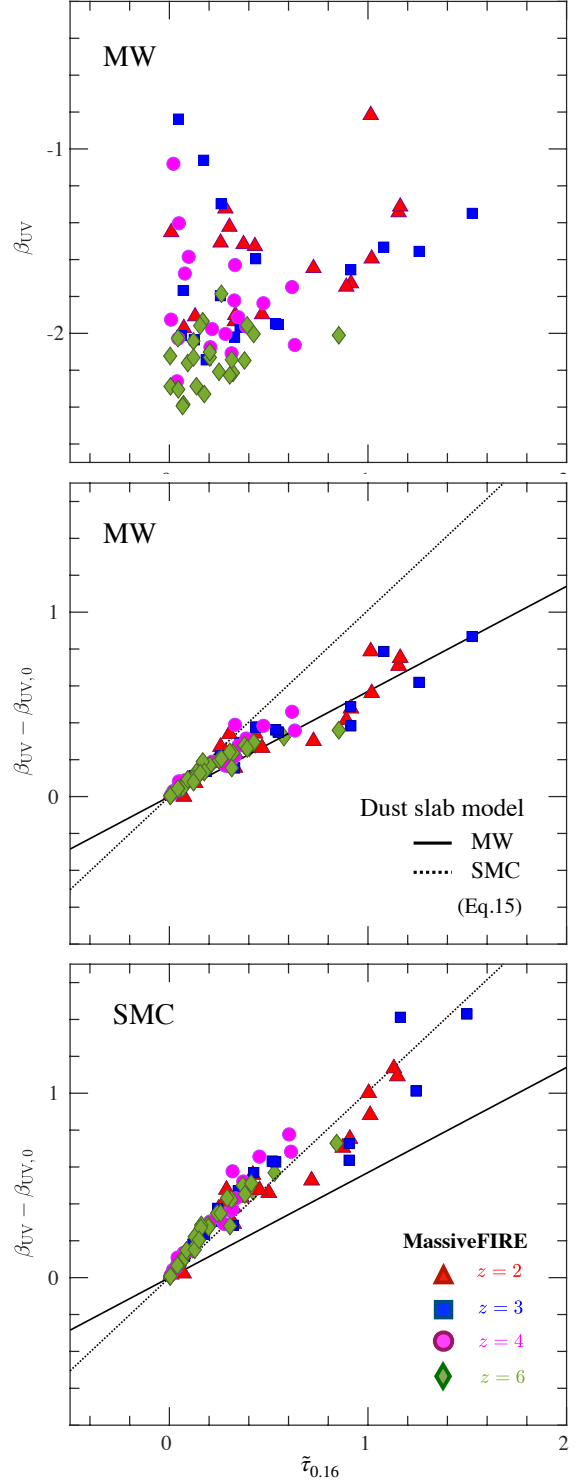


**Figure 9.** The  $\tilde{\tau}_{0.16}$  vs.  $\beta_{\text{UV}}$  relation (*top* panel) and the  $\tilde{\tau}_{0.16}$  vs.  $\beta_{\text{UV}} - \beta_{\text{UV},0}$  relation (*middle* and *bottom* panels) of the MASSIVEFIRE galaxies at different redshifts. The redshifts of the galaxies are indicated by the shape of the symbols as labelled. The *top* panel shows the result for MW dust. The *middle* and *bottom* panels show the results for MW and SMC dust models, respectively. In the *middle* and *bottom* panels, the solid and dotted lines indicate the analytic solution (Eq. 15) of the dust slab model for MW and SMC dust, respectively. The  $\tilde{\tau}_{0.16}$  vs.  $\beta_{\text{UV}} - \beta_{\text{UV},0}$  relations of the MASSIVEFIRE galaxies are in broad agreement with the analytic solutions of the dust slab model, whereas the dispersion of the data in these relations indicate the variation in the shape of the attenuation curve due to the complex dust-to-star geometry of the galaxies.

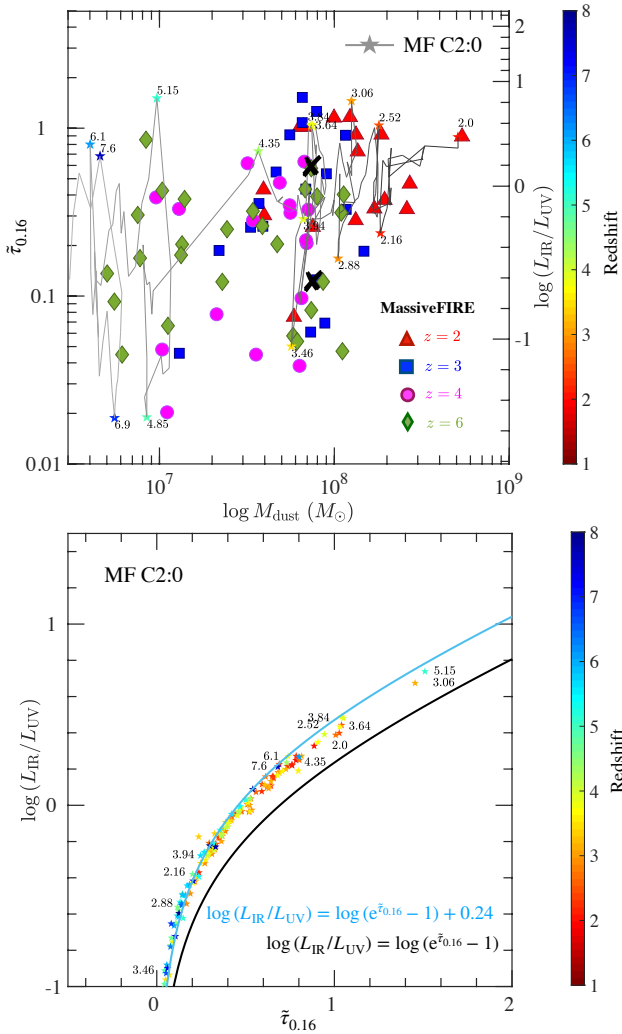


**Figure 10.** *Upper panel:* Relation between  $M_{\text{dust}}$  and angle-averaged  $\bar{\tau}_{0.16}$  (IRX) of the MASSIVEFIRE sample at different redshifts. The redshifts of the galaxies are indicated by the shape of the symbols as labelled. The dark grey line presents the evolutionary trajectory of a selected individual MASSIVEFIRE galaxy (galaxy ID: MF C2:0) on the diagram. A number of instantaneous peaks and troughs in  $\bar{\tau}_{0.16}$  of this galaxy are explicitly marked by asterisks colour-coded by their corresponding redshifts. The two black crosses mark the location of a  $z = 6$  (galaxy ID: MF D3:0) and a  $z = 3$  galaxies (galaxy ID: MF B3:0). The 2D maps of the various properties of the two galaxies are shown in Fig. 12. The y-axis on the right shows the IRX, which maps to  $\bar{\tau}_{0.16}$  by Eq. 19.  $\bar{\tau}_{0.16}$ , which is well correlated with IRX, is not a good proxy of  $M_{\text{dust}}$  of galaxy. *Lower panel:* The angle-averaged  $\bar{\tau}_{0.16}$  vs. IRX relation of the selected galaxy, MF C2:0, at different snapshots. Each data point represents a simulation snapshot and is colour-coded by the corresponding redshift. The cyan and black lines are identical as the ones in Fig. 8.

The remaining two panels of Fig. 9 prove that this explanation is the correct one. In particular, there is a strong correlation between  $\bar{\tau}_{0.16}$  and  $\Delta\beta_{\text{UV}} = \beta_{\text{UV}} - \beta_{\text{UV},0}$ . As expected, the  $\bar{\tau}_{0.16}$  vs.  $\Delta\beta_{\text{UV}}$  relation of the MASSIVEFIRE sample is in broad agreement with the analytic solution derived using the dust slab model, Eq. 15. This is true for both MW (*middle panel*) and SMC dust (*bottom panel*). The slope of inclination of the analytic solution ( $\mathcal{Z}$ ) for MW and SMC dust are 0.57 and 1.01 (calculated by Eq. 16), respectively. The data of MASSIVEFIRE galaxies roughly follow the predicted *linear* relation for both dust models.

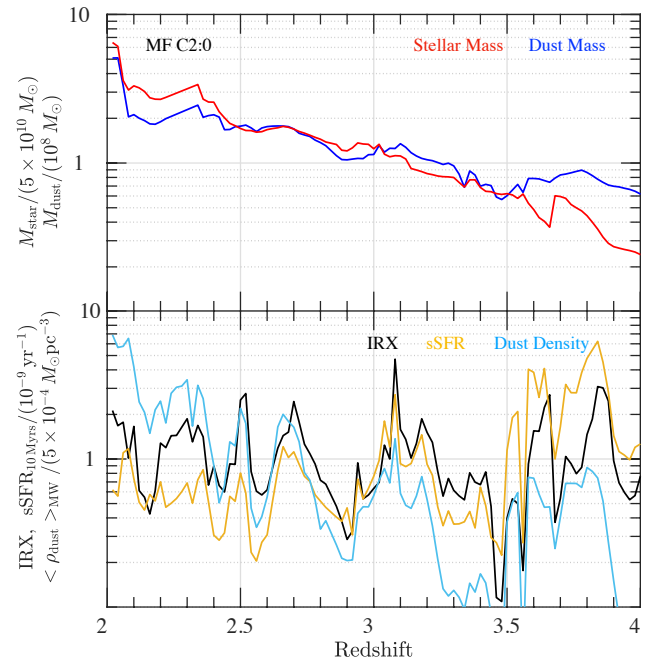


**Figure 11.** *Upper panel:* Evolution of the normalised  $M_*$  (red) and  $M_{\text{dust}}$  (blue) of a selected MASSIVEFIRE galaxy between  $z = 2$  and  $z = 4$ . *Lower panel:* Evolution of IRX (black), as well as the normalised sSFR (brown) and mass-weighted dust density (cyan) over the same time period. IRX is well correlated with sSFR and the dust density while  $M_{\text{dust}}$  slowly grows. This result indicates that IRX (or  $\bar{\tau}_{0.16}$ ) of galaxy depends on the spatial configuration of dust with respect to star-forming regions in galaxy rather than  $M_{\text{dust}}$ .

We notice, however, that the simulation data shows scatter, even though they are produced using a constant extinction curve. The deviation of the galaxies from the analytic solution indicates the variations in the shape of the dust attenuation curve ( $\bar{\tau}_\lambda$ ) of the galaxies from the underlying extinction curve ( $\kappa_\lambda$ ). The shape of  $\bar{\tau}_\lambda$  depends not only on  $\kappa_\lambda$ , but also on the geometry of the dust and star particle distribution in the galaxies (see *e.g.* Witt & Gordon 1996, 2000; Charlot & Fall 2000; Narayanan et al. 2018b).

To summarise this section,  $\bar{\tau}_{0.16}$  is well correlated with IRX and the relation between the two resembles an exponential relation predicted by the dust slab model. In contrast,  $\bar{\tau}_{0.16}$  and  $\beta_{\text{UV}}$  are not well correlated due to the variations in the intrinsic UV spectral slope of the galaxies,  $\beta_{\text{UV},0}$ . The important implication is that  $\beta_{\text{UV}}$  should not be viewed as a reliable proxy for the dust optical depth (or level of dust attenuation) of high- $z$  galaxies (Narayanan et al. 2018a). Instead,  $\Delta\beta_{\text{UV}} = \beta_{\text{UV}} - \beta_{\text{UV},0}$  is linearly correlated with  $\bar{\tau}_{0.16}$ .

### 4.3 The nature of infrared excess of galaxies

We have shown in the last subsection that the IRX of galaxies are well correlated with  $\bar{\tau}_{0.16}$ . It is therefore important to understand what determines  $\bar{\tau}_{0.16}$  of galaxies at different stages of their evolution.

The total *effective* optical depth of galaxies may depend on the total dust mass and/or the spatial configuration of dust distribution.

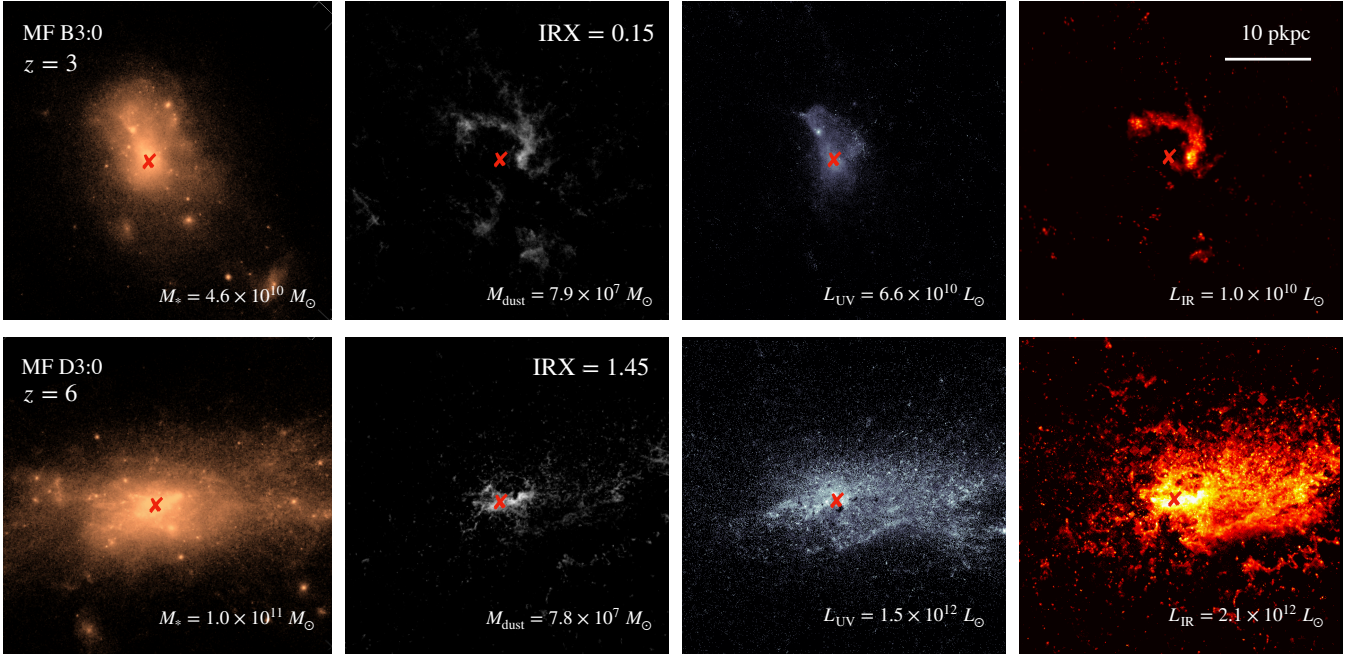


**Figure 12.** 2D maps of stellar mass (*left*), dust mass (*middle left*), UV (*middle right*) and IR surface brightness (*right*) of two MASSIVEFIRE galaxies at  $z = 3$  (*upper panels*) and  $z = 6$  (*lower panels*). The two galaxies have similar  $M_{\text{dust}}$  ( $\approx 10^8 M_{\odot}$ ) but very different IRX (0.15 vs. 1.45). The red crosses in the *upper* and *lower* panels mark the location of the maximum surface density of stellar mass of the two galaxies. These also correspond to the local maximum points of the UV surface brightness (*right middle panels*). IRX strongly depends on the dust-to-star geometry in galaxies.

We first examine the relation between  $\tilde{\tau}_{0.16}$  and  $M_{\text{dust}}$ <sup>11</sup> in MASSIVEFIRE. The *upper* panel of Fig. 10 shows that  $\tilde{\tau}_{0.16}$  and  $M_{\text{dust}}$  are weakly correlated. We also overplot in the panel the trajectory of a selected galaxy (galaxy ID: MF C2:0) between  $z = 8$  and  $z = 2$  with a dark grey line. This galaxy goes through several periods of significant rise and decline in  $\tilde{\tau}_{0.16}$ , while its dust mass slowly increases. On the other hand,  $\tilde{\tau}_{0.16}$  is always well correlated with IRX (both are angle-averaged) and their relation does not deviate much from the best-fit exponential-law curve that we have derived using the entire sample, as shown in the *lower* panel of the figure. This is because the  $\mathcal{Y}$  parameter in Eq. 7 has limited variation as the galaxy evolves with time.

The evolution of the galaxy’s  $\tilde{\tau}_{0.16}$  (or equivalently, IRX) is well correlated to dust mass density, as is shown in Fig. 11 (*lower panel*). This signifies that  $\tilde{\tau}_{0.16}$  of galaxies is driven by the compactness of the spatial configuration of dust rather than the total amount of dust. Interestingly, the evolution of both IRX (black line) and dust mass density (cyan line) also coincide with that of sSFR (golden line), since more star formation is triggered when the ISM gas/dust becomes more compact and thus the local free-fall timescale of star-forming clouds decreases ( $t_{\text{ff}} \propto \rho^{-1/2}$ ). IRX (or  $\tilde{\tau}_{0.16}$ ), sSFR, and dust mass density can significantly vary on relatively short timescales ( $\lesssim 100$  Myrs), while the dust and stellar masses of galaxy gradually grow.

Therefore, the observationally derived IRX of a galaxy mainly reflects the spatial configuration of dust with respect to star-forming regions, and provides limited constraint on its dust mass. To better illustrate this, we present the 2D maps of the dust mass column density of two MASSIVEFIRE galaxies at two different redshifts ( $z = 3$  and  $z = 6$ ) in Fig. 12. These two galaxies have about the same  $M_{\text{dust}}$

( $\approx 10^8 M_{\odot}$ ) but significantly different IRX (0.15 vs. 1.45). The location of the two galaxies on the  $M_{\text{dust}}$  vs.  $\tilde{\tau}_{0.16}$  diagram are marked with black crosses in Fig. 10 (*upper panel*). The  $z = 6$  galaxy (galaxy ID: MF D3:0) is at an instantaneous peak of star formation, having a  $\text{SFR}_{10 \text{ Myrs}} = 250 M_{\odot} \text{ yr}^{-1}$ . The  $z = 3$  galaxy (galaxy ID: MF B3:0) is relatively quiescent and has a much lower  $\text{SFR}_{10 \text{ Myrs}}$  of only  $7 M_{\odot} \text{ yr}^{-1}$ . Comparing the *upper* and *lower* panels (*middle left*), it is clear that the  $z = 6$  object shows a more compact spatial configuration of dust distribution near the star-forming regions at the galaxy center (marked by red cross in each panel), where most of its UV and IR emission originates. The dust in the  $z = 3$  galaxy, on the contrary, is dispersed away from the UV-emitting regions. The relatively high IRX of the  $z = 6$  galaxy is due to the higher obscuration of its star-forming regions.

We now investigate the relationship between  $\tilde{\tau}_{0.16}$  (equivalently, IRX) and several important observable properties of galaxies, including starburstiness<sup>12</sup>,  $M_*$ ,  $L_{\text{UV}}$  and  $L_{\text{IR}}$ , see Fig. 13. In each panel, we show the results for both the  $z = 2$ – $6$  galaxy sample and the evolutionary trajectory of a selected MASSIVEFIRE galaxy.

The figure shows that  $\tilde{\tau}_{0.16}$  (equivalently, IRX) has a moderate correlation with starburstiness (Spearman’s correlation coefficient  $r_s = 0.57$ ), which is not surprising because the increase in ISM density results in a higher SFR.  $\tilde{\tau}_{0.16}$  also correlates with  $L_{\text{IR}}$  ( $r_s = 0.55$ ) because galaxies of higher  $\tilde{\tau}_{0.16}$  tend to be more bursty and thus dust is exposed to a harder radiation field resulting from the enhanced fraction of young stars (see also *e.g.*, Wang & Heckman 1996; Adelberger & Steidel 2000; Bell 2003; Buat et al. 2005; Jonsson et al. 2006; Buat et al. 2007, 2009; Reddy et al. 2010; Hayward et al. 2012). In addition, a higher fraction of stellar light is absorbed and reemitted due to higher  $\tilde{\tau}_{0.16}$ .  $L_{\text{UV}}$ , on the contrary,

<sup>11</sup> Physical properties of galaxies (*i.e.*  $M_{\text{dust}}$ ,  $M_*$ , SFR,  $L_{\text{UV}}$ ,  $L_{\text{IR}}$  and etc.) reported in this paper are estimated using a radial kernel of 30 physical kpc around the dark matter halo center.

<sup>12</sup> We defined ‘starburstiness’ as the ratio of a galaxy’s sSFR to the median sSFR of the sample at that redshift, *i.e.*  $\text{sSFR}/\text{sSFR}(z)$ .

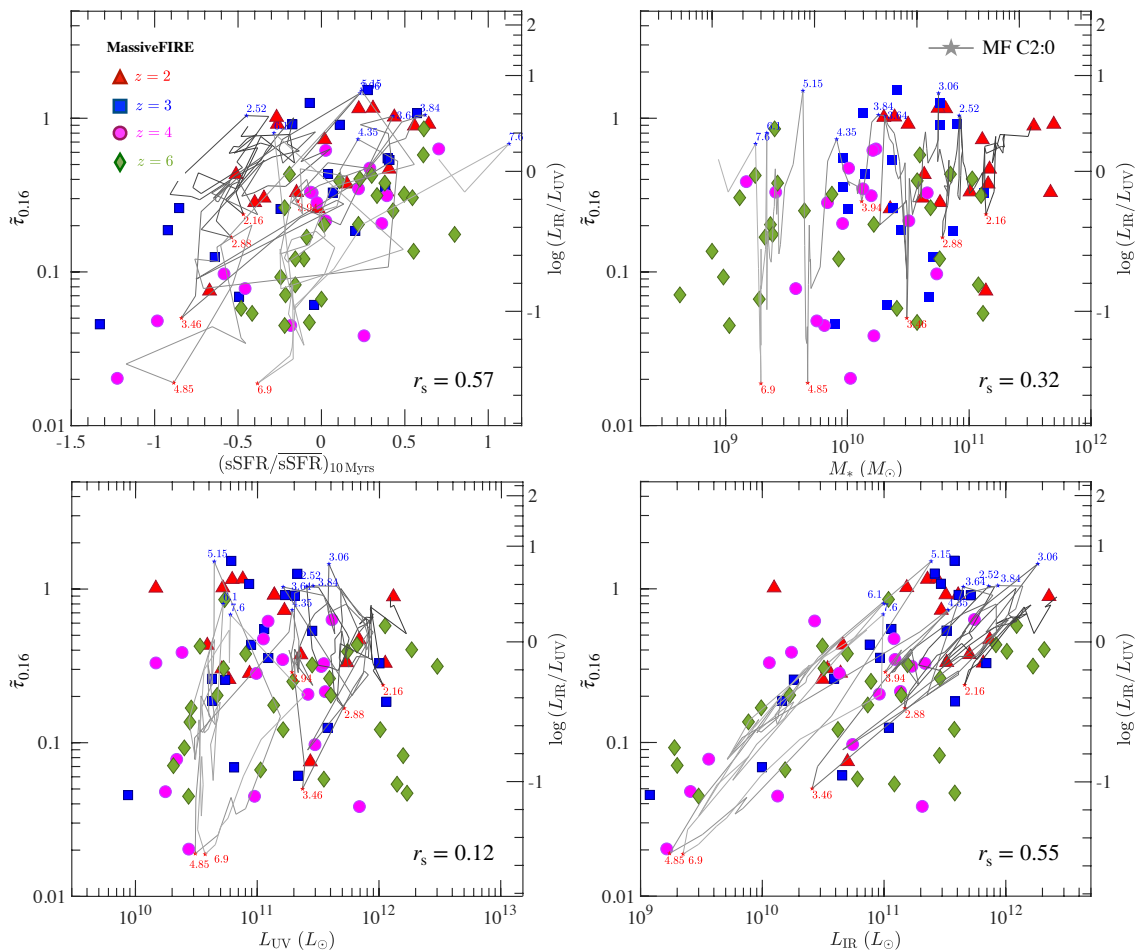


**Figure 13.** The  $\tilde{\tau}_{0.16}$  vs. starburstiness (*upper left*),  $\tilde{\tau}_{0.16}$  vs.  $M_*$  (*upper right*),  $\tilde{\tau}_{0.16}$  vs.  $L_{UV}$  (*lower left*) and  $\tilde{\tau}_{0.16}$  vs.  $L_{IR}$  (*lower right*) relations of the MASSIVEFIRE galaxies at  $z = 2 - 6$ . The redshifts of the galaxies are indicated by the shape of the symbols as labelled. The dark grey line in each panel represents the evolutionary trajectory of a selected MASSIVEFIRE galaxy from  $z = 8$  to  $z = 2$ . A number peaks and troughs in  $\tilde{\tau}_{0.16}$  (IRX) are marked with blue and red asterisk in each panel.  $\tilde{\tau}_{0.16}$  shows a moderate correlation with starburstiness (Spearman’s correlation coefficient  $r_s=0.57$ ) and  $L_{IR}$  ( $r_s=0.55$ ) of galaxies, and a weak correlation with  $M_*$  ( $r_s=0.32$ ) and  $L_{UV}$  ( $r_s=0.12$ ).

shows almost no correlation with  $\tilde{\tau}_{0.16}$  ( $r_s = 0.12$ ) due to increasing absorption with  $\tilde{\tau}_{0.16}$  (see also *e.g.*, Buat et al. 2009; Reddy et al. 2010; Casey et al. 2014b; Sklias et al. 2014; Reddy et al. 2018). And finally,  $\tilde{\tau}_{0.16}$  and  $M_*$  are only weakly correlated ( $r_s = 0.32$ ). This is consistent with the scenario that the spatial redistribution of dust and the interstellar radiation field can significantly change on the timescale of a few 10 Myrs, while galaxies assemble their dust and stellar masses on much longer timescales (see Fig. 11, *c.f.*, Sklias et al. 2014; Bouwens et al. 2016; Fudamoto et al. 2017; Reddy et al. 2018; Koprowski et al. 2018; McLure et al. 2018; Fudamoto et al. 2020; Bouwens et al. 2020).

#### 4.4 The evolution of galaxies in the IRX- $\beta_{UV}$ plane

Using the dust slab model, we have shown that while dust UV optical depth drives galaxies along the direction of the IRX- $\beta_{UV}$  relation, variation of stellar age contributes to the offsets from the relation. Optical depth and stellar age thus act as two independent factors that affect the location of galaxies in the IRX- $\beta_{UV}$  plane in the case of the toy model. For real galaxies, however, the two quantities may be correlated. For instance, Fig. 11 shows that during a starburst,  $\tilde{\tau}_{0.16}$  (equivalent to IRX) increases while more young stars are born. The anti-correlation between  $\tilde{\tau}_{0.16}$  and stellar population

ages has consequence for the evolutionary trajectory of galaxies in the IRX- $\beta_{UV}$  plane.

In Fig. 14, we show the location of a selected MASSIVEFIRE galaxy (galaxy ID: MF A3:0) in the IRX- $\beta_{UV}$  plane at different snapshots at  $z = 2 - 6$ . While we show only one example, the overall behaviour of this galaxy is typical for the galaxies in our sample.

The evolutionary trajectory of this galaxy over the period of  $z = 3 - 3.75$  is highlighted by the magenta line. We mark five characteristic times that distinguish the different evolutionary stages using capital letters (from ‘A’ to ‘E’). Fig. 15 shows the evolution of IRX and  $\beta_{UV}$  of the galaxy as a function of lookback time, together with other galaxy properties that are relevant for the physical explanation of the galaxy’s trajectory in the IRX- $\beta_{UV}$  plane.

According to Fig. 14, the trajectory of the galaxy in the IRX- $\beta_{UV}$  plane is counter-clockwise. Time ‘A’ corresponds to  $z = 3.62$ , when a minor merger occurs. Over the next 70 Myrs, the gas/dust distribution of the galaxy becomes more concentrated due to the instabilities induced by the merger and the star-forming regions become more obscured, resulting in a significant boost of  $\tilde{\tau}_{0.16}$  and hence IRX of the galaxy, until time ‘B’ ( $z = 3.52$ ). Meanwhile, the sSFR of galaxy is also enhanced due to the growing compactness of the gas distribution (*top panel* of Fig. 15). Furthermore, the galaxy’s



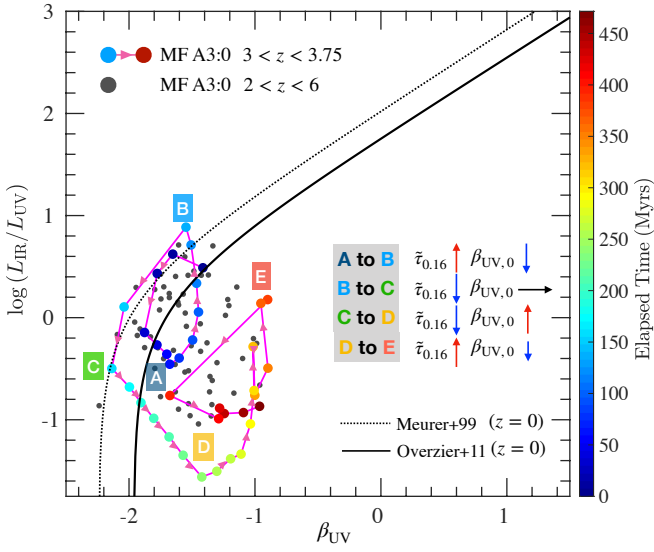


**Figure 14.** Evolution of selected MASSIVEFIRE galaxy in the IRX- $\beta_{\text{UV}}$  plane. The magenta curve shows the evolutionary trajectory of this galaxy between  $z = 3.75$  and  $z = 3$ . The filled dots linked by the curve represent the output snapshots of the simulation, which are colour-coded by the time that has elapsed since  $z = 3.75$  (in unit of Myrs). The grey dots indicate the location of the galaxy at the other snapshots between  $z = 2 - 6$ . We specifically mark the five characteristic snapshots (A, B, C, D and E) on the galaxy’s trajectory to distinguish the different evolutionary stages of the galaxy (Section 4.4). The dotted and solid black lines indicate the local M99 and M99<sub>corr</sub> relations, respectively. The location of galaxy in the IRX- $\beta_{\text{UV}}$  plane exhibits a large spread over cosmic time and its evolutionary trajectory shows counter-clockwise rotation.

UV-luminosity-weighted age,  $t_{\text{age,UV}}$ , computed by weighting the age of each star particle by its luminosity over  $\lambda = 0 - 3200 \text{ \AA}$ , decreases from  $\sim 0.5$  Gyr at time ‘A’ to  $\sim 0.1$  Gyr at time ‘B’. This is because more young, massive OB stars are formed over this period, which dominates the rest-UV emission of the galaxy. Consequently,  $\beta_{\text{UV},0}$  declines from -1.8 to -2.4.  $\beta_{\text{UV}}$ , on the contrary, is nearly constant because the increased reddening due to the larger  $\tilde{\tau}_{0.16}$  cancels out the decrease in  $\beta_{\text{UV},0}$  (see Eq. 15).

From ‘B’ to ‘C’, the galaxy moves roughly along the M99 relation downwards in the IRX- $\beta_{\text{UV}}$  plane (Fig. 14). The IRX of the galaxy decreases to nearly the same value as at time ‘A’. This happens on a much shorter timescale,  $\sim 20$  Myrs (see Fig. 15). Over this period of time, feedback from the newly born stars efficiently ejects the material in the star-forming region, which leads to a decrease in  $\tilde{\tau}_{0.16}$  of the galaxy.  $\beta_{\text{UV},0}$ , however, does not change significantly on this short timescale (lower middle panel, Fig. 15). Therefore,  $\beta_{\text{UV}}$  of the galaxy becomes bluer because of the reduced reddening due to the decrease of  $\tilde{\tau}_{0.16}$ .

From ‘C’ to ‘D’, the galaxy undergoes a quenching phase that lasts about 100 Myrs (see Feldmann et al. 2017 for an in-depth discussion of quenching in MASSIVEFIRE galaxies). Over this period, stellar feedback continues to eject the dust near star-forming regions and reduce the optical depth of the galaxy. As the OB stars die out,  $t_{\text{age,UV}}$  increases to  $\sim 1$  Gyr, which is similar to the mass-weighted stellar age (upper middle panel, Fig. 15). The galaxy’s sSFR continuously declines, reaching a minimum value of  $7 \times 10^{-11} M_{\odot} \text{ yr}^{-1}$  at Snapshot ‘D’ (top panel). Due to the aging of the stellar population,  $\beta_{\text{UV},0}$  significantly increases from -2.3 to -1.2, driving the increase of  $\beta_{\text{UV}}$  (lower middle panel). Over this

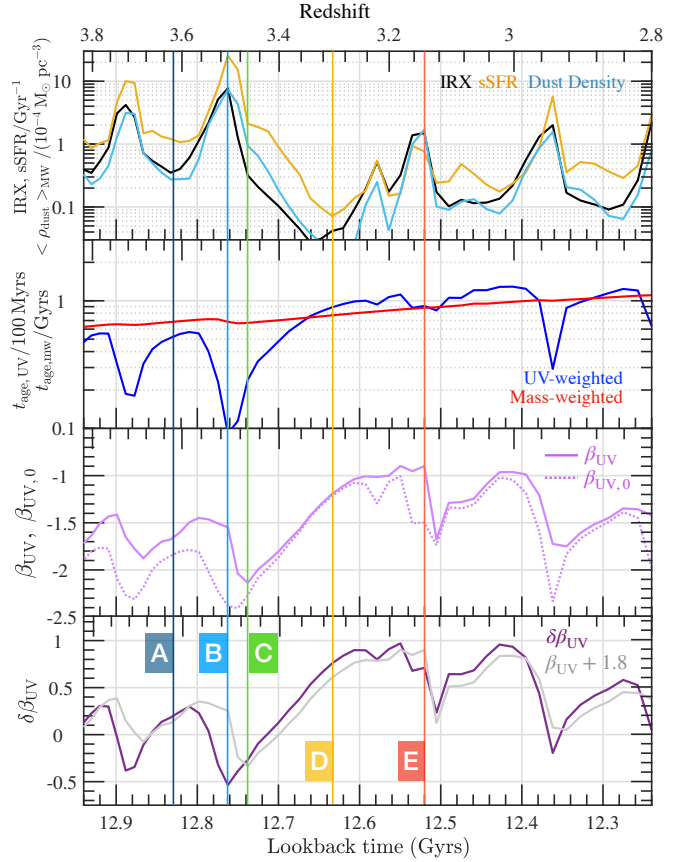


**Figure 15.** Evolution of different properties of a typical MASSIVEFIRE galaxy (same as shown in Fig. 14) from  $z = 3.8$  to  $z = 2.8$ . *Top panel:* Evolution of the IRX (black line), the normalised sSFR (yellow line), and mass-weighted dust density (cyan line). *Upper middle panel:* Evolution of the UV-luminosity-weighted (blue line) and the mass-weighted (red line) stellar age of the galaxy. *Lower middle panel:* Evolution of  $\beta_{\text{UV}}$  (solid violet line) and  $\beta_{\text{UV},0}$  (dotted violet line). *Bottom panel:* Evolution of  $\delta\beta_{\text{UV}}$  (purple line), the horizontal offset of the galaxy’s location from the canonical M99 relation. The grey line in this panel represents the rescaled UV spectral slope,  $\beta_{\text{UV}}+1.8$ . The vertical dark blue, blue, green, yellow and red lines mark the five characteristic snapshots that distinguish the different evolutionary stages of the galaxy, as in Fig. 14.

period, the galaxy’s  $\beta_{\text{UV}}$  becomes redder mainly because of the aging of the stellar population instead of the optical depth effect.

At Snapshot ‘D’, the galaxy restarts gas accretion which triggers active star formation within the galaxy again. Over a period of  $\sim 120$  Myrs, its gas and dust density, UV optical depth and IRX increases until time ‘E’ (top panel, Fig. 15). However, the gas accretion over this period is not as violent as the period of ‘A’ to ‘B’, and so the galaxy remains below the M99 relation since the young OB stars do not outshine the more evolved stars at rest-frame UV wavelength.

The galaxy undergoes such starburst-dispersal-quenching-reaccretion cycles throughout its lifetime (Muratov et al. 2015; Anglés-Alcázar et al. 2017; Feldmann et al. 2017; Sparre et al. 2017). As a result, the trajectory of galaxy in the IRX- $\beta_{\text{UV}}$  plane shows repeated counter-clockwise rotation. The location and the size of these cycles certainly depend on the strength of the starburst and the quenching of each cycle. Overall, the location of an individual galaxy on the diagram shows significant dispersion over

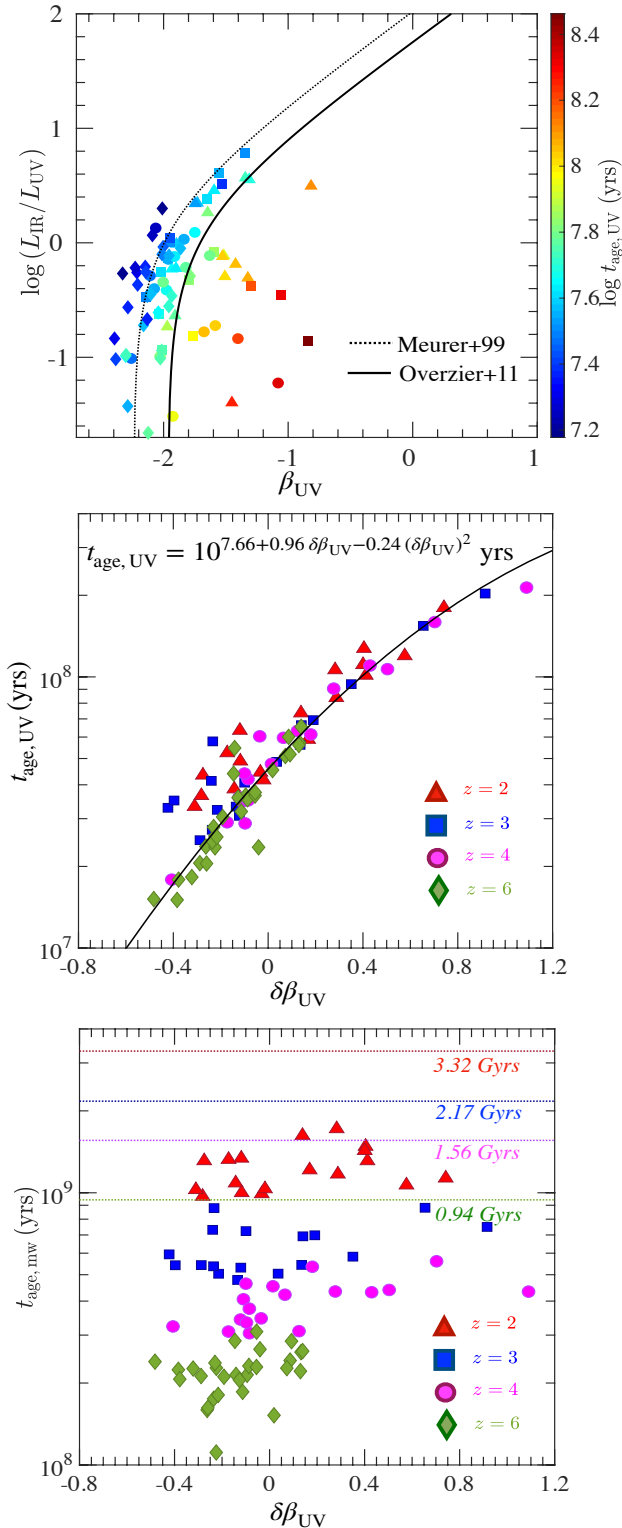


**Figure 16.** *Top panel:* The ‘secondary dependence’ of the IRX- $\beta_{\text{UV}}$  relation on the UV-luminosity-weighted stellar age,  $t_{\text{age,UV}}$ . The dotted and solid black lines indicate the local M99 and M99<sub>corr</sub> relations, respectively. *Middle panel:* The relation between  $t_{\text{age,UV}}$  and  $\delta\beta_{\text{UV}}$  in MASSIVEFIRE. *Bottom panel:* The relation between the mass-weighted stellar age,  $t_{\text{age,mw}}$ , and  $\delta\beta_{\text{UV}}$ . The dotted red, blue, magenta and green horizontal lines mark the age of the Universe at  $z = 2$ ,  $z = 3$ ,  $z = 4$  and  $z = 6$ , respectively. While  $\delta\beta_{\text{UV}}$  is strongly correlated with  $t_{\text{age,UV}}$ ,  $\delta\beta_{\text{MW}}$  and  $t_{\text{age,mw}}$  have no clear correlation.

cosmic time, as indicated by the coloured and grey dots in Fig. 14. The IRX of MF A3:0 varies by more than two orders of magnitude and its  $\beta_{\text{UV}}$  by order unity at  $z = 2 - 6$ .

From Fig. 15, we can see that  $\delta\beta_{\text{UV}}$  (*bottom panel*), the horizontal offset of the galaxy’s  $\beta_{\text{UV}}$  from the M99 relation, well correlates to  $t_{\text{age,UV}}$  (*upper middle panel*). We therefore expect a good correlation between the two quantities of the general galaxy sample. This is indeed the case. We can see from Fig. 16 that the ‘secondary dependence’ of the IRX- $\beta_{\text{UV}}$  relation on  $t_{\text{age,UV}}$  appears to be remarkable. And by fitting  $\delta\beta_{\text{UV}}$  vs.  $\log(t_{\text{age,UV}})$  of the sample by a second-order polynomial law, we obtain

$$\log\left(\frac{t_{\text{age,UV}}}{10^8 \text{ yrs}}\right) = (7.66 \pm 0.02) + (0.96 \pm 0.15)\delta\beta_{\text{UV}} - (0.24 \pm 0.48)(\delta\beta_{\text{UV}})^2. \quad (20)$$

We note that  $t_{\text{age,mw}}$  shows no clear correlation with  $\delta\beta_{\text{UV}}$  (*lower panel*, Fig. 16). This reflects that the shape of galaxies’ SEDs at rest-frame UV is determined by the galaxies’ recent star formation activities, and is not well correlated with the formation history of the more evolved bulk of the stellar population.

#### 4.5 Additional sources of scatter in the IRX- $\beta$ relation

We will examine in this section a few additional sources of the scatter in the IRX- $\beta_{\text{UV}}$  relation, including the changes of dust extinction law, dust-to-metal mass ratio, direction of viewing and also the stellar population model (singular vs. binary evolution of stars).

##### 4.5.1 The variation of the dust extinction law

The dust extinction law of galaxies at high- $z$  is not well constrained and is one important source of uncertainty in the IRX- $\beta_{\text{UV}}$  relation. In this work, we adopt the MW and SMC dust models of WD01. The extinction curve of the SMC dust model has a steeper slope at UV than that of the MW model and has no clear ‘bump’ feature at  $\lambda = 2175 \text{ \AA}$  (Fig. 2), which is present in the MW curve. Since high- $z$  galaxies are more metal-poor than nearby galaxies of the same mass (*e.g.*, Tremonti et al. 2004), SMC dust is often invoked by the studies of high- $z$  galaxies.

We produce the IRX- $\beta_{\text{UV}}$  relation using the SMC dust in addition to the MW dust (which is employed in the fiducial model), and show the results of both cases in Fig. 17 (*left panel*). As discussed before (Section 4.2), the two dust models lead to very similar IRX. The SMC dust generates an IRX that is lower, on the average, by only about 0.06 dex (see Fig. 8). In contrast, it can lead to a significant offset of  $\beta_{\text{UV}}$ , and the offset becomes more prominent with increasing  $\tilde{\tau}_{0.16}$  and IRX. This is clearly shown in *right panel* of Fig. 17, where we plot the difference between the  $\beta_{\text{UV}}$  obtained from the two dust models as a function of  $\tilde{\tau}_{0.16}$ . The relation is in good agreement with the prediction from the dust slab model, which we show by the solid black line in the *right panel*.

To derive this analytic relation of the toy model, we first rewrite the Eq. 15 for the two dust models as

$$\beta_{\text{MW}} = \beta_0 + \mathcal{Z}_{\text{MW}} \tilde{\tau}_{0.16} \quad \text{and} \quad \beta_{\text{SMC}} = \beta_0 + \mathcal{Z}_{\text{SMC}} \tilde{\tau}_{0.16}. \quad (21)$$

Then by subtracting one equation by the other, we obtain

$$\beta_{\text{SMC}} - \beta_{\text{MW}} = (\mathcal{Z}_{\text{SMC}} - \mathcal{Z}_{\text{MW}}) \tilde{\tau}_{0.16} = 0.48 \tilde{\tau}_{0.16}, \quad (22)$$

where we have input  $\mathcal{Z}_{\text{SMC}} = 1.01$  and  $\mathcal{Z}_{\text{MW}} = 0.57$ , calculated

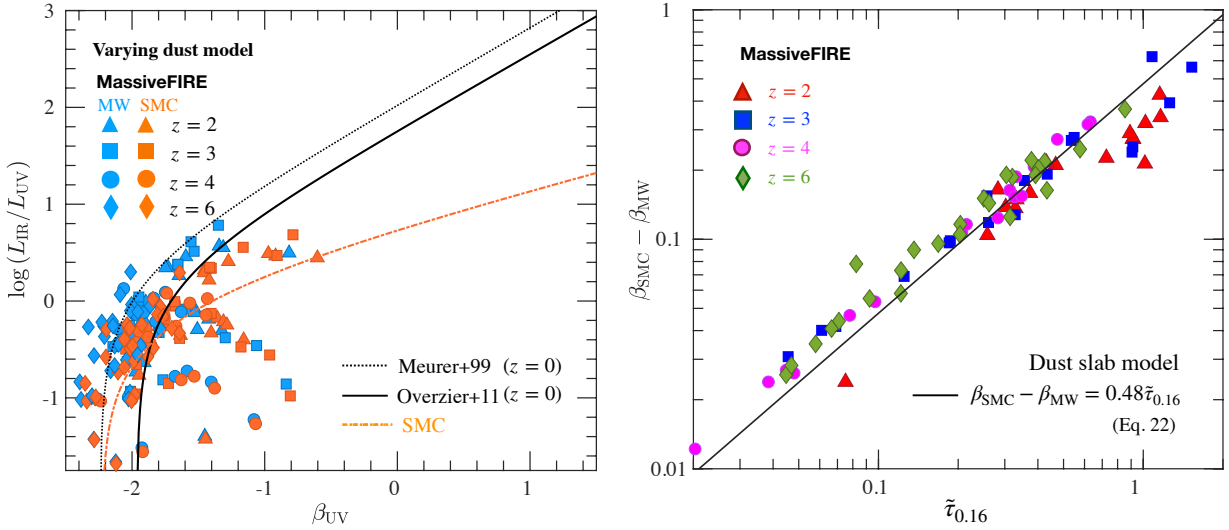


**Figure 17.** *Left panel:* IRX vs.  $\beta_{UV}$  relation of the MASSIVEFIRE galaxies for the two dust models, MW (blue symbols) and SMC (orange symbols) of WD01. The dotted and solid black lines show the M99 and M99<sub>corr</sub> relations. The dot-dashed orange line shows the result of the dust slab model for SMC dust, with  $t_{\text{age}} = 50$  Myrs and  $Z_{*} = 0.1Z_{\odot}$ . *Right panel:* The difference between the  $\beta_{UV}$  produced by MW and SMC dust as a function of  $\tilde{\tau}_{0.16}$ . The solid black line represents the analytic result derived from the dust slab model (Eq. 22).

using  $\lambda_{FUV} = 1230 \text{ \AA}$  and  $\lambda_{NUV} = 3200 \text{ \AA}$  in Eq. 16. The equation shows that the difference in the  $\beta_{UV}$  of galaxies produced by the two extinction curves is expected to be *linearly* scaled to  $\tilde{\tau}_{0.16}$ .

Note that this result is not limited to the two particular dust models that we use. Any variation in the steepness of the dust extinction curve at UV will result in a linear relation between the offset of  $\beta_{UV}$  and  $\tilde{\tau}_{0.16}$ . The slope of the linear relation is determined by the difference in the steepness of the two extinction curves being considered.

#### 4.5.2 The dependence on viewing angle

The dust attenuation curve of galaxies may depend on various directions due to a non-isotropic distribution of dust and stars. Consequently, viewing direction can be one source of scatter for the IRX- $\beta_{UV}$  relation.

We examine how the  $\tilde{\tau}_{0.16}$  vs. IRX relation depends on viewing direction in Fig. 18. There we show IRX and  $\tilde{\tau}_{0.16}$  at  $z = 2$  for the galaxies of our sample at 24 random viewing angles. The data points corresponding to the different viewing angles exhibit more significant scatter compared with the angle-averaged result (Fig. 8). The angle-averaged relation is well fit by Eq. 7. Interestingly, viewing the same galaxy from different viewing angles leads to a shallower IRX- $\tilde{\tau}_{0.16}$  relation than Eq. 7, indicating a smaller  $\mathcal{Y}$  at higher  $\tilde{\tau}_{0.16}$ . This result signifies the variation of the dust attenuation curve with viewing direction (Eq. 10).

In Fig. 19, we explicitly show the attenuation curve of each of the 24 viewing angles of a selected disc-like galaxy (galaxy ID: MF A2:0) at  $z = 2$  (see Fig. 1 for its visualisation).  $\tilde{\tau}_{0.16}$  of the galaxy spans over the range of 0.81–1.73 amongst the viewing angles (Fig. 18), with the median value being 1.15. The figure clearly shows that the galaxy’s edge-on (face-on) direction has roughly the highest (lowest)  $\tilde{\tau}_{0.16}$  among all the sightlines. In Fig. 20, we show the cumulative probability distribution of dust column mass density (in units of  $M_{\odot} \text{ pc}^{-2}$ ) of the star particles in both the face-on (left panel) and edge-on (right panel) directions. The mean column mass density in the face-on and edge-on directions are  $2.4 \times 10^{-2}$

and  $7.6 \times 10^{-2} M_{\odot} \text{ pc}^{-2}$ , respectively. The latter is higher by a factor of  $\sim 3$ , thus explaining the larger  $\tilde{\tau}_{0.16}$  for the edge-on viewing direction.

There is also a clear trend that the attenuation curve becomes shallower (or ‘grayer’) with increasing  $\tilde{\tau}_{0.16}$  (right panel of Fig. 19). The flattening of the attenuation curve leads to the decrease of  $\mathcal{Y}$  with increasing  $\tilde{\tau}_{0.16}$  (Eq. 10). This trend is driven by the variation of dust column density with stellar age — younger stars reside in the more opaque regions where dust column density is higher.

To better illustrate this, we separately show in Fig. 20 the column density distribution of the young stars ( $t_{\text{age}} < 10$  Myrs) and the evolved stars ( $t_{\text{age}} \geq 10$  Myrs) at the two viewing angles. The mean column density of the young stars in the face-on on edge-on directions are  $4.7 \times 10^{-2}$  and  $0.47 M_{\odot} \text{ pc}^{-1}$ , which are higher than that of the evolved stars by 0.3 and 0.8 dex (a factor of 1.9 and 6.3), respectively.

The young stars dominate the emission at FUV and the attenuation of galaxy at FUV strongly depends on the obscuration of the young stars. We separately show the emission of the young and evolved stars of MF A2:0 in the left panel of Fig. 19 (black dashed lines). The young stars, which account for only 0.4% of the total stellar mass of this galaxy, dominate the stellar emission of the galaxy at  $\lambda \leq 2500 \text{ \AA}$ , while the emission at longer wavelength is dominated by the evolved stars. A large fraction of these young stars are ‘highly obscured’ at FUV (*i.e.*,  $\tau_{FUV} \gtrsim 1$ ). Specifically, 40% (90%) of the young stars have  $\tau_{0.12}$  (measured at  $\lambda_{FUV} = 1230 \text{ \AA}$ ) over unity in the face-on (edge-on) direction. The consequence of the high obscuration of the young stars is that the attenuation at FUV ‘responds’ mildly to a change in the dust column density, as it turns from the face-on to the edge-on direction (the decline in  $e^{-\tau}$  ‘saturates’ when  $\tau \gtrsim 1$ ).

In contrast, the attenuation at NUV is more sensitive to a change in viewing direction because the evolved stars, which dominate the NUV emission because the evolved stars, which dominate the NUV emission, reside in the relatively diffuse environments. 76% (51%) of the evolved stars have  $\tau_{0.32}$  (measured at  $\lambda_{NUV} = 3200 \text{ \AA}$ ) less than unity in the face-on (edge-on) direction.

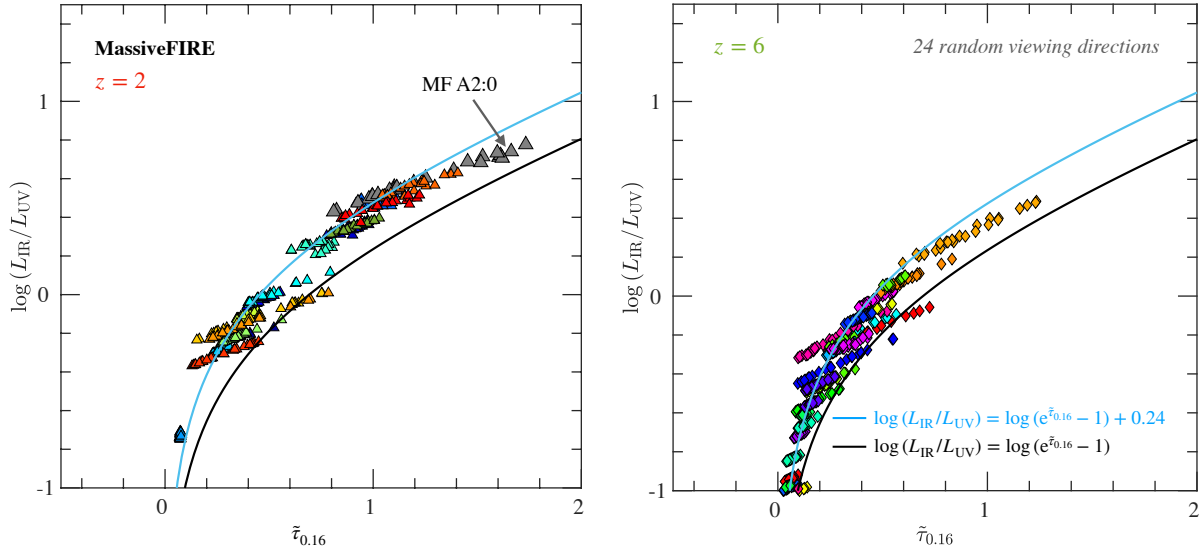


**Figure 18.**  $\tilde{\tau}_{0.16}$  vs. IRX relation of MASSIVEFIRE galaxies at 24 different viewing angles. We show the results for the  $z = 2$  and  $z = 6$  galaxies in the *left* and *right* panels, respectively. All viewing directions of the same galaxy are marked by the same colour. The cyan and black solid lines are the same reference relations as in Fig. 8. The  $\tilde{\tau}_{0.16}$  vs. IRX relation of each individual galaxy at different viewing angles is shallower than the exponential relation that best fit the angle-averaged result of the whole sample (Eq. 19). This indicates that the dust attenuation law of galaxies depends on viewing direction.

As a result, the attenuation at NUV, increases more significantly with dust column density ( $e^{-\tau}$  declines rapidly with increasing  $\tau$  at  $\tau < 1$ ).

Scattering plays a role in altering the shape of the attenuation curve, in particular, in the regime redwards of the ‘bump’ ( $\lambda > 2175 \text{ \AA}$ ) (*right* panel of Fig. 19). The attenuation curve becomes steeper by accounting for the light scattered into the camera from dust because this component compensates more for the loss of light by extinction along the sightlines at longer wavelength in the UV-to-optical regime. Furthermore, the scattered light accounts for a larger fraction of the total received light in the face-on direction due to the anisotropy of scattering (*left* panel). The discrepancy in the steepness of the attenuation curve between the viewing angles is magnified due to the scattered light (*right* panel).

Confirming the trend of shallower attenuation curve at higher  $\tilde{\tau}_{0.16}$  (Fig. 18) observationally will be challenging. However, there may be *indirect* evidence embedded in the IRX- $\beta_{UV}$  relation. We have shown in Section 4.5.1 (Eq. 22, and see also in Section 4.1) that a steeper (more SMC-like) attenuation law can lead to a redder and shallower IRX- $\beta_{UV}$  relation. This implies that the edge-on disc galaxies in a statistically large sample should appear to have redder  $\beta_{UV}$  than the face-on disc galaxies at given IRX since they on average have steeper attenuation curve. This trend has indeed been recently reported by Wang et al. (2018), who derive the result using a sample of UV-selected galaxies at  $1.3 < z < 1.7$  extracted from the CANDELS field (see also Kriek & Conroy 2013).

Note that although Wang et al. (2018) has adopted a sample of disc galaxies, which is the most straightforward way of distinguishing the viewing directions of higher or lower  $\tilde{\tau}_{0.16}$  observationally, we find that the trend of flattening attenuation curve with increasing  $\tilde{\tau}_{0.16}$  prevails among galaxies of varied morphology, as our sample also includes massive ellipticals, irregular galaxies and merging systems. That the attenuation curve is shallower in the direction of higher  $\tilde{\tau}_{0.16}$  appears to be the general trend for galaxies of all types (Fig. 18).

Finally, the inclination effect does not appear to be a major

contributor to the scatter in the IRX- $\beta_{UV}$  relation. Overall, it leads to a mean  $3\sigma$  dispersion of  $\beta_{UV}$  of  $\sim 0.1$ , which is small compared to the scatter driven by the variations of the intrinsic UV spectral slope of galaxies (Fig. 16) or the uncertainties in the underlying dust extinction law (Fig. 17).

#### 4.5.3 The effect of varying dust-to-metal mass ratio

Variations of the dust-to-metal ratio (*e.g.* De Cia et al. 2013, 2016; Wiseman et al. 2017; De Vis et al. 2019; Li et al. 2019) are another potential source of scatter in the IRX- $\beta_{UV}$  relation. So far, we have adopted a constant  $\delta_{dzt} = 0.4$  in our analysis. In this subsection, we estimate the impact of  $\delta_{dzt}$  variations on the IRX- $\beta_{UV}$  relation.

We show in Fig. 21 (*left* panel) the IRX- $\beta_{UV}$  relation of MASSIVEFIRE galaxies for the cases of  $\delta_{dzt} = 0.2, 0.4$  and  $0.8$ . Both IRX and  $\beta_{UV}$  increase with  $\delta_{dzt}$ , due to the increase of dust column density. However, the changes of IRX and  $\beta_{UV}$  are small compared to the overall galaxy-to-galaxy scatter in the relation. Increasing (decreasing)  $\delta_{dzt}$  by a factor of 2 results in a systematic increase (decrease) of IRX and  $\beta_{UV}$  by 0.15 (0.20) dex and 0.05 (0.05) on average, respectively. This again shows that dust mass (in this case, scaled to  $\delta_{dzt}$ ) is not the key factor that determines the location of galaxies on the IRX- $\beta_{UV}$  diagram (but rather, dust-to-star geometry).

Interestingly, galaxies do not move parallel to the analytic curve of the dust slab model at large IRX (or  $\beta_{UV}$ ) when  $\delta_{dzt}$  is varied. The change of the position in the IRX- $\beta_{UV}$  plane with increasing  $\delta_{dzt}$  is almost parallel to the vertical direction and is steeper than the analytic relation predicted by the dust slab model for MW dust. This indicates that the attenuation curve of galaxies becomes shallower (‘grayer’) with increasing  $\delta_{dzt}$ .

The attenuation curve varies with  $\delta_{dzt}$  for the same reason it varies with viewing angle, see Section 4.5.2. Young stars, which dominate the stellar emission at shorter wavelength, reside in more dust obscured regions. As a consequence, UV light from a significant fraction of young stars is almost completely attenuated inde-

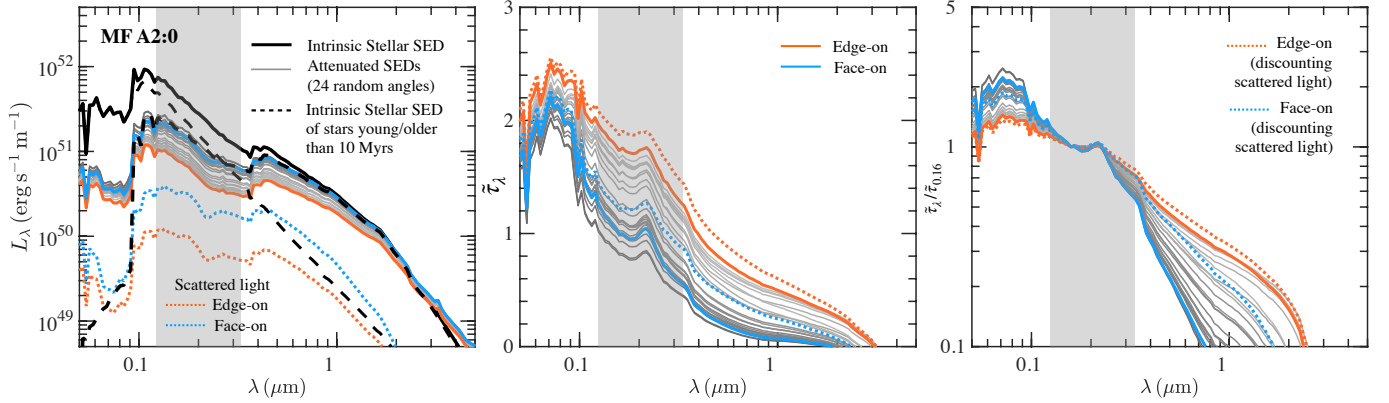


**Figure 19.** *Left panel:* The intrinsic (solid black line) and attenuated SEDs (grey+coloured lines) of a selected MASSIVEFIRE galaxy at  $z = 2$  (same as in Fig. 1). The two dashed black lines indicate the stellar emission from the stars younger/older than 10 Myrs. The grey lines show the attenuated SEDs of the 24 random viewing angles. The solid orange and blue lines correspond to the attenuated SEDs at the edge-on and face-on directions, respectively. The dotted orange and blue lines show the light that is scattered into the cameras in those two directions. *Middle panel:* The attenuation curves for the different viewing angles. The dotted orange and blue lines show the attenuation curves when the light scattered into the cameras is discounted. *Right panel:* The *normalised* attenuation curves (normalised by  $\bar{\tau}_{0.16}$ ) of the different viewing angles. The grey shaded area in each panel marks the wavelength range of  $\lambda = 1230 - 3200 \text{ \AA}$ , where the photometries are used for determining the  $\beta_{\text{UV}}$  of galaxies by the observations.  $\bar{\tau}_{\lambda}/\bar{\tau}_{0.16}$  appears to be shallower in the edge-on direction, where  $\bar{\tau}_{0.16}$  is larger.

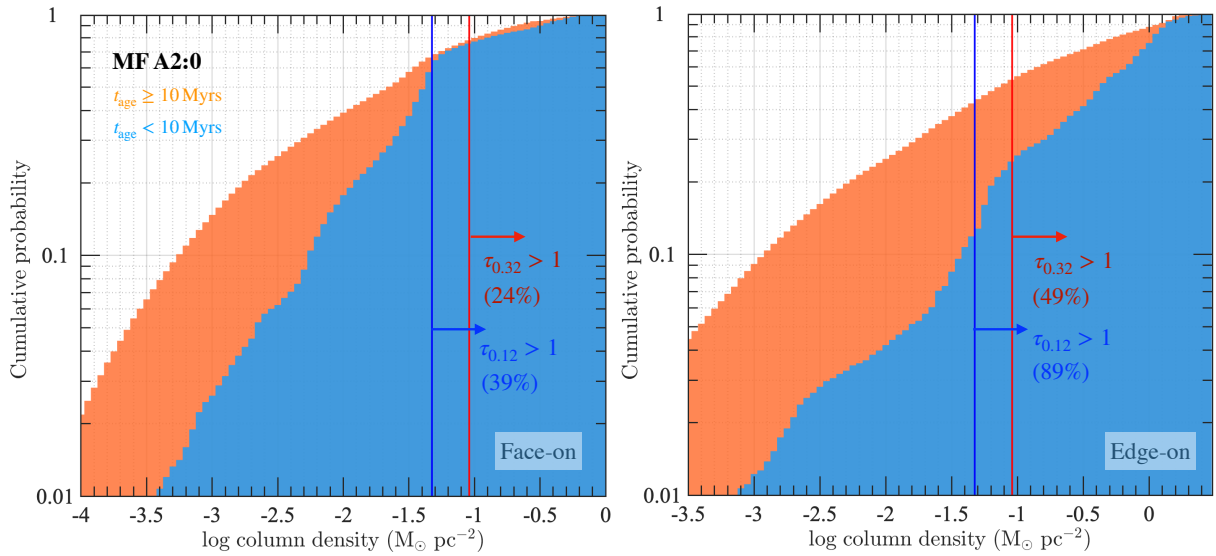


**Figure 20.** The cumulative probability distribution of dust column mass density (in units of  $\text{kg m}^{-2}$ ) of the stars of a selected  $z = 2$  MASSIVEFIRE galaxy (same as in Fig. 19) in the face-on (*left panel*) and edge-on (*right panel*) directions. In both panels, the blue and orange areas show the result of the young ( $t_{\text{age}} < 10 \text{ Myrs}$ ) and evolved ( $t_{\text{age}} \geq 10 \text{ Myrs}$ ) stars, respectively. The blue and red vertical lines indicate the column mass density above which the optical depth at  $\lambda = 1230 \text{ \AA}$  and  $\lambda = 3200 \text{ \AA}$  is over unity, assuming MW dust. The young stars dominate the stellar emission at  $\lambda = 1230 \text{ \AA}$ , while the evolved stars dominate the emission  $\lambda = 3200 \text{ \AA}$  (see *left panel* of Fig. 19). The mean dust column density of the stars is relatively higher in the edge-on direction than the face-on direction. The young stars, on the average, have higher column density than the evolved stars.

pendent of the precise value of  $\delta_{\text{dZr}}$  (provided it is large enough). If every star or star-forming region had the same column density, the shape of the attenuation curve would be independent of  $\delta_{\text{dZr}}$ , which follows from Eq. 18. The shift of the data in the IRX- $\beta_{\text{UV}}$  plane would then be parallel to the analytic curve of the dust slab model with varying  $\delta_{\text{dZr}}$ .

Finally, we note that the uncertainties in  $\delta_{\text{dZr}}$  we consider here can also be more generally viewed as equivalent to the uncertainties in the gas metallicities or the normalisation of the extinction curve, which are not well constrained observationally at high- $z$ . A

change of either of the two quantities will have the same effect on the attenuation curve as a change of  $\delta_{\text{dZr}}$  by the same factor.

#### 4.5.4 Binary evolution of stellar population

So far we have presented the results of the analysis using the SB99 stellar population model, which accounts for the evolution of single stellar populations. Recently there has also been growing attention to the effect of binary evolution of stellar populations on galaxy SED (e.g. Stanway et al. 2016; Ma et al. 2016b; Reddy et al. 2018).

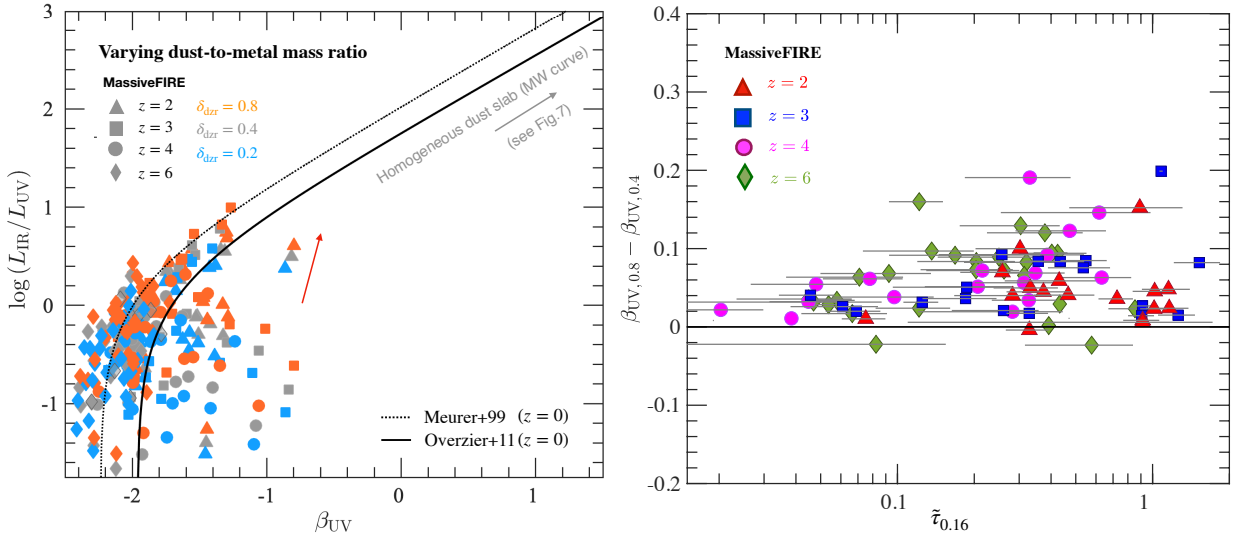


**Figure 21.** *Left panel:* The IRX- $\beta_{\text{UV}}$  relation of the MASSIVEFIRE galaxies with varying  $\delta_{\text{dzt}}$ . The red, grey and blue symbols correspond to the cases of  $\delta_{\text{dzt}} = 0.8$ ,  $\delta_{\text{dzt}} = 0.4$  and  $\delta_{\text{dzt}} = 0.2$ , respectively. The dotted and solid black lines indicate the local M99 and M99<sub>corr</sub> relations, respectively. The red arrow indicates the direction of change in the IRX- $\beta_{\text{UV}}$  relation by increasing  $\delta_{\text{dzt}}$ . The slope of the change is steeper than the analytic relation derived from the dust slab model with MW dust, indicating that  $\bar{\tau}_{\lambda}$  becomes shallower (‘grayer’) with increasing  $\delta_{\text{dzt}}$ . *Right panel:* The difference in  $\beta_{\text{UV}}$  between the cases of  $\delta_{\text{dzt}} = 0.8$  and  $\delta_{\text{dzt}} = 0.4$  as a function of  $\bar{\tau}_{0.16}$  (calculated using  $\delta_{\text{dzt}} = 0.4$ ). The horizontal error bars indicate the range of  $\bar{\tau}_{0.16}$  corresponding to  $\delta_{\text{dzt}} = 0.2 - 0.8$ .

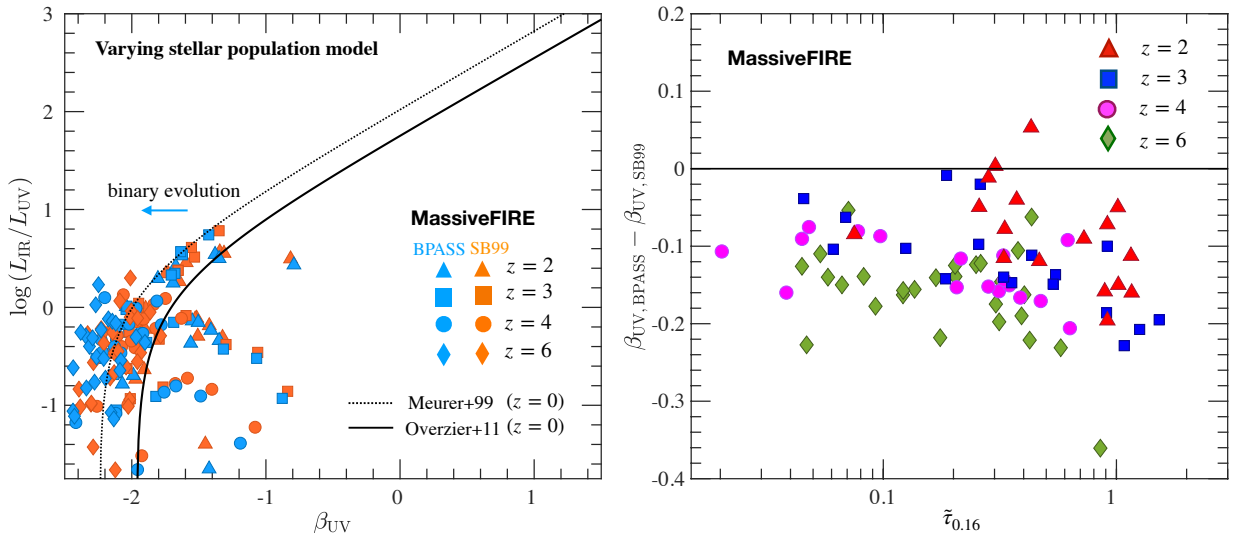


**Figure 22.** *Left panel:* Comparison between the IRX- $\beta_{\text{UV}}$  relation computed using the BPASS (blue symbols) and the SB99 (orange symbols) stellar population models. The dotted and solid black lines indicate the local M99 and M99<sub>corr</sub> relations. *Right panel:* The difference in  $\beta_{\text{UV}}$  produced by the two stellar population models as a function of  $\bar{\tau}_{0.16}$ .

Observations of the stars in the solar neighbourhood have shown that a considerable fraction of massive stars reside in binary systems (e.g. Raghavan et al. 2010; Sana et al. 2012; Duchêne & Kraus 2013; El-Badry & Rix 2018). Processes such as mass transfer between binary stars and binary mergers may increase the number of high-mass stars and effectively boost the UV part of the stellar emission.

Here we provide an estimate of the change in the IRX- $\beta_{\text{UV}}$  relation resulting from the binary evolution of stars. Specifically, we show the result derived from the recently developed ‘Binary Population and Spectral Synthesis’ (BPASS) SED template libraries (v2.2; Eldridge & Stanway 2012; Eldridge et al. 2017; Stanway & Eldridge 2018) and compare it with the fiducial model. The BPASS

libraries are tabulated by stellar age and metallicity for a number of different IMFs. We adopt the BPASS templates for the Chabrier (2003) IMF with a cut-off mass of  $100 M_{\odot}$ , which is the closest available match in the libraries to the Kroupa IMF that has been implemented into MASSIVEFIRE.

In Fig. 22, we show the IRX- $\beta_{\text{UV}}$  relation produced using the two stellar population models in the *left* panel, and also the difference in  $\beta_{\text{UV}}$  between the two models as a function of  $\bar{\tau}_{0.16}$  in the *right* panel. The BPASS templates predict slightly bluer  $\beta_{\text{UV}}$  than the SB99 templates as expected. The mean difference of  $\beta_{\text{UV}}$  between the two stellar population models is 0.12 and the difference increases slightly with redshift because i) higher- $z$  galaxies are on average more bursty and thus contain a higher fraction of young

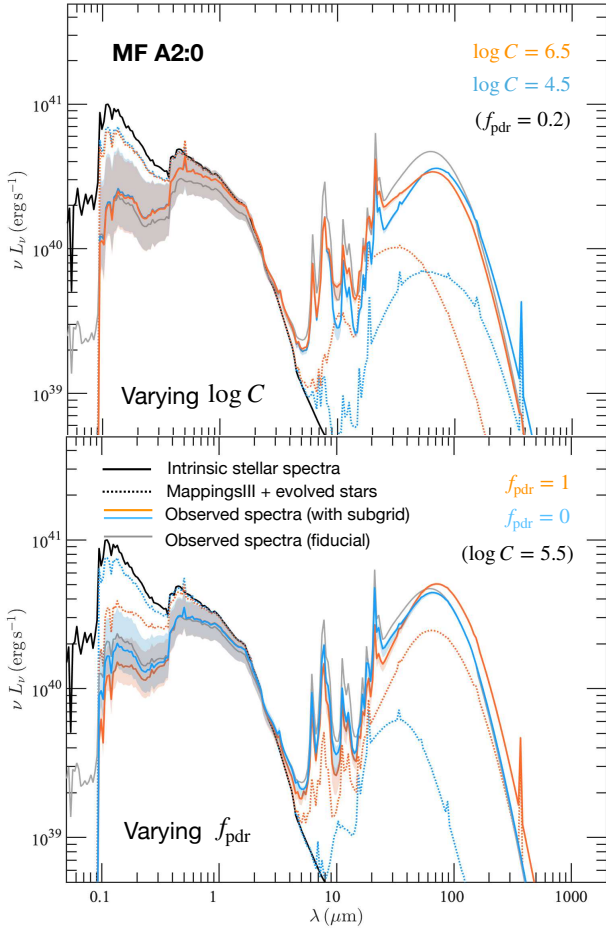


**Figure 23.** SEDs of a  $z = 2$  MASSIVEFIRE galaxy (galaxy ID: MF2:0) produced using different dust models. The coloured lines in the two panels show the results for the models where we adopt the subgrid prescription for the birth-clouds embedding the young ( $t_{\text{age}} \leq 10$  Myrs) stars. In the *upper* panel, we show the result for  $\log C = 4.5$  (blue),  $\log C = 6.5$  (orange), with fixed  $f_{\text{pdr}} = 0.2$ . In the *lower* panel, we show the observed spectra for  $f_{\text{pdr}} = 0$  (blue), and  $f_{\text{pdr}} = 1.0$  (orange) with fixed  $\log C (= 0.2)$ . In each panel, black line shows the intrinsic stellar SED, while solid orange, blue and grey lines show the angle-averaged observed SEDs, each corresponding to a different dust model. Grey line corresponds to the fiducial RT model (without the subgrid prescription). Dotted lines (orange and blue) show the combined emission from the birth-clouds (pre-processed by the dust within the birth-clouds) and the evolved ( $t_{\text{age}} > 10$  Myrs) stars (unattenuated by the diffuse dust component). The shaded orange and blue areas indicate the range of observed spectra spanning the different viewing directions for each model.

OB stars and ii) they are metal-poorer (Eldridge et al. 2017). The IRX is almost identical between the two SED models because IRX depends primarily on dust properties rather than the intrinsic emission from stars.

#### 4.5.5 The subresolution structure of the birth-clouds

As mentioned before, our simulation may only marginally resolve the typical scale of the birth-clouds embedding the young star clusters (Jonsson et al. 2010). Therefore, in order to check the uncertainty arising from small-scale ISM structures in the birth-clouds, we have performed additional RT analysis as in Liang et al. (2019), where we include a subgrid model for the birth-clouds. We sum-

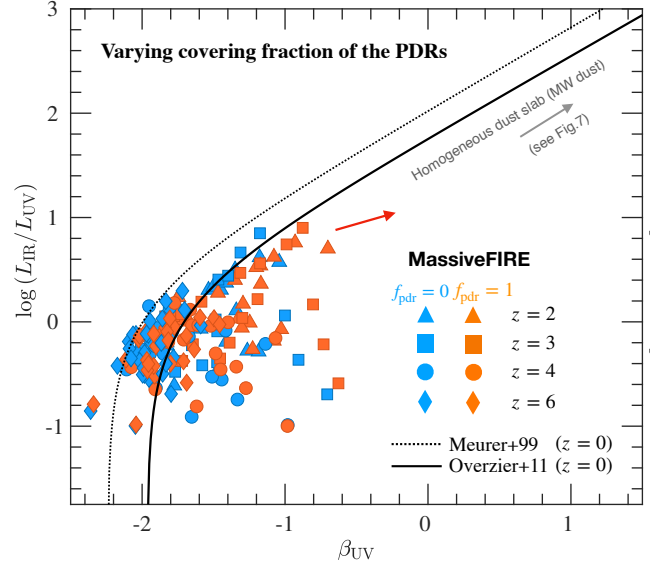


**Figure 24.** The effect of the covering fraction of the PDR ( $f_{\text{pdr}}$ ) on the IRX- $\beta_{UV}$  relation. Orange and blue symbols correspond to the cases of  $f_{\text{pdr}} = 1.0$  and  $f_{\text{pdr}} = 0$ , respectively. The dotted and solid black lines represent the local M99 and M99<sub>corr</sub> relations, respectively. The red arrow marks the direction of change in the IRX- $\beta_{UV}$  relation of galaxies with  $\text{IRX} \geq 1$  by increasing  $f_{\text{pdr}}$ . The direction appears to be shallower than the analytic curve of the dust slab model, indicating the attenuation curve of galaxies become steeper (more SMC-like) with increasing  $f_{\text{pdr}}$ .

marise the details of the subgrid model and the resulting uncertainties in the IRX- $\beta_{UV}$  relation in this subsection.

In brief, all the young ( $t_{\text{age}} \leq 10$  Myrs) star particles of a galaxy are assigned a MAPPINGSIII source SED (Groves et al. 2008). The MAPPINGSIII SED templates are parametrized by the SFR and the metallicity of the star-forming regions, the pressure of the ambient ISM, the H II region compactness ( $\log C$ ), and the covering fraction of the associated photodissociation regions (PDR) ( $f_{\text{pdr}}$ ). The PDRs in the MAPPINGSIII model are defined to have a hydrogen column depth of  $10^{22} \text{ cm}^{-2}$  (Jonsson et al. 2010) based on both the observational and theoretical grounds (Larson 1981; Solomon et al. 1987; Rosolowsky et al. 2003).

In Fig. 23 we show how the overall SED of galaxy depends on  $f_{\text{pdr}}$  (*upper* panel) and  $\log C$  (*lower* panel). From the *upper* panel, we can see that by changing  $\log C$  alone barely affects the UV-to-optical part of the SED since the dust optical depth of the birth-clouds is unaffected. It does, however, affect the temperature distribution of dust within the birth-clouds and thus the dust re-emission at FIR (Groves et al. 2008). A higher  $\log C$  leads to a warmer dust SED shape of galaxy. The integrated IR luminosity as well as the overall IRX of galaxy, however, do not depend on  $\log C$  since IRX well correlates with dust optical depth (Section 4.2), the latter being independent of  $\log C$ . Therefore,  $\log C$  does not affect the IRX- $\beta_{UV}$  relation of galaxies.

On the other hand, a higher  $f_{\text{pdr}}$  leads to an increase in the global effective optical depth of galaxy (as is shown in the *lower* panel of Fig. 23) and thus an increase in both  $\beta_{UV}$  and IRX. We show in Fig 24 the IRX- $\beta_{UV}$  relation of the MASSIVEFIRE galaxies for the cases of  $f_{\text{pdr}} = 0$  (indicating that H II regions are uncovered by the PDRs) and  $f_{\text{pdr}} = 1.0$  (indicating that the PDRs entirely surround the H II regions in the birth-clouds). The mean  $\beta_{UV}$  (IRX) of our sample is higher by 0.09 (0.02 dex) with  $f_{\text{pdr}} = 1.0$ .

We also note that the direction of change in the IRX- $\beta_{\text{UV}}$  relation with  $f_{\text{pdr}}$  appears to be shallower than the slope of the analytic curve of the dust slab model, indicating a steeper (more SMC-like) attenuation curve with increasing  $f_{\text{pdr}}$ . This is not surprising because a higher  $f_{\text{pdr}}$  means that a larger fraction of the ISM dust is associated to the birth-clouds. The hard UV photons emitted from the young stars therefore get more attenuated. This is in contrast with the scenario of increasing  $\delta_{\text{dzt}}$ , where the dust mass evenly increases at any place within the galaxies but *without* changing the dust-to-star geometry. In that case, the attenuation curve becomes shallower (‘grayer’) and the change of direction in the IRX- $\beta_{\text{UV}}$  plane with increasing  $\delta_{\text{dzt}}$  becomes steeper than the analytic curve of the toy model (Section 4.5.3).

## 5 THE DEVIATION OF THE IRX- $\beta$ RELATION DUE TO THE OBSERVATIONAL EFFECTS

In Section 4, we explored the various sources of the *intrinsic* scatter of the IRX- $\beta_{\text{UV}}$  relation and quantified their relative contribution. However, measurements of  $\beta_{\text{UV}}$  and IRX of the distant galaxies can be uncertain due to different observational effects. Specifically, we will examine the uncertainties in the  $\beta_{\text{UV}}$  measurements due to different photometric samplings in Section 5.1. We will also discuss in Section 5.2 the uncertainties in the ‘dust temperature’ (or SED shape) used to infer  $L_{\text{IR}}$  of high- $z$  galaxies by the observations, which results from the common dearth of photometric data points in the dust SEDs at high- $z$ . Finally, in Section 5.3, we review recent observational constraints of the IRX- $\beta_{\text{UV}}$  relation for a sample of LBGs at  $z \gtrsim 5$  in more detail.

### 5.1 Measuring $\beta_{\text{UV}}$ using broadband photometry

In the observational studies,  $\beta_{\text{UV}}$  are commonly estimated by fitting power-law SEDs to multi-band photometry within the wavelength range  $1230 < \lambda < 3200 \text{ \AA}$ . The true SED shape within this wavelength range, however, may not be well described by a power law (particularly, the  $2175 \text{ \AA}$  ‘bump’ feature), and thus, the derived  $\beta_{\text{UV}}$  can depend on the photometric sampling. A poor sampling of UV photometry can result in non-trivial offset of the derived  $\beta_{\text{UV}}$  (e.g. Popping et al. 2017).

This issue is more important for intermediate- and high- $z$  observations, where galaxies often have few photometric data points at rest-UV (Reddy et al. 2018; Álvarez-Márquez et al. 2019). For instance, the  $\beta_{\text{UV}}$  of the intermediate- $z$  ( $1.5 \lesssim z \lesssim 4$ ) samples by Casey et al. (2014b) & Wang et al. (2018) are estimated based on 3 photometric data points on average and the  $\beta_{\text{UV}}$  of the sources at higher- $z$  ( $z \gtrsim 5$ ) are mostly derived based on two or three data points (see Table 3 for a summary).

In Fig. 25, we show an example of the coverage of the rest-UV wavelength range by different filters at different redshifts ( $z = 2, 3, 4$  and  $6$ , corresponding to the four panels)<sup>13</sup>. The photometric sampling we use here includes the *HST* filters that were used for the 3D-HST survey (Skelton et al. 2014), combined with *GALEX*, and a  $K_s$ -band filter. In each panel, we show the intrinsic (thick black line) and the dust-attenuated SEDs (solid blue and orange lines)

of a selected MASSIVEFIRE galaxy at the corresponding redshift. We present the attenuated SEDs for both the MW (blue lines) and the SMC (orange lines) dust models. The photometric data points are calculated by convolving the attenuated SEDs with the transmission functions of the filters, which are shown below the galaxy spectra in each panel (thin black line). We also show in each panel the best-fit power-law curves obtained using different sampling of photometric data points (coloured dotted and dot-dashed lines). The dot-dashed curves correspond to the case where the two data points are both blueward of the ‘bump’ at  $\lambda = 2175 \text{ \AA}$ , whereas the dotted curves correspond to the case where the two data points are on either side of the ‘bump’.

Looking at the figure, it is clear that galaxy spectra are not pure power laws at rest-UV wavelengths. The spectra show a deficit of flux at  $1700 < \lambda < 2700 \text{ \AA}$  (indicated by dark grey area) due to the enhanced extinction near the  $2175 \text{ \AA}$  ‘bump’.  $\beta_{\text{UV}}$  derived with and without the data points in this regime have noticeable differences. We show in each panel of the figure the  $\beta_{\text{UV}}$  derived using two photometric samplings for each spectrum, one with two photometric data points lying both blueward of the ‘bump’ and the other with the two data points lying on either side of the peak and outside the ‘bump’ regime (dark grey area). For MW (SMC) dust, the former sampling yields noticeably bluer (redder)  $\beta_{\text{UV}}$ .

The difference in  $\beta_{\text{UV}}$  for the different photometric samplings increases with larger  $\tilde{\tau}_{0.16}$ , in line with the prediction of the dust slab model. Specifically, we can rewrite Eq. 15 for two different photometric samplings, *i.e.*

$$\beta_{\text{UV},1} = \beta_{\text{UV},0} + \mathcal{Z}_1 \tilde{\tau}_{0.16}, \quad (23)$$

and

$$\beta_{\text{UV},2} = \beta_{\text{UV},0} + \mathcal{Z}_2 \tilde{\tau}_{0.16}. \quad (24)$$

where  $\mathcal{Z}_1$  and  $\mathcal{Z}_2$  represent the steepness of the *same* attenuation curve and  $\beta_{\text{UV},1}$  and  $\beta_{\text{UV},2}$  represent the UV spectral slopes that are measured by two different combinations of bandpass filters. By subtracting one equation by the other, we obtain

$$\beta_{\text{UV},1} - \beta_{\text{UV},2} = (\mathcal{Z}_1 - \mathcal{Z}_2) \tilde{\tau}_{0.16}, \quad (25)$$

*i.e.* the difference between the estimated  $\beta_{\text{UV}}$  scales linearly with  $\tilde{\tau}_{0.16}$ . Since IRX increases with  $\tilde{\tau}_{0.16}$ ,  $\beta_{\text{UV}}$  measurements of galaxies of higher IRX are expected to be more influenced by the photometric sampling effect.

In Fig. 26, we explicitly show the impact of the photometric samplings on the derived IRX- $\beta_{\text{UV}}$  relation using both the analytic solutions of the dust slab model and RT calculations of the MASSIVEFIRE galaxies for  $z = 6$ . For the analytic solutions, we show the results for both the MW and SMC dust models and for three filter combinations,  $1230+3200 \text{ \AA}$ ,  $F105W+K_s$  and  $F105W+F160W$ . For the RT calculations, we only present the results for MW dust and for the filter combinations of  $1230+3200 \text{ \AA}$  and  $F105W+F160W$ . The latter has both filters blueward of the  $2175 \text{ \AA}$  ‘bump’, resulting in the lowest ‘measured’  $\beta_{\text{UV}}$  among the three samplings (see the *lower right* panel of Fig. 25).

The most significant uncertainty in the derived IRX- $\beta_{\text{UV}}$  relation is the effect of the  $2175 \text{ \AA}$  ‘bump’ feature in the MW extinction curve. With  $F105W+F160W$ , the derived  $\beta_{\text{UV}}$  can be much ‘bluer’ than the cases where both sides of the peak are covered (e.g.  $1230+3200 \text{ \AA}$ ). We will show in Section 5.3 that the location of some MASSIVEFIRE galaxies in the IRX- $\beta_{\text{UV}}$  plane derived using the  $F105W+F160W$  filters (blue filled symbols) is in good

<sup>13</sup> This figure is adapted from Fig. 9 of Popping et al. (2017). Note that the authors also present other filter combinations (see the appendix of that paper). In this work, we only use one combination as an example for the impact of photometric sampling on  $\beta_{\text{UV}}$  estimates.



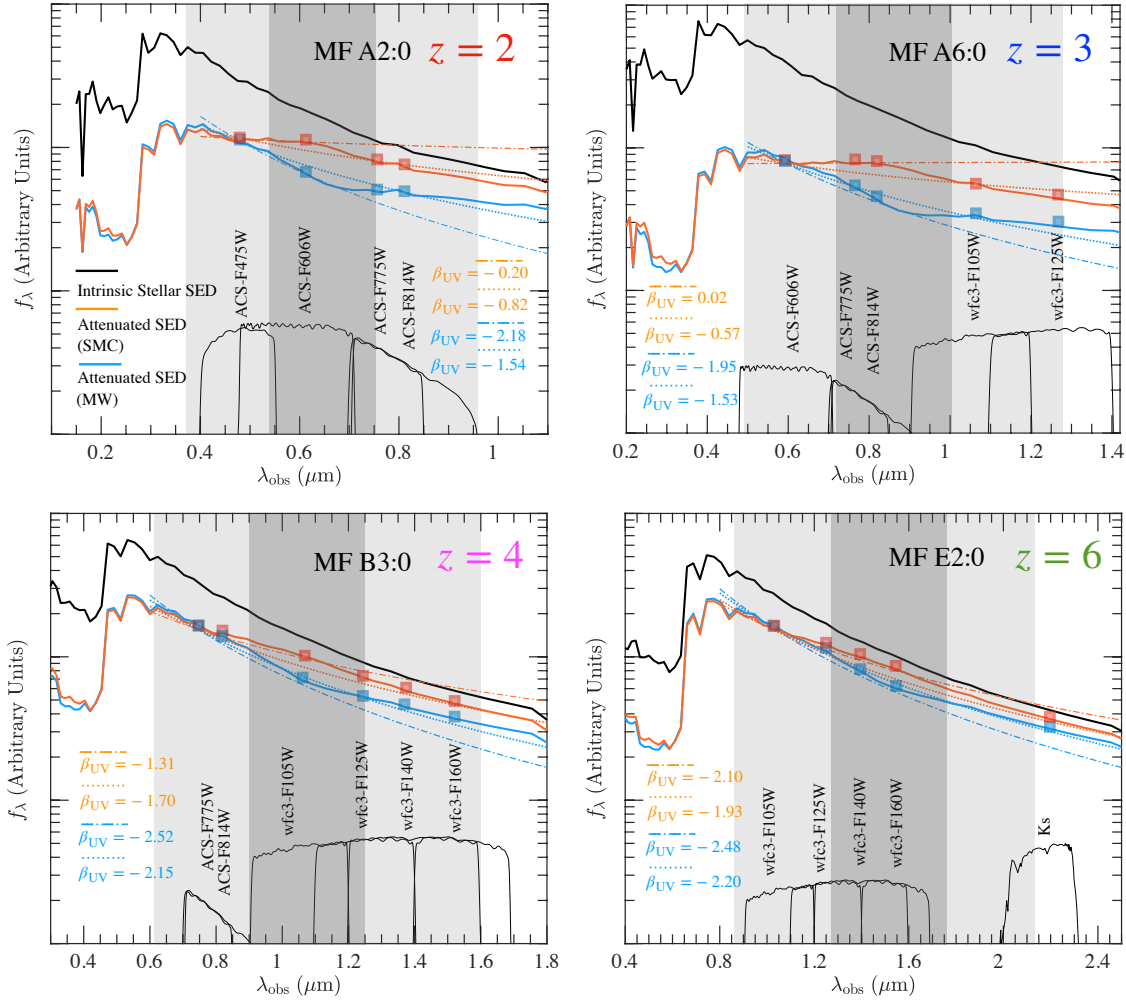


**Figure 25.** The coverage of the rest-frame UV wavelength regime by different filters for redshifts running from  $z = 2$  to  $z = 6$  (adapted from Fig. 9 of Popping et al. 2017). The photometric sampling includes the *HST* filters as part of the 3D-*HST* survey, on top of *GALEX*, and a  $K_s$ -band filter. In each panel, the thick solid black curve shows the intrinsic stellar SED at FUV-to-NUV of a MASSIVEFIRE galaxy at the corresponding redshift. The blue and orange lines in each panel show the attenuated spectra for the MW and SMC dust, respectively. The photometric data points of the attenuated spectra are marked by coloured squares. The relevant filters at each redshift and their transmission functions are plotted below the galaxy spectra. In each panel, the coloured dotted and dot-dashed lines show the best-fit power-law curves (for estimating  $\beta_{UV}$ ) to the two different combinations of photometric data points. From  $z = 2$  to  $z = 6$ , the dotted (dot-dashed) line in the panel shows the result of the filter combinations of F475W+F775W (F606W), F606W+F105W (F814W), F775W+F125W (F105W) and F105W+ $K_s$  (F160W). The light grey areas indicate the wavelength range ( $1230 < \lambda < 3200 \text{ \AA}$ ) where the photometric data points are used for estimating  $\beta_{UV}$  by the observations, while the dark grey areas show the regime ( $1700 < \lambda < 2700 \text{ \AA}$ ) of the ‘bump’ feature in the MW extinction curve.

agreement with a few detected LBGs at  $z \gtrsim 5$ , which appears to be significantly ‘bluer’ than the M99 relation. On the other hand, photometric sampling appears to be a less important issue for SMC dust due to the absence of the  $2175 \text{ \AA}$  ‘bump’ feature. Using the F105W+F160W filter combination leads to a slightly redder  $\beta_{UV}$  in this case.

The results we present here are derived using the local MW and SMC dust curves of the WD01 model. At higher redshifts, the shape of the dust extinction curve and, in particular, the strength of the  $2175 \text{ \AA}$  ‘bump’ feature are poorly constrained, although there has been preliminary evidence showing that high- $z$  galaxies tend to exhibit weaker ‘bump’ than the MW curve (e.g. Schady et al. 2012; Kriek & Conroy 2013; Zafar et al. 2018). Therefore, the significant offset of  $\beta_{UV}$  presented here should be viewed as a conservative maximum estimate.

## 5.2 The uncertainties in the ‘dust temperature’

Estimating  $L_{IR}$  (and hence IRX) of galaxies at  $z \gtrsim 5$  reliably can be challenging (Casey 2012; Liang et al. 2019) because source detection at this epoch is difficult due to the high confusion noise. The majority of objects with detected dust emission at this epoch have only one or two photometric data points derived with ALMA (typically at band 6 or 7). To extrapolate  $L_{IR}$  of these galaxies, often a specific dust SED shape is adopted and the ‘dust temperature’ is set to a specific value (35 K) (Bouwens et al. 2016; Liang et al. 2019). The derived IRX thus strongly depends on this assumed ‘dust temperature’.

Recently, there has been growing evidence that galaxies at high- $z$  (i.e.,  $z \gtrsim 5$ ) have higher ‘dust temperatures’ than those at low and intermediate redshifts (e.g., Capak et al. 2015; Bouwens et al. 2016; Matthee et al. 2017; Harikane et al. 2020). Specifically, it has been found that applying a constant ‘dust temperature’ of 35 K to

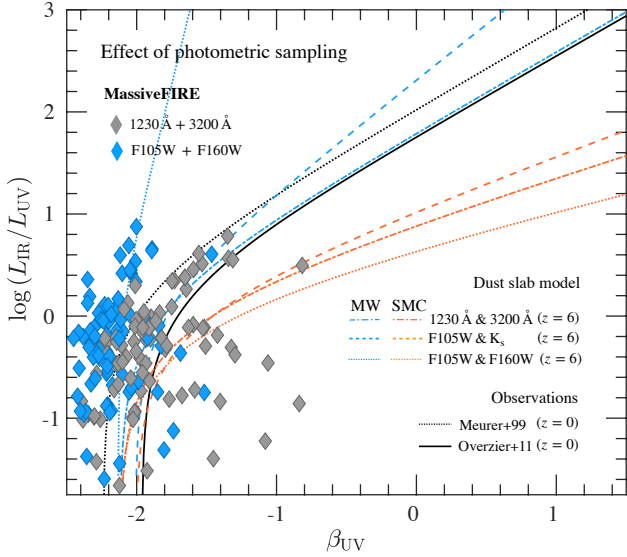


**Figure 26.** The effect of photometric sampling on the derived IRX- $\beta_{UV}$  relation. The grey symbols represent the result of the MASSIVEFIRE sample for MW dust with  $\beta_{UV}$  measured at  $\lambda = 1230$  and  $3200 \text{ \AA}$ . The blue symbols show the result with  $\beta_{UV}$  estimated using the filter combination of *HST* F105W and F160W bands, as if the galaxies were all at  $z = 6$ . The blue and orange lines show the analytic curves derived from the dust slab model for the MW and SMC dust of WD01, respectively. The dotted, dash-dotted and solid lines correspond to the cases where  $\beta_{UV}$  of the attenuated spectra (redshifted to  $z = 6$ ) is estimated using the filter combination of F105W+F160W bands, F105W+K<sub>s</sub> bands and at rest-frame  $1230 \text{ \AA}$  and  $3200 \text{ \AA}$ , respectively. All these curves are produced using the SB99 template SEDs for the case of  $t_{\text{age}} = 50 \text{ Myrs}$  and  $Z_* = 0.1Z_{\odot}$ . The black solid and dotted lines represent the M99 and M99<sub>corr</sub> relations, respectively. Photometric sampling affects the measured IRX- $\beta_{UV}$  relation of galaxies.

gether with a MBB function will lead to a significant IRX deficit of high- $z$  galaxies, resulting in galaxies far below the canonical M99 relation. Aside from having steeper dust attenuation curves, these galaxies may have a higher dust temperature so that the observed submm flux is lower for a given  $L_{IR}$ .

Motivated by these observations, a number of recent theoretical studies have investigated the ‘dust temperature’ of high- $z$  galaxies in detail. The dust SED shape of high- $z$  galaxies is found to differ noticeably from the template SEDs commonly adopted in the literature (e.g. Liang et al. 2019; Ma et al. 2019). Specifically, high- $z$  galaxies show more prominent emission on the Wien side of the dust SED compared to the low- $z$  counterparts in the cosmological ‘zoom’ galaxy simulations. This part of the SED is associated with the warm dust component that is exposed to the hard UV radiation from the newly born young stars (Casey 2012). The more prominent emission of the warm dust component in high- $z$  galaxies can be attributed to enhanced star formation activity (Safarzadeh et al. 2017a; Liang et al. 2019; Ma et al. 2019) and/or a higher mean dust column density in vicinity of young stars (Behrens et al. 2018; Sommovigo et al. 2020) in high- $z$  galaxies. Although the Wien side of the dust SED of galaxies at  $z \geq 5$  is typically not constrained by observations, a number of low- and intermediate-redshift observations with *Herschel* have found a trend of enhanced mid-IR emission with increasing redshift based on stacking analysis (e.g., Béthermin et al. 2015; Casey et al. 2018a; Schreiber et al. 2018).

Hence, in order to account for this evolution of SED shape with redshift, an increase in ‘dust temperature’ is needed to convert ALMA flux densities to  $L_{IR}$  with a MBB function. Using the

MASSIVEFIRE galaxy sample at  $z = 2 - 6$ , Liang et al. (2019) derived the best-fit formula for this ‘equivalent’ dust temperature (see Eq.9 of Liang et al. 2019 for its definition) using redshift and  $\delta_{dZr}$  as variables, *i.e.*,

$$T_{\text{eqv}} = T_0 (1+z)^\alpha (\delta_{dZr}/0.4)^\gamma. \quad (\text{L19}) \quad (26)$$

The ‘dust temperature’ for inferring  $L_{IR}$  depends on the assumed functional shape of the dust SED and the observing bandpass, and it does not reflect the *physical* temperature of the bulk of the ISM dust (see Liang et al. 2019, for the details). For ALMA band 7 (6) fluxes, the best-fit parameter values are  $T_0 = 24.4$  (22.3) K,  $\alpha = 0.31$  (0.36) and  $\gamma = -0.13$  (-0.15). The anti-correlation with  $\delta_{dZr}$  indicates that an increase in  $\delta_{dZr}$  leads to a reduced mass fraction of the dust in the ISM being exposed to the hard UV photons from the young stars and hence less prominent emission on the Wien side (Scoville 2013; Faisst et al. 2017; Liang et al. 2019). The  $\delta_{dZr}$  of high- $z$  galaxies is not yet well constrained observationally.

Using Eq. 26 can mitigate the systematic underestimates of IRX at higher- $z$  when only ALMA data is available, considering that the redshift can often be determined through spectroscopy or photometry. We illustrate this in Fig. 27, where we show the difference between the IRX converted from the single-ALMA-band flux and the true value,  $\Delta(\log \text{IRX})$ , as a function of  $\tau_{0.16}$  for the MASSIVEFIRE sample at different redshifts. We show the results for the cases where we adopt a constant  $T_{\text{eqv}} = 35 \text{ K}$  and the redshift-dependent  $T_{\text{eqv}}$  following Eq. 26 in the *left* and *right* panels, respectively. It can be seen that by using  $T_{\text{eqv}} = 35$ , the IRX is systematically underestimated for galaxies above  $z = 2$ . The IRX of  $z = 6$  galaxies (green diamonds) is underestimated by  $\sim 0.4$  dex (a factor of  $\sim 3$ ).  $T_{\text{eqv}}$  based on Eq. 26 can reduce the systematic error in the IRX estimates (*right* panel). We note that Eq. 26 is in good agreement with estimates based on source number counts in recent deep ALMA surveys (e.g., Bouwens et al. 2016; Casey et al. 2018a,b).

However, we can see from the *right* panel that the scatter in  $\Delta \log(\text{IRX})$  is non-trivial, even after accounting for the systematic redshift evolution of  $T_{\text{eqv}}$ . The  $1\sigma$  dispersion of  $\Delta \log(\text{IRX})$  is 0.22 (corresponding to a factor of  $\sim 1.67$  in IRX). This non-trivial scatter is due to the variations in the dust SED shape at fixed redshift, which are not well accounted for by a redshift-dependent formula for  $T_{\text{eqv}}$ . This is not surprising because galaxies at the same redshift have large dispersion in the starburstiness (*i.e.* sSFR, see e.g. Rodighiero et al. 2011; Sparre et al. 2017; Feldmann 2017) and very different spatial configuration of dust distribution near the UV-emitting OB stars (e.g. Lombardi et al. 2014; Faisst et al. 2017; Cochrane et al. 2019; Sommovigo et al. 2020). The prominence of the emission of the warm dust component at rest-MIR can thus have large galaxy-to-galaxy variations at a given redshift.

We expect that galaxies with higher  $\tau_{0.16}$  show more prominent emission on the Wien side of the dust SED when  $\delta_{dZr}$  is fixed. Galaxies with higher  $\tau_{0.16}$  tend to be more bursty (Fig. 13, and see Section 4.3), leading to a stronger emission from warm dust component. From the *right* panel of Fig. 27, we indeed see a clear anti-correlation between  $\Delta(\log \text{IRX})$  and  $\tau_{0.16}$ , indicating that a higher  $T_{\text{eqv}}$  is needed for recovering the  $L_{IR}$  of galaxies with higher  $\tau_{0.16}$ . Hence, if  $\tau_{0.16}$  were known, it could be used to further improve the accuracy of the IRX estimate.

Using the least- $\chi^2$  method, we derive the best-fit relation be-

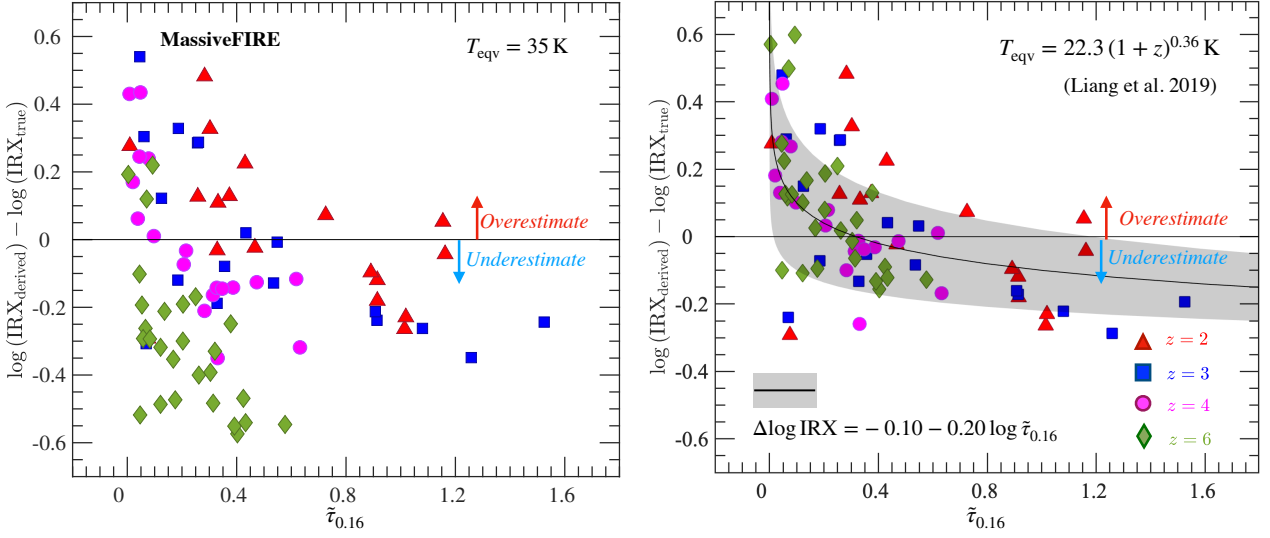


**Figure 27.** The offset between IRX derived from converting ALMA band 6 (1.1 mm) flux densities and the true IRX of galaxies as a function of  $\tilde{\tau}_{0.16}$ . In the *left* panel, we show the result for the case where we adopt a MBB function (using  $\beta_{\text{IR}} = 2.0$ ) with a constant  $T_{\text{eqv}} = 35$  K submm-flux-to-IR-luminosity conversion. In the *right* panel, we show the result when a redshift-dependent  $T_{\text{eqv}}$  following Eq. 26 (using  $\delta_{\text{dzt}} = 0.4$ ) is employed for the conversion. The grey semi-transparent area indicates the  $3\sigma$  probability contour of the distribution of the data. The required  $T_{\text{eqv}}$  appears to show an additional positive correlation with  $\tilde{\tau}_{0.16}$  at fixed redshift.

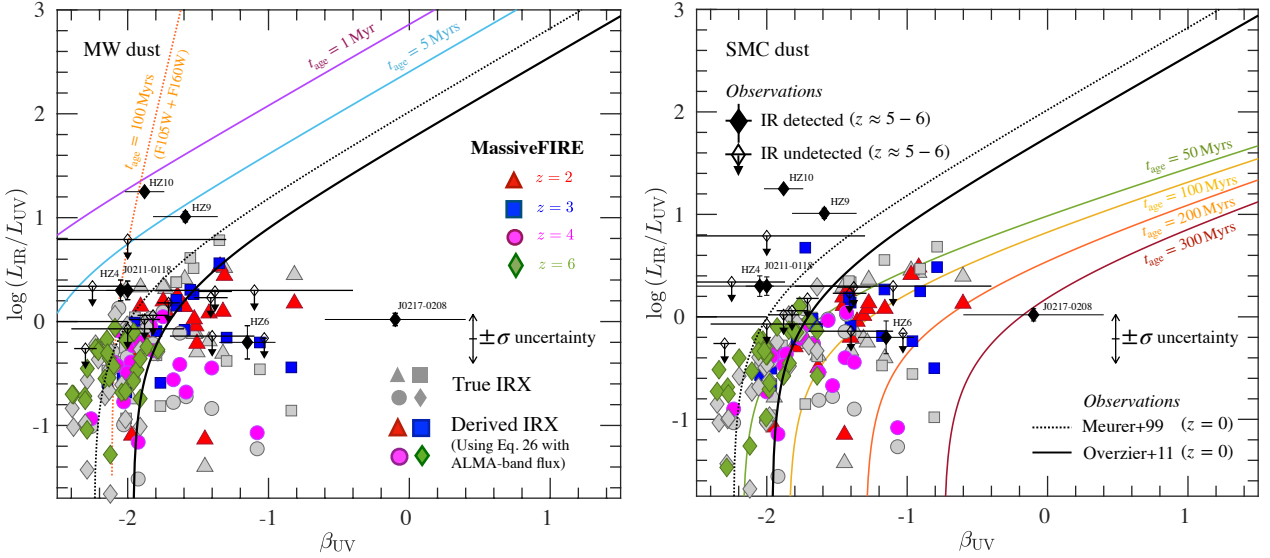


**Figure 28.** Comparison of the IRX- $\beta_{\text{UV}}$  relation of the MASSIVEFIRE galaxies to the compilation of the recent observational data at  $z \approx 5 - 6.5$ . The  $L_{\text{IR}}$  of the observational data are converted from their reported ALMA-band fluxes (either band 6 or 7) using a standard MBB function (assuming  $\beta_{\text{IR}} = 2.0$ ) with  $T_{\text{eqv}}$  following Eq. 26 (assuming  $\delta_{\text{dzt}} = 0.4$ ). For undetected sources, downward arrows mark the  $3\sigma$  upper limits of their IRX. The coloured filled symbols represent the result for MASSIVEFIRE derived using the same method as the observational data. For purpose of reference, the result for the true IRX is shown by grey symbols. In the *left* panel, the violet and blue lines indicate the analytic curves of the dust slab model for MW dust and stellar age  $t_{\text{age}} = 1$  and 5 Myrs, respectively. For these two curves,  $\beta_{\text{UV}}$  is measured at  $\lambda = 1230$  and  $3200 \text{ \AA}$ . The orange dotted line represents the case where  $t_{\text{age}} = 100$  Myrs while  $\beta_{\text{UV}}$  is measured at the *HST* F105W and F160W bands for the attenuated spectra (redshifted to  $z = 6$ ), both being blueward of the  $2175 \text{ \AA}$  ‘bump’ for  $z = 6$ . In the *right* panel, the green, brown, orange and dark red lines represent the analytic curves for SMC dust curve and  $t_{\text{age}} = 50, 100, 200$  and  $300$  Myrs, respectively.  $\beta_{\text{UV}}$  is measured at  $\lambda = 1230$  and  $3200 \text{ \AA}$ . In both panels, the dotted and solid black lines indicate the local M99 and M99<sub>corr</sub> relations, respectively.

tween  $\Delta \log(\text{IRX})$  and  $\tilde{\tau}_{0.16}$  for the MASSIVEFIRE sample at  $z = 2 - 6$  over the range of  $\tilde{\tau}_{0.16} = 0.01 - 1.6$ ,

$$\Delta \log(\text{IRX}) = -0.10 \pm 0.04 - (0.20 \pm 0.04) \log \tilde{\tau}_{0.16}. \quad (27)$$

Knowing that the derived IRX is proportional to  $(T_{\text{eqv}})^{3+\beta}$  for a given ALMA broadband flux (at band 6 or 7) in the Rayleigh-Jeans

regime (see Eq. 10 of Liang et al. 2019), we can then translate the above equation to a modified version of Eq. 26, including a correction term of  $\tilde{\tau}_{0.16}$ , *i.e.*

$$T_{\text{eqv}} = T_0 (1+z)^\alpha (\delta_{\text{dzt}}/0.4)^\gamma \Gamma, \quad (28)$$

where  $\Gamma = 1.05 (\tilde{\tau}_{0.16})^{0.04}$ .

### 5.3 The IRX- $\beta$ relation at $z \geq 5$

Fig. 28 shows a compilation of ALMA-detected LBGs at  $z \approx 5-6.5$  (see Table 3 for their observational properties). 6 out of 19 objects in this sample have  $> 3\sigma$  detection at either ALMA band 6 or 7. For the rest of the sample, we show in the figure their upper  $3\sigma$  limits. We notice that  $L_{\text{IR}}$  of these galaxies was originally derived using different dust temperatures and dust SEDs. Hence, to make a fair comparison, we convert the reported ALMA-band fluxes to  $L_{\text{IR}}$  and hence IRX using the same MBB function (with  $\beta_{\text{IR}} = 2.0$ ), constant  $\delta_{\text{dzt}} = 0.4$  and  $T_{\text{eqv}}$  from Eq. 26 (we still adopt Eq. 26 instead of Eq. 28 because  $\tilde{\tau}_{0.16}$  is in practice very difficult to measure). We also derive  $L_{\text{IR}}$  and IRX of the MASSIVEFIRE sample by the same method.

The observational data at  $z \geq 5$  shows a large scatter in the IRX- $\beta_{\text{UV}}$  plane. While a few objects with ALMA detections (HZ10, HZ9, HZ4, and J0211-0118) appear to be much ‘bluer’ than the canonical M99 relation (solid black line), there are also a few objects (HZ6 and J0217-0208) that lie below the relation. To better estimate the conditions of the different objects in the compiled sample, we also overplot a set of analytic curves for different stellar population ages and dust extinction curves.

In the *left* panel, we show the analytic solutions for MW dust with a stellar population age of  $t_{\text{age}} = 1$  Myr and 5 Myrs, and  $\beta_{\text{UV}}$  are measured at  $\lambda = 1230$  and  $3200 \text{ \AA}$ . The galaxy that shows the largest offset from the M99 relation on the ‘blue’ side, HZ10, can be accounted for by a very young UV-weighted  $t_{\text{age}}$  of  $\sim 1$  Myr. Alternatively, its location in the IRX- $\beta_{\text{UV}}$  plane can also be explained by a strong  $2175 \text{ \AA}$  ‘bump’ in the attenuation curve, given that  $\beta_{\text{UV}}$  of this object was measured using only the photometry blueward of the ‘bump’ (see Table 3, and also Barisic et al. 2017). We show the analytic IRX- $\beta_{\text{UV}}$  relation for  $t_{\text{age}} = 100$  Myrs at  $z = 6$  and  $\beta_{\text{UV}}$  being measured at the *HST* F105W and F160W bands. The location of HZ10 is also consistent with the analytic curve of this relatively old  $t_{\text{age}}$  because of the ‘bump’ feature in the MW extinction curve. Therefore, to distinguish the potential contamination by the ‘bump’ feature to the  $\beta_{\text{UV}}$  measurements of the  $z \geq 5$  galaxies, observations in the  $K_s$ -band may be need (Popping et al. 2017).

In the *right* panel, we show the analytic IRX- $\beta_{\text{UV}}$  relation for SMC dust curve and a much older stellar population. The location of the ‘reddest’ galaxy, J0217-0208, is consistent with  $t_{\text{age}} = 300$  Myrs, close to the oldest UV-weighted stellar age of the MASSIVEFIRE sample (Fig. 16). However, the location of J0217-0208 indicates a higher  $\tilde{\tau}_{0.16}$  than the MASSIVEFIRE galaxy of similar age. J0217-0208 may also have younger UV-weighted  $t_{\text{age}}$  and an attenuation curve steeper than the SMC curve. This can either be due to a steep intrinsic extinction curve, or a heavier dust obscuration of the young stars. Furthermore, the location of the detected source, HZ6, and the upper  $3\sigma$  limit of the undetected source, HZ5, imply a  $t_{\text{age}}$  (or a lower limit of  $t_{\text{age}}$  for the undetected source) between 100 and 200 Myrs. The data points or upper  $3\sigma$  limits of the rest of the objects are all above the curve for  $t_{\text{age}} = 100$  Myrs.

The mean IRX of the undetected objects at  $z \geq 5$  derived from their stacked ALMA flux appeared to lie significantly below the canonical M99 relation (Capak et al. 2015). This tension was alleviated by the work of Barisic et al. (2017), where the authors reassessed the  $\beta_{\text{UV}}$  measurements using the *HST*/Wide Field Camera 3 near-IR imaging and found a systematic bias of the previous ground-based data toward redder slopes. In this work, we re-derive the IRX of these objects using the best-fit formula for  $T_{\text{eqv}}$  (Eq. 26).

We find that the majority of the upper  $3\sigma$  limits of the undetected sources (10 out of 13) are in agreement with the canon-

ical M99 relation and the IRX- $\beta_{\text{UV}}$  relation for SMC dust with  $t_{\text{age}} = 50$  Myrs. The few objects that show an IRX deficit compared to these relations can be explained by a relatively evolved stellar population, which is common in MASSIVEFIRE. Note that IRX estimates of high- $z$  galaxies based on ALMA-band fluxes alone can have non-trivial uncertainties due to the variations in the dust SED shape of galaxies at the wavelength range not covered by the ALMA bands. We mark the  $\pm 1\sigma$  uncertainty in the IRX estimate in both panels of Fig. 28.

## 6 SUMMARY AND CONCLUSIONS

The empirical relation between UV spectral slope ( $\beta_{\text{UV}}$ ) and infrared excess (IRX) of galaxies is frequently adopted for estimating  $L_{\text{IR}}$  and the dust-obscured SFR of distant galaxies when only UV measurements are available; however, observations have shown evidence of non-trivial scatter of this relation among different galaxy populations. In this work, we explore the nature of the IRX- $\beta_{\text{UV}}$  relation and the different origins of the scatter. We adopt a sample of galaxies at  $z = 2 - 6$  ( $M_* \approx 10^9 - 10^{12} M_{\odot}$ ) that are extracted from the cosmological ‘zoom-in’ simulations MASSIVEFIRE (Feldmann et al. 2016, 2017), which are part of the Feedback in Realistic Environments (FIRE) project (Hopkins et al. 2014). Using the dust radiative transfer tool, SKIRT (Baes et al. 2011; Baes & Camps 2015), we produce spatially resolved UV-to-mm SEDs for the MASSIVEFIRE sample, and study their observational properties, in particular  $\beta_{\text{UV}}$ , integrated UV and IR luminosities.

The main findings of this work are:

- Using the standard MW dust extinction law, the MASSIVEFIRE sample is in broad agreement with the canonical relation of Meurer et al. (1999) (M99) derived using a local starburst population (Section 3.1 & Section 3.2). The deviation from the M99 relation correlates with the *UV-luminosity*-weighted stellar age ( $t_{\text{age, UV}}$ ) (see Eq. 20), but not with the mass-weighted stellar age ( $t_{\text{age, mw}}$ ).
- The UV *effective* optical depth of galaxies ( $\tilde{\tau}_{0.16}$ ) is well correlated with IRX, specifically,  $\text{IRX} \propto e^{\tilde{\tau}_{0.16}} - 1$  (Eq. 19). This relation is in agreement with the analytic curve derived using the dust slab model (Section 4.1). In contrast,  $\tilde{\tau}_{0.16}$  is weakly correlated to  $\beta_{\text{UV}}$  due to the large variations in the intrinsic UV spectral slope ( $\beta_{\text{UV}, 0}$ ) of galaxies (Section 4.2). Thus,  $\beta_{\text{UV}}$  should not be used as reliable proxy for UV optical depth.
- The increment (reddening) of UV spectral slope,  $\beta_{\text{UV}} - \beta_{\text{UV}, 0}$ , scales proportionally with  $\tilde{\tau}_{0.16}$ , broadly consistent with the expectation of the dust slab model. The slope of this linear relation depends on the steepness of the dust attenuation curve of galaxy. The shape of the attenuation curve and that of the underlying dust extinction curve are generally different depending on the dust-to-star geometry (Section 4.2).
- $\tilde{\tau}_{0.16}$  (or equivalently, IRX) depends on the spatial configuration of dust with respect to star-forming regions in the galaxies and is not well correlated with  $M_{\text{dust}}$ .  $\tilde{\tau}_{0.16}$  increases during the starbursts as gas/dust configuration becomes more concentrated due to instabilities. Two galaxies of similar  $M_{\text{dust}}$  can have significantly different IRX (by over an order of magnitude) (Section 4.3).
- A galaxy evolves in the IRX- $\beta_{\text{UV}}$  plane over cosmic time. The evolutionary trajectory consists of counter-clockwise rotation on relatively short timescales of  $\lesssim 100$  Myrs. During starbursts, galaxies move upwards and leftwards in the plane (due

**Table 3.** Observed properties of the galaxy compilation at  $z \approx 6$  that are shown in Figure 28.

ID	$z$	$\beta_{UV}$	Rest-UV Photometry	$\log(L_{UV}/L_{\odot})$	$S$ ( $\mu\text{Jy}$ ) <sup>1,2</sup>	$\log(L_{IR}/L_{\odot})$ <sup>1,3</sup>	References <sup>4</sup>
HZ8	5.1533	$-1.41 \pm 0.12$	F105W, F125W, F160W	$11.04 \pm 0.02$	$< 90$ (7)	$< 11.26$	C15, B17
HZ7	5.2532	$-1.38 \pm 0.12$	F105W, F125W, F160W	$11.05 \pm 0.02$	$< 108$ (7)	$< 11.33$	C15, B17
HZ6	5.2928	$-1.15 \pm 0.20$	F105W, F125W, F160W	$11.47 \pm 0.10$	$129 \pm 36$ (7)	$11.07 \pm 0.12$	C15, B17
HZ5	5.310	$-1.03 \pm 0.02$	F105W, F125W, F160W	$11.45 \pm 0.01$	$< 96$ (7)	$< 11.28$	C15, B17
HZ9	5.541	$-1.59 \pm 0.23$	F105W, F125W, F160W	$10.95 \pm 0.02$	$516 \pm 42$ (7)	$11.96 \pm 0.04$	C15, B17
HZ3	5.5416	$-1.71 \pm 0.08$	F105W, F125W, F160W	$11.08 \pm 0.01$	$< 93$ (7)	$< 11.25$	C15, B17
HZ4	5.544	$-2.05 \pm 0.10$	F105W, F125W, F160W	$11.28 \pm 0.01$	$202 \pm 50$ (7)	$11.58 \pm 0.10$	C15, B17
HZ10	5.6566	$-1.88 \pm 0.14$	F105W, F125W, F160W	$11.14 \pm 0.02$	$1261 \pm 44$ (7)	$12.39 \pm 0.02$	C15, B17
HZ2	5.6597	$-1.82 \pm 0.11$	F105W, F125W, F160W	$11.15 \pm 0.01$	$< 87$ (7)	$< 11.20$	C15, B17
HZ1	5.6885	$-1.88 \pm 0.11$	F105W, F125W, F160W	$11.21 \pm 0.01$	$< 90$ (7)	$< 11.22$	C15, B17
A383-5.1	6.029	$-2.0 \pm 0.7$	F814W, F110W, F125W, F160W, IRAC 3.6 $\mu\text{m}$ , 4.5 $\mu\text{m}$	$10.34 \pm 0.13$	$< 33$ (6)	$< 11.12$	R11, K16
J1211-0118	6.0293	$-2.0 \pm 0.5$	Subaru/HSC $z$ and $y$ bands	11.43	$348 \pm 72$ (7)	$11.73 \pm 0.09$	H20
J0235-0532	6.0901	$-2.6 \pm 0.6$	Subaru/HSC $z$ and $y$ bands	11.46	$< 162$ (7)	$< 11.45$	H20
J0217-0208	6.2037	$-0.1 \pm 0.5$	Subaru/HSC $z$ and $y$ bands	11.63	$310 \pm 42$ (7)	$11.65 \pm 0.06$	H20
VR7	6.534	$-1.4 \pm 0.3$	F110W, F160W	$11.22 \pm 0.02$	$< 31.8$ (6)	$< 11.07$	M17, M19
MASOSA	6.543	$-1.1 \pm 0.7$	F110W, F160W	$10.72 \pm 0.06$	$< 27.6$ (6)	$< 11.01$	S15, M15, M17, M19
UVISTA-279127	6.58	$-2.25 \pm 0.38$	UVISTA $Y$ , $J$ , and $H$ bands	$11.37 \pm 0.06$	$< 138$ (6)	$< 11.70$	B18
Himiko	6.595	$-2.0 \pm 0.4$	F125W, F160W	11.07	$< 27$ (6)	$< 10.99$	O13, C18
CR7	6.604	$-2.3 \pm 0.08$	UVISTA $Y$ , $J$ , $K_s$ -band	$11.15 \pm 0.04$	$< 21$ (6)	$< 10.88$	S15, M15, M17

<sup>1</sup> For the non-detections, we show the upper  $3\sigma$  confidence limits.

<sup>2</sup> Bracketed numbers in this column (6 and 7) indicate the specific ALMA band at which the dust continuum was measured by the observations.

<sup>3</sup>  $L_{IR}$  is converted from  $S$  using a MBB function (assuming  $\beta_{IR} = 2.0$ ) with the ‘dust temperature’ that follows Eq. 26 (assuming  $\delta_{dtr} = 0.4$ ).

<sup>4</sup> References: C15: (Capak et al. 2015); B17: Barisic et al. (2017); R11: Richard et al. (2011); K16: Knudsen et al. (2016); H20: Harikane et al. (2020); M17, Matthee et al. (2017); M19: Matthee et al. (2019); S15: Sobral et al. (2015); M15: Matthee et al. (2015); B18, Bowler et al. (2018); O13: Ouchi et al. (2013); I16: Inoue et al. (2016); C18: Carniani et al. (2018b).

to the increase of dust optical depth and the decrease of stellar age) while during quiescent periods, galaxies move downwards and rightwards (due to the decrease of optical depth and the increase of stellar age) (Section 4.4).

- The attenuation curve of galaxies varies with viewing direction, appearing to be shallower (or ‘grayer’) in the direction of higher  $\tilde{\tau}_{0.16}$ , regardless of the morphology of galaxy. For disc galaxies, the edge-on (face-on) direction shows the highest (lowest)  $\tilde{\tau}_{0.16}$  and the shallowest attenuation curve (Section 4.5.2). This is consistent with the recent observational finding reported by Wang et al. (2018) (see also Kriek & Conroy 2013).
- Uncertainties in viewing direction, dust-to-metal mass ratio, stellar population model (single vs. binary star evolution) and conditions of the star-forming birth-clouds are secondary contributors to the scatter in the IRX- $\beta_{UV}$  relation of the MASSIVE-FIRE sample (Section 4.5.2-4.5.4). For a given dust model, the scatter can largely be accounted for by the variations in the intrinsic UV spectral slope of galaxies (Section 4.4). The off-

set of  $\beta_{UV}$  resulting from the variation in the steepness of the extinction curve scales linearly with  $\tilde{\tau}_{0.16}$  (Section 4.5.1).

Estimating observationally the relatively contributions of the various sources to the scatter in the IRX- $\beta_{UV}$  relation is challenging. Most of the current observational constraints in the intermediate redshift range ( $2 \lesssim z \lesssim 4$ ) are derived based on a stacking method, which does not capture the variations of individual sources (Section 3.2). A few studies using DSFGs have complete detections. These samples are biased to the IR-luminous objects, and show a clear ‘secondary dependence’ of the relation on  $L_{IR}$  (Section 3.1). The overall dispersion of this relation at high- $z$  among a general, unbiased galaxy sample is still uncertain.

Measurements of  $\beta_{UV}$  and  $L_{IR}$  carry additional uncertainties mainly because of the common dearth of photometric data points in the SEDs at high- $z$ .  $\beta_{UV}$  estimates may depend on the photometric sampling at rest-UV and be susceptible to the ‘contamination’ by the 2175 Å ‘bump’ feature in the dust extinction curve (Section 5.1). The ‘contamination’ can be more severe in the systems of high  $\tilde{\tau}_{0.16}$  (or IRX), which is indicated by the analytic solution

of the dust slab model (Eq. 25). Additionally,  $L_{\text{IR}}$  estimates may also be uncertain due to the variations in the dust SED shape in the wavelength range (*i.e.* the Wien side of the dust SED) that is not well covered by ALMA bands (Section 5.2).

We have also assessed the IRX- $\beta_{\text{UV}}$  relation of a LBG sample at  $z \approx 5 - 6.5$  that had previously been reported to show significant IRX deficit (*e.g.*, Capak et al. 2015). Using the recently updated  $\beta_{\text{UV}}$  measurements (*e.g.*, Barisic et al. 2017) and the IRXs derived using our best-fit formula for the ‘equivalent dust temperature’ ( $T_{\text{eqv}}$ ) based on MASSIVEFIRE (Eq. 26, and see Liang et al. 2019), the location of these objects in the IRX- $\beta_{\text{UV}}$  plane shows no clear tension with the locally derived dust attenuation laws (MW and SMC). The objects in the sample that show redder  $\beta_{\text{UV}}$  compared to the M99 relation can be accounted for by SMC dust together with a relatively evolved stellar population. We also note that the  $L_{\text{IR}}$  estimates of these galaxies based on ALMA fluxes will typically not be better than  $\pm 0.22$  dex due to a ‘secondary dependences’ of  $T_{\text{eqv}}$ . The next-generation space IR telescope SPICA (Spinoglio et al. 2017; Egami et al. 2018), which covers the spectral range of 12 – 230  $\mu\text{m}$  with much improved sensitivity compared to the *Spitzer* and *Herschel* telescopes, may improve our constraints on the dust SED shape and thus the  $L_{\text{IR}}$  estimates of the high- $z$  galaxies.

## ACKNOWLEDGEMENTS

This manuscript has benefited from discussions with Pascal Oesch (Geneva), Nick Z. Scoville (Caltech), Xuejian (Jacob) Shen (Caltech), Marcel Neeleman (MPIA), Laura Sommovigo (Scuola Normale Superiore) and Andrea Ferrara (Scuola Normale Superiore). We thank Caitlin Casey for providing us with the data that are not publicly available for producing Fig. 4. LL would like to thank the hospitality of the Department of Astronomy of the University of Florida (UF), where part of this manuscript was improved. His research stay at UF was supported by the GRC Grant awarded by the University of Zurich. RF acknowledges financial support from the Swiss National Science Foundation (grant no. 157591). Simulations were run with resources provided by the NASA High-End Computing (HEC) Programme. Additional computing support was provided by HEC allocations SMD-14-5189, SMD-15-5950, SMD-16-7561, SMD-17-1204, by NSF XSEDE allocations AST120025, AST140023, AST150045, by allocations s697, s698 at the Swiss National Supercomputing center (CSCS), and by S3IT resources at the University of Zurich. DN was supported by NSF grants AST-1715206, AST-1908137 and AST-1909153, as well as HST-AR-15043.001. DK acknowledges support from the NSF grant AST-1715101 and the Cottrell Scholar Award from the Research Corporation for Science Advancement. CAFG was supported by NSF through grants AST-1517491, AST-1715216, and CAREER award AST-1652522; by NASA through grant 17-ATP17-0067; by STScI through grant HST-AR-14562.001; and by a Cottrell Scholar Award from the Research Corporation for Science Advancement. PFH was supported by an Alfred P. Sloan Research Fellowship, NASA ATP Grant NNX14AH35G, and NSF Collaborative Research Grant #1411920 and CAREER grant #1455342. This research was supported by the Munich Institute for Astro- and Particle Physics (MIAPP) of the Deutsche Forschungsgemeinschaft (DFG) cluster of excellence ‘‘Origin and Structure of the Universe’’. The Flatiron Institute is supported by the Simons Foundation.

## REFERENCES

- Adelberger K. L., Steidel C. C., 2000, *ApJ*, 544, 218  
 Álvarez-Márquez J., et al., 2016, *A&A*, 587, A122  
 Álvarez-Márquez J., Burgarella D., Buat V., Ilbert O., Pérez-González P. G., 2019, *A&A*, 630, A153  
 Anglés-Alcázar D., Faucher-Giguère C.-A., Kereš D., Hopkins P. F., Quataert E., Murray N., 2017, *MNRAS*, 470, 4698  
 Baes M., Camps P., 2015, *A&C*, 12, 33  
 Baes M., Verstappen J., De Looze I., Fritz J., Saftly W., Vidal Pérez E., Stalevski M., Valcke S., 2011, *ApJS*, 196, 22  
 Bakx T. J. L. C., et al., 2020, *MNRAS*, 493, 4294  
 Bañados E., et al., 2019, *ApJ*, 881, L23  
 Barisic I., et al., 2017, *ApJ*, 845, 41  
 Behrens C., Pallottini A., Ferrara A., Gallerani S., Vallini L., 2018, *MNRAS*, 477, 552  
 Bell E. F., 2002, *ApJ*, 577, 150  
 Bell E. F., 2003, *ApJ*, 586, 794  
 Berta S., et al., 2011, *A&A*, 532, A49  
 Béthermin M., et al., 2015, *A&A*, 573, A113  
 Boquien M., et al., 2012, *A&A*, 539, A145  
 Bourne N., et al., 2017, *MNRAS*, p. stx031  
 Bouwens R. J., et al., 2009, *ApJ*, 705, 936  
 Bouwens R. J., et al., 2014, *ApJ*, 795, 126  
 Bouwens R., et al., 2016, *ApJ*, 833, 72  
 Bouwens R., et al., 2020, arXiv e-prints, 2009.10727  
 Bowler R. A. A., Bourne N., Dunlop J. S., McLure R. J., McLeod D. J., 2018, *MNRAS*, 481, 1631  
 Buat V., Boselli A., Gavazzi G., Bonfanti C., 2002, *A&A*, 383, 801  
 Buat V., et al., 2005, *ApJ*, 619, L51  
 Buat V., Marcillac D., Burgarella D., Le Floc’h E., Takeuchi T. T., Iglesias-Parámo J., Xu C. K., 2007, *A&A*, 469, 19  
 Buat V., Takeuchi T. T., Burgarella D., Giovannoli E., Murata K. L., 2009, *A&A*, 507, 693  
 Burgarella D., et al., 2013, *A&A*, 554, A70  
 Calzetti D., 1997, *ApJ*, 113, 162  
 Calzetti D., Kinney A. L., Storchi-Bergmann T., 1994, *ApJ*, 429, 582  
 Calzetti D., Armus L., Bohlin R. C., Kinney A. L., Koornneef J., Storchi-Bergmann T., 2000, *ApJ*, 533, 682  
 Camps P., Baes M., 2015, *A&C*, 9, 20  
 Camps P., et al., 2015, *A&A*, 580, A87  
 Camps P., Trayford J. W., Baes M., Theuns T., Schaller M., Schaye J., 2016, *MNRAS*, 462, 1057  
 Camps P., et al., 2018, *ApJS*, 234, 20  
 Capak P., et al., 2004, *ApJ*, 127, 180  
 Capak P., et al., 2007, *ApJS*, 172, 99  
 Capak P. L., et al., 2015, *Nature*, 522, 455  
 Carniani S., et al., 2018a, *MNRAS*, 478, 1170  
 Carniani S., Maiolino R., Smit R., Amorín R., 2018b, *ApJ*, 854, L7  
 Casey C. M., 2012, *MNRAS*, 425, 3094  
 Casey C. M., Narayanan D., Cooray A., 2014a, *Physics Reports*, 541, 45  
 Casey C. M., et al., 2014b, *ApJ*, 796, 95  
 Casey C. M., et al., 2018a, *ApJ*, 862, 77  
 Casey C. M., Hodge J., Zavala J. A., Spilker J., da Cunha E., Staguhn J., Finkelstein S. L., Drew P., 2018b, *ApJ*, 862, 78  
 Chabrier G., 2003, *PASP*, 115, 763  
 Charlot S., Fall S. M., 2000, *ApJ*, 539, 718  
 Chary R., Elbaz D., 2001, *ApJ*, 556, 562  
 Cochrane R. K., et al., 2019, *MNRAS*, 488, 1779  
 Conroy C., 2013, *ARA&A*, 51, 393  
 Dale D. A., Helou G., 2002, *ApJ*, 576, 159  
 Dale D. A., Helou G., Magdis G. E., Armus L., Díaz-Santos T., Shi Y., 2014, *ApJ*, 784, 83  
 De Cia A., Ledoux C., Savaglio S., Schady P., Vreeswijk P. M., 2013, *A&A*, 560, A88  
 De Cia A., Ledoux C., Mattsson L., Petitjean P., Srianand R., Gavignaud I., Jenkins E. B., 2016, *A&A*, 596, A97  
 De Looze I., et al., 2014, *A&A*, 571, A69

- De Vis P., et al., 2019, *A&A*, 623, A5
- Dey A., et al., 2008, *ApJ*, 677, 943
- Dole H., et al., 2004, *ApJS*, 154, 93
- Draine B. T., et al., 2007, *ApJ*, 663, 866
- Duchêne G., Kraus A., 2013, *ARA&A*, 51, 269
- Dunlop J. S., et al., 2017, *MNRAS*, 466, 861
- Dwek E., 1998, *ApJ*, 501, 643
- Egami E., et al., 2018, *PASA*, 35
- El-Badry K., Rix H.-W., 2018, *MNRAS: Letters*
- Elbaz D., et al., 2011, *A&A*, 533, A119
- Eldridge J. J., Stanway E. R., 2012, *MNRAS*, 419, 479
- Eldridge J. J., Stanway E. R., Xiao L., McClelland L. A. S., Taylor G., Ng M., Greis S. M. L., Bray J. C., 2017, *PASP*, 34
- Ellis R. S., et al., 2013, *ApJ*, 763, L7
- Faisst A. L., et al., 2017, *ApJ*, 847, 21
- Faisst A. L., Fudamoto Y., Oesch P. A., Scoville N., Riechers D. A., Pavesi R., Capak P., 2020, arXiv e-prints, 2005.07716
- Faucher-Giguère C.-A., 2017, *MNRAS*, 473, 3717
- Faucher-Giguère C.-A., Lidz A., Zaldarriaga M., Hernquist L., 2009, *ApJ*, 703, 1416
- Feldmann R., 2017, *MNRAS: Letters*, 470, L59
- Feldmann R., Hopkins P. F., Quataert E., Faucher-Giguère C.-A., Kereš D., 2016, *MNRAS: Letters*, 458, L14
- Feldmann R., Quataert E., Hopkins P. F., Faucher-Giguère C.-A., Kereš D., 2017, *MNRAS*, 470, 1050
- Ferrara A., Hirashita H., Ouchi M., Fujimoto S., 2017, *MNRAS*, 471, 5018
- Fischera J., Dopita M. A., Sutherland R. S., 2003, *ApJ*, 599, L21
- Fitzpatrick E. L., 1999, *PASP*, 111, 63
- Flores Velázquez J. A., et al., 2020, arXiv e-prints, 2008.08582
- Fudamoto Y., et al., 2017, *MNRAS*, 472, 483
- Fudamoto Y., et al., 2020, *MNRAS*, 491, 4724
- Galametz A., et al., 2013, *ApJS*, 206, 10
- Gill S. P. D., Knebe A., Gibson B. K., 2004, *MNRAS*, 351, 399
- Goldader J. D., Meurer G., Heckman T. M., Seibert M., Sanders D. B., Calzetti D., Steidel C. C., 2002, *ApJ*, 568, 651
- Gordon K. D., Calzetti D., Witt A. N., 1997, *ApJ*, 487, 625
- Gordon K. D., Clayton G. C., Misselt K. A., Landolt A. U., Wolff M. J., 2003, *ApJ*, 594, 279
- Granato G. L., Lacey C. G., Silva L., Bressan A., Baugh C. M., Cole S., Frenk C. S., 2000, *ApJ*, 542, 710
- Grasha K., Calzetti D., Andrews J. E., Lee J. C., Dale D. A., 2013, *ApJ*, 773, 174
- Griffin M. J., et al., 2010, *A&A*, 518, L3
- Groves B., Dopita M. A., Sutherland R. S., Kewley L. J., Fischera J., Leitherer C., Brandl B., van Breugel W., 2008, *ApJS*, 176, 438
- Gruppioni C., et al., 2013, *MNRAS*, 432, 23
- Guo Y., et al., 2013, *ApJS*, 207, 24
- Hahn O., Abel T., 2011, *MNRAS*, 415, 2101
- Hao C.-N., Kennicutt R. C., Johnson B. D., Calzetti D., Dale D. A., Moustakas J., 2011, *ApJ*, 741, 124
- Harikane Y., et al., 2020, *ApJ*, 896, 93
- Harvey P. M., et al., 2013, *ApJ*, 764, 133
- Hayward C. C., Smith D. J. B., 2015, *MNRAS*, 446, 1512
- Hayward C. C., Kereš D., Jonsson P., Narayanan D., Cox T. J., Hernquist L., 2011, *ApJ*, 743, 159
- Hayward C. C., Jonsson P., Kereš D., Magnelli B., Hernquist L., Cox T. J., 2012, *MNRAS*, 424, 951
- Heinis S., et al., 2013, *MNRAS*, 429, 1113
- Hildebrand R. H., 1983, *QJRAS*, 24, 267
- Hinshaw G., et al., 2013, *ApJS*, 208, 19
- Hirashita H., Nozawa T., Villaume A., Srinivasan S., 2015, *MNRAS*, 454, 1620
- Hopkins P. F., 2013, *MNRAS*, 428, 2840
- Hopkins P. F., 2015, *MNRAS*, 450, 53
- Hopkins P. F., Kereš D., Oñorbe J., Faucher-Giguère C.-A., Quataert E., Murray N., Bullock J. S., 2014, *MNRAS*, 445, 581
- Howell J. H., et al., 2010, *ApJ*, 715, 572
- Ilbert O., et al., 2009, *ApJ*, 690, 1236
- Imara N., Loeb A., Johnson B. D., Conroy C., Behroozi P., 2018, *ApJ*, 854, 36
- Inoue A. K., et al., 2016, *Science*, 352, 1559
- Jin S., et al., 2019, *ApJ*, 887, 144
- Jonsson P., Cox T. J., Primack J. R., Somerville R. S., 2006, *ApJ*, 637, 255
- Jonsson P., Groves B. A., Cox T. J., 2010, *MNRAS*, 403, 17
- Kennicutt R. C., 1998, *ARA&A*, 36, 189
- Kennicutt R. C., Evans N. J., 2012, *ARA&A*, 50, 531
- Kinney A. L., Bohlin R. C., Calzetti D., Panagia N., Wyse R. F. G., 1993, *ApJS*, 86, 5
- Knollmann S. R., Knebe A., 2009, *ApJS*, 182, 608
- Knudsen K. K., Richard J., Kneib J.-P., Jauzac M., Clément B., Drouart G., Egami E., Lindroos L., 2016, *MNRAS: Letters*, 462, L6
- Kong X., Charlot S., Brinchmann J., Fall S. M., 2004, *MNRAS*, 349, 769
- Koprowski M. P., et al., 2018, *MNRAS*, 479, 4355
- Kriek M., Conroy C., 2013, *ApJ*, 775, L16
- Krumholz M. R., Gnedin N. Y., 2011, *ApJ*, 729, 36
- Laigle C., et al., 2016, *ApJS*, 224, 24
- Laporte N., et al., 2016, *ApJ*, 820, 98
- Laporte N., et al., 2017, *ApJ*, 837, L21
- Larson R. B., 1981, *MNRAS*, 194, 809
- Leitherer C., Heckman T. M., 1995, *ApJS*, 96, 9
- Leitherer C., et al., 1999, *ApJS*, 123, 3
- Li Q., Narayanan D., Davé R., 2019, *MNRAS*, 490, 1425
- Liang L., Feldmann R., Faucher-Giguère C.-A., Kereš D., Hopkins P. F., Hayward C. C., Quataert E., Scoville N. Z., 2018, *MNRAS: Letters*, 478, L83
- Liang L., et al., 2019, *MNRAS*, 489, 1397
- Lombardi M., Bouy H., Alves J., Lada C. J., 2014, *A&A*, 566, A45
- Lutz D., 2014, *ARA&A*, 52, 373
- Ma J., et al., 2015, *MNRAS*, 454, 1751
- Ma X., Hopkins P. F., Faucher-Giguère C.-A., Zolman N., Muratov A. L., Kereš D., Quataert E., 2016a, *MNRAS*, 456, 2140
- Ma X., Hopkins P. F., Kasen D., Quataert E., Faucher-Giguère C.-A., Kereš D., Murray N., Strom A., 2016b, *MNRAS*, 459, 3614
- Ma J., Ge J., Zhao Y., Prochaska J. X., Zhang S., Ji T., Schneider D. P., 2017, *MNRAS*, 472, 2196
- Ma X., et al., 2019, *MNRAS*, 487, 1844
- Madau P., Dickinson M., 2014, *ARA&A*, 52, 415
- Magnelli B., Elbaz D., Chary R. R., Dickinson M., Le Borgne D., Frayer D. T., Willmer C. N. A., 2009, *A&A*, 496, 57
- Magnelli B., Elbaz D., Chary R. R., Dickinson M., Le Borgne D., Frayer D. T., Willmer C. N. A., 2011, *A&A*, 528, A35
- Matthee J., Sobral D., Santos S., Röttgering H., Darvish B., Mobasher B., 2015, *MNRAS*, 451, 400
- Matthee J., et al., 2017, *ApJ*, 851, 145
- Matthee J., et al., 2019, *ApJ*, 881, 124
- McCracken H. J., et al., 2012, *A&A*, 544, A156
- McLeod D. J., McLure R. J., Dunlop J. S., Robertson B. E., Ellis R. S., Targett T. A., 2015, *MNRAS*, 450, 3032
- McLure R. J., et al., 2013, *MNRAS*, 432, 2696
- McLure R. J., et al., 2018, *MNRAS*, 476, 3991
- Meurer G. R., Heckman T. M., Leitherer C., Kinney A., Robert C., Garnett D. R., 1995, *ApJ*, 110, 2665
- Meurer G. R., Heckman T. M., Calzetti D., 1999, *ApJ*, 521, 64
- Morrissey P., et al., 2007, *ApJS*, 173, 682
- Mortlock A., McLure R. J., Bowler R. A. A., McLeod D. J., Marmol-Queraltó E., Parsa S., Dunlop J. S., Bruce V. A., 2017, *MNRAS*, 465, 672
- Muratov A. L., Kereš D., Faucher-Giguère C.-A., Hopkins P. F., Quataert E., Murray N., 2015, *MNRAS*, 454, 2691
- Narayanan D., et al., 2010, *MNRAS*, 407, 1701
- Narayanan D., Davé R., Johnson B. D., Thompson R., Conroy C., Geach J., 2018a, *MNRAS*, 474, 1718
- Narayanan D., Conroy C., Davé R., Johnson B. D., Popping G., 2018b, *ApJ*, 869, 70
- Narayanan D., et al., 2020, arXiv e-prints, 2006.10757
- Natta A., Panagia N., 1984, *ApJ*, 287, 228

- Neeleman M., Prochaska J. X., Kanekar N., Rafelski M., 2020, *Nature*, 581, 269
- Nguyen H. T., et al., 2010, *A&A*, 518, L5
- Noll S., Burgarella D., Giovannoli E., Buat V., Marcellac D., Muñoz-Mateos J. C., 2009, *A&A*, 507, 1793
- Novak M., et al., 2019, *ApJ*, 881, 63
- Oesch P. A., Bouwens R. J., Illingworth G. D., Franx M., Ammons S. M., Dokkum P. G. v., Trenti M., Labbé I., 2015, *ApJ*, 808, 104
- Oesch P. A., Bouwens R. J., Illingworth G. D., Labbé I., Stefanon M., 2018, *ApJ*, 855, 105
- Oteo I., et al., 2013, *A&A*, 554, L3
- Ouchi M., et al., 2013, *ApJ*, 778, 102
- Overzier R. A., et al., 2011, *ApJ*, 726, L7
- Pei Y. C., 1992, *ApJ*, 395, 130
- Penner K., et al., 2012, *ApJ*, 759, 28
- Poglitsch A., et al., 2010, *A&A*, 518, L2
- Popping G., Puglisi A., Norman C. A., 2017, *MNRAS*, 472, 2315
- Qiu Y., Mutch S. J., da Cunha E., Poole G. B., Wyithe J. S. B., 2019, *MNRAS*, 489, 1357
- Raghavan D., et al., 2010, *ApJS*, 190, 1
- Reddy N. A., Steidel C. C., Fadda D., Yan L., Pettini M., Shapley A. E., Erb D. K., Adelberger K. L., 2006, *ApJ*, 644, 792
- Reddy N. A., Erb D. K., Pettini M., Steidel C. C., Shapley A. E., 2010, *ApJ*, 712, 1070
- Reddy N. A., et al., 2018, *ApJ*, 853, 56
- Richard J., Kneib J.-P., Ebeling H., Stark D. P., Egami E., Fiedler A. K., 2011, *MNRAS: Letters*, 414, L31
- Rodighiero G., et al., 2011, *ApJ*, 739, L40
- Rosolowsky E., Engargiola G., Plambeck R., Blitz L., 2003, *ApJ*, 599, 258
- Safarzadeh M., Hayward C. C., Ferguson H. C., Somerville R. S., 2017a, *ApJ*, 818, 62
- Safarzadeh M., Hayward C. C., Ferguson H. C., 2017b, *ApJ*, 840, 15
- Salim S., Boquien M., 2019, *ApJ*, 872, 23
- Salim S., Narayanan D., 2020, arXiv e-prints, 2001.03181
- Sana H., et al., 2012, *Science*, 337, 444
- Schady P., et al., 2012, *A&A*, 537, A15
- Schreiber C., Elbaz D., Pannella M., Ciesla L., Wang T., Franco M., 2018, *A&A*, 609, A30
- Schulz S., Popping G., Pillepich A., Nelson D., Vogelsberger M., Marinacci F., Hernquist L., 2020, *MNRAS*
- Scoville N. Z., 2013, in Falcón-Barroso J., Knapen J. H., eds, *Secular Evolution of Galaxies*. Cambridge University Press, Cambridge, UK, p. 491
- Seon K.-I., Draine B. T., 2016, *ApJ*, 833, 201
- Shao L., et al., 2010, *A&A*, 518, L26
- Shen X., et al., 2020, *MNRAS*, 495, 4747
- Skelton R. E., et al., 2014, *ApJS*, 214, 24
- Sklia P., et al., 2014, *A&A*, 561, A149
- Snyder G. F., et al., 2015, *MNRAS*, 454, 1886
- Sobral D., Matthee J., Darvish B., Schaerer D., Mobasher B., Röttgering H. J. A., Santos S., Hemmati S., 2015, *ApJ*, 808, 139
- Solomon P. M., Rivolo A. R., Barrett J., Yahil A., 1987, *ApJ*, 319, 730
- Somerville R. S., Davé R., 2015, *ARA&A*, 53, 51
- Sommovigo L., Ferrara A., Pallottini A., Carniani S., Gallerani S., Decataldo D., 2020, *MNRAS*, 497, 956
- Sparre M., Hayward C. C., Feldmann R., Faucher-Giguère C.-A., Muratov A. L., Kereš D., Hopkins P. F., 2017, *MNRAS*, 466, 88
- Spinoglio L., et al., 2017, *PASA*, 34
- Stanway E. R., Eldridge J. J., 2018, *MNRAS*, 479, 75
- Stanway E. R., Eldridge J. J., Becker G. D., 2016, *MNRAS*, 456, 485
- Steidel C. C., Giavalisco M., Dickinson M., Adelberger K. L., 1996, *ApJ*, 112, 352
- Stratta G., Maiolino R., Fiore F., D’Elia V., 2007, *ApJ*, 661, L9
- Swinyard B. M., et al., 2010, *A&A*, 518, L4
- Takeuchi T. T., Yuan F.-T., Ikeyama A., Murata K. L., Inoue A. K., 2012, *ApJ*, 755, 144
- Torrey P., et al., 2015, *MNRAS*, 447, 2753
- Trayford J. W., et al., 2017, *MNRAS*, 470, 771
- Trayford J. W., Lagos C. d. P., Robotham A. S. G., Obreschkow D., 2019, *MNRAS*
- Tremonti C. A., et al., 2004, *ApJ*, 613, 898
- Venemans B. P., et al., 2017, *ApJ*, 851, L8
- Vogelsberger M., Marinacci F., Torrey P., Puchwein E., 2020, *Nature Reviews Physics*, 2, 42
- Walter F., et al., 2016, *ApJ*, 833, 67
- Wang B., Heckman T. M., 1996, *ApJ*, 457, 645
- Wang W., et al., 2018, *ApJ*, 869, 161
- Watson D., Christensen L., Knudsen K. K., Richard J., Gallazzi A., Michałowski M. J., 2015, *Nature*, 519, 327
- Weingartner J. C., Draine B. T., 2001, *ApJ*, 548, 296
- Whitaker K. E., Pope A., Cybulski R., Casey C. M., Popping G., Yun M. S., 2017, *ApJ*, 850, 208
- Williams R. J., Quadri R. F., Franx M., van Dokkum P., Labbé I., 2009, *ApJ*, 691, 1879
- Wiseman P., Schady P., Bolmer J., Krühler T., Yates R. M., Greiner J., Fynbo J. P. U., 2017, *A&A*, 599, A24
- Witt A. N., Gordon K. D., 1996, *ApJ*, 463, 681
- Witt A. N., Gordon K. D., 2000, *ApJ*, 528, 799
- Xue Y. Q., et al., 2011, *ApJS*, 195, 10
- Zafar T., Watson D., Fynbo J. P. U., Malesani D., Jakobsson P., de Ugarte Postigo A., 2011, *A&A*, 532, A143
- Zafar T., et al., 2018, *MNRAS*, 479, 1542
- da Cunha E., et al., 2013, *ApJ*, 766, 13

This paper has been typeset from a  $\text{\TeX}/\text{\LaTeX}$  file prepared by the author.